Data Assimilation in a Regional Finite Element Sea-Ice Model for the Arctic - Application of the Singular Evolutive Interpolated Kalman Filter

Katja Rollenhagen

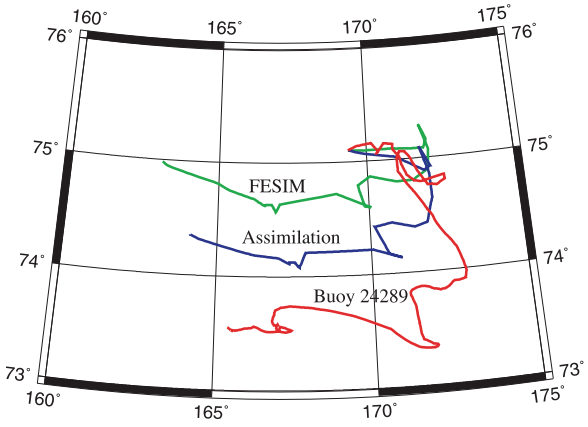

Universität Bremen 2008

Data Assimilation in a Regional Finite Element Sea-Ice Model for the Arctic - Application of the Singular Evolutive Interpolated Kalman Filter

von Katja Rollenhagen

Dissertation

zur Erlangung des Grades eines Doktors der Naturwissenschaften
– Dr. rer. nat. –

Vorgelegt im Fachbereich I (Physik/Elektrotechnik) der

Mai 2008

Diese Arbeit wurde durchgeführt am
ALFRED-WEGENER INSTITUT FÜR POLAR- UND MEERESFORSCHUNG
Bremerhaven

1. Gutachter: Prof. Dr. rer. nat. Peter Lemke
2. Gutachter: Prof. Dr. rer. nat Rüdiger Gerdes

Eingereicht am: 25. März 2008
Promotionskolloquium am: 29. Mai 2008

Abstract

The Arctic region is sensitive to climate change. Since the Arctic sea-ice cover influences the surface heat budget of the Earth the observed sea-ice decline is seen as an indication of global warming. Furthermore, the dynamics of sea ice plays an important role for the sea-ice mass distribution in the Arctic, for the production of dense, cold, and salty water in the Arctic Ocean, which contributes to the thermohaline circulation, and also for the freshwater budget of the Nordic Seas. Thus, a realistic description of sea-ice motion is important to draw conclusions for the mass transport and sea-ice mass distribution.

The Finite-Element Sea-Ice Model simulates the large-scale physical sea-ice processes like the sea-ice growth and circulation realistically. The model domain covers the entire Arctic Ocean and its marginal seas. Together with the Singular Evolutive Interpolated Kalman (SEIK) Filter and remotely sensed sea-ice drift observations this sea-ice model is applied for data assimilation to investigate details of the sea-ice dynamics.

So far, drift assimilation has been carried out to analyze and modify only the drift field with subsequent computation of the advection or redistribution of ice mass which corresponds more to the physical model behavior than a statistical analysis that the SEIK Filter provides. The sea-ice drift data assimilation with the SEIK Filter achieves drift modification and furthermore changes in the two other sea-ice variables concentration and thickness. The modifications of these "unobserved variables" (within the meaning of data assimilation) are validated and it is found that they are in good agreement for at least 2 months for the sea-ice thickness and even 4 months for the sea-ice concentration which is the longest period examined. The drift improvement is achieved due to the sea-ice concentration and thickness changes which leads to a sustainable effect for further sea-ice drift simulation. Furthermore, the assimilation results suggest a higher thickness variability that the model alone is not able to produce. A localized version of the SEIK Filter leads to a more pronounced drift correction which is not sustainable in course of further model integration because in this case the sea-ice concentration and thickness are not much affected by the assimilation method.

This thesis describes the initial work of the sea ice drift assimilation with the SEIK Filter and further examines the ability of the SEIK Filter to modify the model state using the observation data. The applicability, capability, limitation of the assimilation method and suggestions are discussed.

Zusammenfassung

Die Arktis ist eine Region, die sensibel auf klimatische Änderungen reagiert. Da die Meereisbedeckung auf die Wärmebilanz der Erde Einfluss nimmt, wird der beobachtete Eisrückgang als Indikator für die Klimaerwärmung angesehen. Dabei spielt die Dynamik des Meereises ebenso eine wichtige Rolle. Sie beeinflusst die Eismassenverteilung, die Bildung von dichtem, kalten und salzigen Wasser, das in den Ozean absinkt und zur Thermohalinen Zirkulation beiträgt, und auch die Nordmeere und deren Süßwasserhaushalt. Eine realistische Beschreibung der Meereisbewegung ist daher wichtig um z.B. Rückschlüsse auf die Massentransporte oder auch die Meereisverteilung ziehen zu können.

Das Finite Elemente Meereis Modell kann die großskaligen physikalischen Prozesse des Meereises, wie das Eiswachstum und Schmelzen und die Meereiszirkulation, realistisch simulieren. Das Modellgebiet umfasst den gesamten Arktischen Ozean sowie dessen Randmeere. Zusammen mit einem Singular Evolutive Interpolated Kalman (SEIK) Filter und Meereisdrift aus Fernerkundungsdaten wird dieses Meereismodell zur Datenassimilation verwendet, um die Meereisdynamik zu untersuchen.

Bisher wurde bei der Driftassimilationen nur das Driftfeld analysiert und modifiziert, um dann die Umverteilung der Eismasse zu berechnen, was eher dem physikalischen Verhalten entgegenkommt als einer statistische Analyse wie mit dem SEIK Filter. Die Datenassimilation von Meereisdrift mit dem SEIK Filter verändert jedoch nicht nur die Drift sondern modifiziert auch die anderen Größen Eiskonzentration und -dicke. Die Veränderungen der "nicht beobachteten" Größen (im Sinne der Datenassimilation) sind validiert und zeigen eine gute Übereinstimmung mit Beobachtungsdaten für mindestens zwei Monate für die Eisdicke und für vier Monate für die Eiskonzentration. Der Zeitraum von vier Monaten ist zugleich der längste untersuchte Zeitraum für die durchgeführte Datenassimilation. Die Driftverbesserung ist durch Veränderungen der Eiskonzentration und Dicke hervorgerufen was zugleich zu einen langanhaltenden Effekt für die weitere Meereisdriftsimulation führt. Desweiteren lassen die Ergebnisse der Datenassimilation auf eine höhere Eisdickenvariabilität schließen, welche das Model alleine nicht in der Lage ist zu erzeugen. Eine lokalisierte Version des SEIK Filters erziehlt eine ausgeprägtere Driftkorrektur. Diese ist nicht langanhaltend und wird im Verlauf folgender Modelintegrationen "vergessen", da die Eiskonzentration und -dicke kaum Veränderungen durch diese Assimilationsmethode erfahren.

Diese Arbeit stellt die ersten Schritte dar, Meereisdrift mit dem SEIK Filter zu assimilieren und untersucht vorrangig die Fähigkeiten des Filters den Modellzustand mit Hilfe der Beobachtungen zu modifizieren. Die Anwendbarkeit, Fähigkeit und Einschränkungen der Assimilationsmethode sowie weitere Vorschläge werden diskutiert.

Contents

1 Sea Ice in the Arctic Climate System

The Arctic polar region comprises the northernmost part of America, Europe and Asia, and the Arctic ocean and its marginal seas: Baffin Bay, Greenland Sea, Norwegian Sea, Barents Sea, Kara Sea, Laptev Sea, Chukchi Sea, Bering Sea (south of Bering Strait), and Beaufort Sea (Figure 1.1). The Arctic ocean covers an area of 9.5×10^6 km^2. Approximately one third of this area is part of shallow shelf seas: The Chukchi, East Siberian, Laptev, Kara and Barents Seas are all less than 200 m deep; the deep basins are the Canada Basin and the Eurasian Basin with a depth of more than 4000 m. One of the connections with the Atlantic Ocean is the Fram Strait between Greenland and Svalbard. The most notable feature of the Arctic ocean is the sea ice cover which varies seasonally and influences the Arctic and the world climate by making the surface heat balance in this region even more negative.

The region can be defined e.g. by geographical, climatic or marine characteristics: The Arctic Circle defines the boundary of the midnight sun and is located at 66.56° N. Due to the declination of the Earth's rotation axis of 23.44° the sun does not set in summer and does not rise in winter north of the Arctic Circle. This period varies from a single day (at the polar circle) up to 6 months (at the pole).

The climatic Arctic boundary is defined by the area where the mean July temperature is below the 10° C isotherm. This isotherm encloses the Arctic Ocean with its marginal seas, Greenland, Svalbard, most of Iceland and the northern coasts and islands of Russia, Canada and Alaska. The heat transport of the north Atlantic current (the extension of the Gulf Stream) deflects the isotherm northward in such a way that only the northernmost areas of Scandinavia are included. Cold Arctic water and air push the 10° C isotherm southward in the regions of North America and Northeast Asia.

The marine boundary of the Arctic is located along the convergence of cool less saline surface waters from the Arctic Ocean and warmer saltier waters from the oceans to the south. In the eastern Canadian Archipelago this zone stretches along 63° N. Off the east coast of Greenland the marine boundary lies at approximately 65° N where the warming effect of the North Atlantic Current deflects this boundary north of 80° N west of Svalbard while it moves southward in the Barents Sea to 76° N. In contrast, it is difficult to assign a distinct boundary separating Pacific water from Arctic water. There, the boundary is arbitrarily drawn across Bering Strait (*AMAP*, 1998).

This section gives an overview of the general Arctic climate and its sensitivity to global climate change, introduces the general properties of sea ice, gives a brief overview of sea-ice modeling development as well as a review of and the motivation to sea ice data assimilation which is the intention of this work.

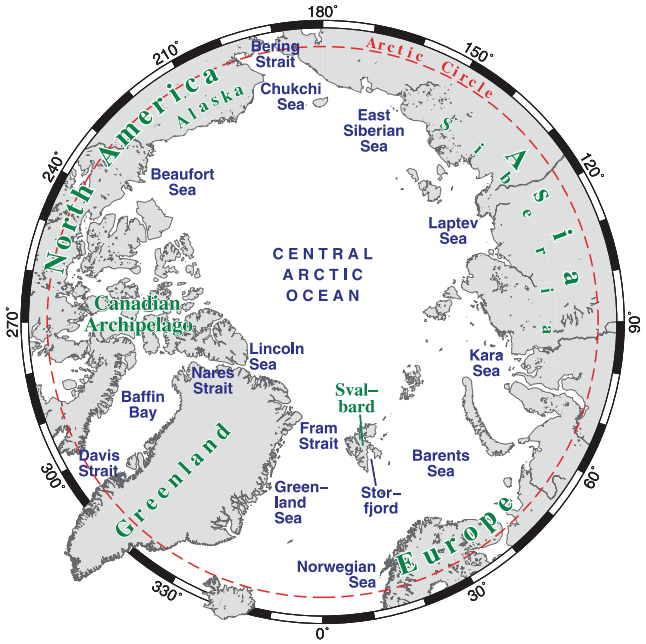

Figure 1.1: Map of the Arctic Ocean: in green are named the coastal Arctic areas in blue the Arctic seas; by courtesy of Torge Martin

1.1 The Arctic Climate

The Arctic is dominated by low temperatures and plays an important role in the world climate system. The cooling in the polar regions leads to an intensified meridional temperature gradient which influences the climate in the lower latitudes. The solar irradiation is reflected by cloud, snow and ice cover which supports the cooling. The annual amount of solar irradiation the Earth receives is less than the infrared radiation that is lost to space because a large part of the radiation is reflected by extensive cloud, snow and ice cover. This results in a negative radiation balance.

The snow covered sea ice has the highest albedo (Table 2.1) and the incoming radiation is reflected such that the radiation energy supply to the Earth system is strongly reduced. The open ocean has a significantly smaller albedo due to the darker surface and the solar radiation can be absorbed by the ocean surface and warms the system. If more area is covered with ice and snow, less energy is supplied, the region becomes colder and more sea ice can form. That positive feedback for cooling the region is called the ice albedo feedback. This feedback works also in the other direction: the more open water is present the more solar energy is absorbed, which leads to warming and further melting and more open water areas. Thus, the Arctic is a very sensitive system to climate warming. Recent observations support the warming, e.g. the sea ice decline (*National Snow and Ice Data Center*, 2005) and a lengthened melting period in the Arctic (*Belchansky et al.*, 2004). It has already been suggested that the tipping point of the system has been reached

(*Lindsay and Zhang*, 2005) and the albedo feedback accelerates a warming in the Arctic and the sea ice decline.

During winter the cooling over the Arctic is supported by a characteristic sea level pressure (SLP) pattern: The Siberian High, a high pressure system over the northern Asian continent which can form a high pressure ridge towards the American continent. Its stability is due to the large land mass and the cold continental climate in winter. It is associated with cold air flowing in winter from the high-pressure area over northern Siberia to the Pacific and cold air flowing northwest from the high-pressure area over the Canadian Arctic towards the low-pressure over the Atlantic. These winds result in very severe climatic conditions in the Arctic. However, the link to the world climate system is related to the preferred tracks of persistent Pacific and Atlantic low pressure systems, the Aleutian Low and the Iceland Low. The latter enters the Arctic mainly from the North Atlantic via the Greenland, Norwegian or Barents Seas. Fewer cyclones enter from the Pacific Ocean. In general, the cyclones transport warm air into the cold region and might cause melting even in winter. During the second half of the twentieth century an increase in the number and intensity of cyclones, which enter the Arctic, has been observed and is related to climate warming (*McCabe et al.*, 2001; *Zhang et al.*, 2004).

The formation and presence of sea ice has important effects on the Arctic climate. The sea-ice cover insulates the relatively warm ocean from the cold atmosphere and has a regulating effect on the temperature. Generally in the central Arctic the average temperature is between -30 and -35° C in winter and between 0 and 2° C in summer (*AMAP*, 1998). In contrast, there are only small variations in ocean temperature between summer and winter due to sea ice on top of the ocean surface layer which is at the freezing point even in summer. The sea-ice formation produces dense, cold, and salty water sinking into the deep ocean (deep water formation) which contributes to the thermohaline circulation. Thus, the sea-ice cover influences indirectly the structure of the ocean water mass. Besides the moving short-lived depressions, which have a warming effect on the Arctic, ocean currents enter the Arctic Ocean and are assumed to influence the Arctic ice cover and might have potential impacts on processes occurring at lower latitudes (*Polyakov et al.*, 2005).

1.2 The Arctic Ocean Sea-Ice Cover

The existence of the Arctic sea-ice cover is the response to the low temperatures and the small solar flux, including the absence of solar radiation during the polar night which supports sea ice growth. Low temperatures in summer are caused by the low altitude of the sun and the high reflectance (albedo) of the snow and sea ice cover which delays spring melt and limits the summer decay. Due to the salinity of the Arctic Ocean the water density anomaly is bypassed and the salty water has its maximum density at the freezing point, approximately -1.8° C for a salinity of 35 parts per thousand (ppt), such if the ocean surface layer is cooled down to the freezing point temperature the sea ice can grow. New ice forms by phase transition of ocean water to sea ice in autumn and winter,

the brine is mostly rejected which leads to an increasing density of the surface ocean layer and enhances the depth of the vertical mixing. The salinity of sea ice decreases with time and multi-year sea ice can have a salinity of 0 - 4 ppt (*Weeks*, 1998) and can be regarded as frozen freshwater. The sea-ice melt starts in spring and the freshwater is released into the surface ocean layer which decreases vertical mixing and stabilizes the ocean stratification.

1.2.1 Sea-Ice Coverage

The sea-ice cover can be characterized by the sea-ice concentration which is 100 % if the regarded area is totally covered with sea ice and 0 % in case of completely open water. Values between zero and hundred percent give the fraction of ice covered ocean. The interior ice pack has a sea-ice concentration typically exceeding 97 % in winter and decreasing during summer to 85 - 95 % (*Parkinson et al.*, 1987). The total sea-ice covered area varies from $14 \cdot 10^6$ km^2 in winter (March) to $7 \cdot 10^6$ km^2 in summer (September) (*Bjørgo et al.*, 1997; *Johannessen et al.*, 2004)

The existence of open water in the central Arctic is caused mainly by dynamic processes. Wind stresses open and close leads which can form with ranges of 10 to 1000 m. Leads can exceed 10 km in width near the coast creating the coastal polynyas, (*Barry et al.*, 1993). Dynamic processes can also cause ice floes to break into smaller blocks which pile up and result in consumption of ice area. The sea-ice extent varies seasonally but also the minima in summer vary from year to year. The maxima, the winter coverage, seems to be almost stable or shows a slightly decreasing trend (*Walsh and Chapman*, 2001). Contrary, the minima exhibit a significant decreasing trend (*National Snow and Ice Data Center*, 2005; *Walsh and Chapman*, 2001; *IPCC*, 2007) which is interpreted as an evidence for global warming.

The sea-ice coverage is important for the Arctic ocean because the sea-ice cover acts as an insulator hindering exchange of heat, momentum, moisture, gases and aerosols. The heat flux between ocean and atmosphere is decreased by 1 - 2 order of magnitudes in presence of sea ice which depends on the sea-ice thickness. The average Arctic ocean heat flux is 2 - 5 W m^{-2} (*Maykut*, 1986; *Maykut and Phee*, 1995; *Krishfield and Perovich*, 2005). The thicker the ice the less energy is transfered from the ocean to the atmosphere. The heat exchange in areas of open water, e.g. polynyas in winter, can reach up to 450 W m^{-2} (*Andreas and Cash*, 1999).

1.2.2 Sea-Ice Circulation

The sea-ice cover is generally in motion except at coastal regions where sea ice is attached to the shoreline which is called landfast ice. The average sea-ice motion features two typical drift patterns (Figure 1.2): the Beaufort Gyre, which comprises a clockwise (anticyclonic) motion with a center in the Canada Basin, and the Transpolar Drift Stream (TDS), in which the sea ice is advected away from the Siberian coast across the pole and towards the Greenland Sea which is important for sea-ice export through the Fram Strait.

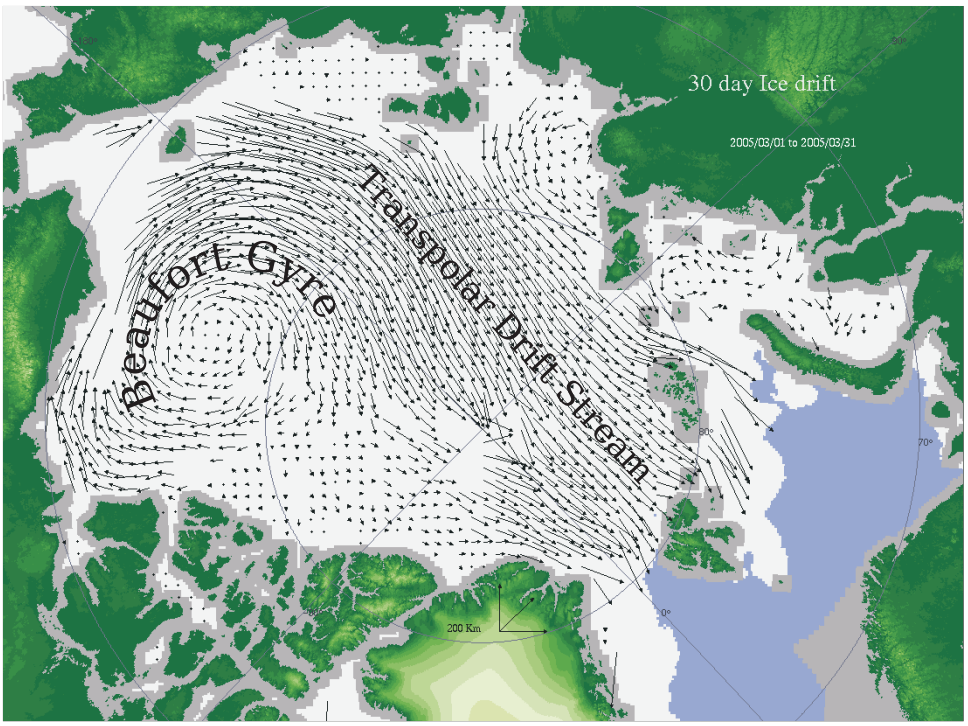

Figure 1.2: Characteristic sea-ice drift in the Arctic: the typical pattern of the Beaufort Gyre and the Transpolar Drift Stream were observed for March 2005; the picture is provided by CERSAT, the drift is derived from Quikscat and SSM/I data.

The sea-ice drift is determined by the forces acting on the sea ice. The atmospheric and oceanic drag and the internal forces of sea ice are the most important components, a smaller contribution results from the Coriolis force and the sea surface tilt. At the ice edge and in areas where the concentration is below 80 %, the drift is dominated by free drift conditions, where the internal interactions are negligible. In winter months the sea-ice drift is almost parallel ($\pm 10°$) to the geostrophic wind[1] and the drift speed is approximately 2 % of the wind speed for free drift conditions and the wind contribution to the ice motion can be decreased to 0 % if the internal forces dominate (*Kimura and Wakatsuchi*, 2000). It is dependent on the spatial thickness distribution because compact and thicker ice conditions lead to increasing sea-ice resistance.

The atmosphere has a high variability and changes very frequently and the sea-ice, which is mainly influenced by the wind, reacts very fast and reflects the atmospheric features like cyclones very well. On a seasonal scale an anticyclonic regime dominates in winter, which supports the Beaufort Gyre, which leads rather to a recirculation of

[1]The geostrophic wind is the wind that results from an exact balance between Coriolis force and the pressure gradient force. It is directed parallel to isobars - lines of constant pressure at a given height. The surface wind almost always differs from the geostrophic wind due to the friction, which becomes larger the smaller the distance to the surface is regarded.

sea ice. A cyclonic regime dominates in summer supporting a TDS and sea ice export through the Fram Strait (*Proshutinsky et al.*, 2002).

The Beaufort Gyre recirculates and accumulates the sea ice such that ice can survive the melt season and multi-year ice is present off the Greenland-Canadian and Alaskan coast. The drift around the Beaufort Gyre takes typically 5 - 10 years (*Thorndike*, 1986) with an average speed of 1 - 3 $\mathrm{cm\,s^{-1}}$. Contrary, sea ice is exported off the Siberian coast such that first-year ice is transported towards the pole and open water can refreeze during the freezing period. The transport across the Arctic with the TDS requires about 3 years (*Thorndike*, 1986) with increasing sea-ice velocities towards the Fram Strait of 5 - 10 $\mathrm{cm\,s^{-1}}$. The marginal Siberian seas are the ice production zones of the Arctic Ocean. First-year ice dominates here because during summer ice retreat in that area is amplified due to the general drift regime and no ice grows during melt season. Open water areas dominate in summer, especially since the summer sea ice decline in recent years (*National Snow and Ice Data Center*, 2005). However, the general circulation pattern resembles the mean atmospheric surface pressure but underlies the high short-term variability of the atmosphere. Therefore on small time scales drift patterns with a counter clockwise Beaufort Gyre can emerge due to atmospheric conditions as well as a drift stream across the central Arctic into the Beaufort Sea. Still, the more steady ocean currents influence the drift on long-term scales as well.

Deformation processes forced by sea ice motion also influence the atmosphere and ocean. Deformation such as ridging influences the roughness of sea ice and the oceanic and atmospheric drag increases. Since the sea ice is transported across the Arctic Ocean and into the North Atlantic most of the exported sea-ice melts in the Greenland and Norwegian Sea. The low density of melted freshwater has a stabilizing effect on the ocean stratification. Thus, the sea ice is a storage of freshwater, and signals can be retained beyond annual cycles. The sea ice transport affects these properties on a large scale because sea ice freezes and melts at different locations.

1.2.3 Sea-Ice Thickness

The sea ice can be divided into different ice types: the level ice, which is undeformed and is thermodynamically grown, and dynamically thickened sea-ice: hummocked ice, pressure ridges with keels that may extend to a depth of 20 m or more with resulting openings where new ice can form during the freezing period.

The sea ice grows thermodynamically when the ocean is at the freezing point and the atmosphere is continuing to cool. In winter the temperature difference between ocean and atmosphere is generally between 20 and 30° C. Due to the insulating effect of the ice cover the thermodynamic ice growth is limited to an upper sea-ice thickness with an equilibrium thickness of 2.5 - 3 m on the Arctic Ocean (*Maykut*, 1986). The limit is defined by the heat flux which is transfered by heat conduction through the ice which is depending on the sea-ice thickness and the temperature difference between atmosphere and ocean. Additionally, it is dependent on the thermal conductivity of sea ice, which is a function of the sea-ice temperature and salinity and is between 1.0 - 2.5 $\mathrm{W\,m^{-1}\,K^{-1}}$ (*Untersteiner*, 1961; *Yen*, 1961; *Maykut*, 1986). It has been found that the equilibrium

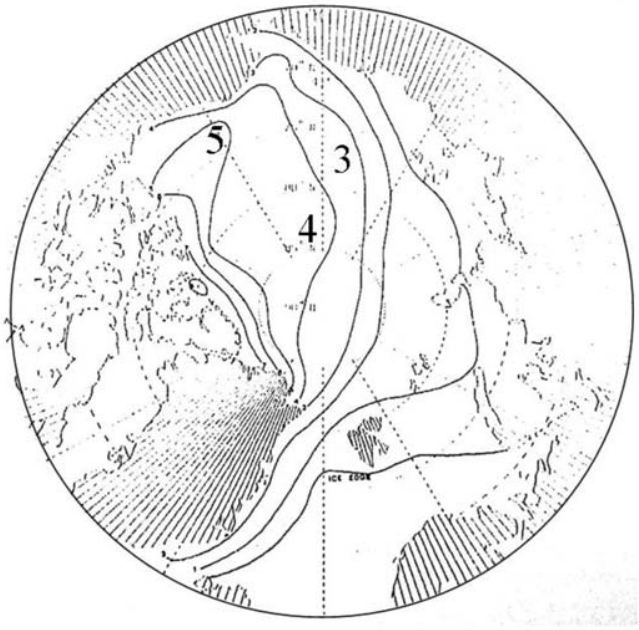

Figure 1.3: Mean Arctic sea ice draft (m) in winter derived from the entire submarine under ice data set by *Bourke and Garrett* (1987)

sea-ice thickness can not be reached thermodynamically in a single winter season (*Eicken*, 2003).

Besides the freezing there are dynamical processes which thicken the sea ice. These processes exceed the thermodynamical equilibrium sea-ice thickness. Ridging piles up ice blocks forming sails and deep keels. Then the conductive heat flux decreases and sea-ice formation is reduced. Even in winter time melting may occur at the deepest point of a keel, in which ice blocks are pushed well below the draft of flat, level ice floes, while the undeformed ice next to the ridge is still growing. This can occur due to different dominating effects which depend on the sea ice thickness: the basal melting occurs when oceanic heat flux dominates and freezing when the conductive heat flux is higher. Therefore the thermodynamics always drives the sea ice towards the equilibrium thickness which is also representative for the average Arctic sea-ice thickness.

However, the sea-ice thickness is one of the less known sea-ice properties because the observation data base is sparse temporally as well as spatially. Mainly submarine sonar sea-ice draft measurements are used to estimate sea-ice thickness and its distribution in the Arctic Ocean, besides sparse data of ice cores, aircraft laser measurements of the freeboard, and electromagnetic ice thickness measurements (*Bourke and Garrett*, 1987; *Haas*, 2004; *Haas et al.*, 2006). The large-scale sea-ice distribution derived from several submarine cruises (*Bourke and Garrett*, 1987) can be explained by dynamical and thermodynamical processes. Evident is the thick sea ice along the north Greenland,

Canadian and Alaskan coasts (Figure 1.3) which is due to the recirculation and transport towards these coasts accumulating and piling up of sea ice. The thinner ice on the Siberian Seas is clearly caused by the TDS transport towards the pole maintaining the thinner mean sea-ice thickness in that region. The seasonal and interannual variability in sea-ice thickness is poorly known as well as the spatial variability. First charts of seasonal variability have been presented by *Bourke and Garrett* (1987) and can be explained by seasonal varying thermodynamical and dynamical processes.

Due to the lack of data coverage and the recently observed massive sea-ice decline the question of sea-ice thickness decline becomes more pressing. Based on submarine ice draft data it has been reported that sea ice has thinned by 40% from the 1960s and 1970s to the 1990s (*Rothrock et al.*, 1999). *Holloway and Sou* (2002) argue that the decrease of observed submarine sea-ice drafts recorded by *Rothrock et al.* (1999) is caused by aliased sampling of spatial and temporal variability of sea-ice thickness. *Rothrock et al.* (2003) report positive agreement in temporal changes of ice thickness between model simulations and the submarine observations and a basinwide thinning of the ice over the period between 1987 and 1997.

Lindsay and Zhang (2005) have examined the thinning Arctic sea ice from 1988-2003 by modeling. They suggest that the Arctic system has passed a tipping point and recent thinning is now dominated by the ice albedo feedback. They also suggest that 1989 represents the tipping point for the Arctic ice-ocean system because by then it reached a state in which triggering events were able to initiate a process of continuous rapid change even though external forcing has changed only little. Their line of argument leads to a decline of Arctic sea-ice extent and thickness which started with an increase in autumn, winter and spring air temperature over the Arctic Ocean, which may reflect the response of the Arctic system to the climate warming signal.

1.3 Modeling the Arctic Sea-Ice Cover

Simulating the large-scale behavior of sea-ice requires descriptions for the sea-ice freezing and melting as well as for the sea-ice motion.

Simple thermodynamic models simulate the sea-ice growth (*Semtner*, 1976; *Thorndike*, 1992) but can not be used to investigate sufficiently climate changes. Although these models are not adequate it has been found that there are two equilibriums: continuous ice pack or a completely ice free ocean.

Since the thermodynamic sea-ice growth is only a part of the true sea-ice state, the important effect of sea-ice motion has to be included into a model to obtain realistic simulations. Simple approaches have been proposed by *Bryan et al.* (1975) and *Manabe et al.* (1979) where the ice is advected with the ocean surface current or a free ice drift is assumed but no internal forces occur. These simplified assumptions are sufficient to study only some of the dynamic processes of the sea-ice cover.

Thus, descriptions of the internal stress as a function of sea-ice deformation rates (rheology) have been developed. With the assumption that the sea ice behaves like a Newtonian fluid (*Campbell*, 1965) the influence of the internal forces onto the sea-ice

motion far away from the coasts has been successfully simulated. In this approach, the influence of convergent and divergent deformation is neglected, which deteriorates the sea-ice motion especially near the coast.

Then, the behavior of the sea ice with the assumption of a linear-viscous fluid has been studied (*Hibler*, 1975; *Rothrock*, 1975; *Hibler and Tucker*, 1979). Here, seasonal and regional variability arise for differently selected bulk and shear viscosities which describe the resistance to convergence and shear. Such a variation of the viscosities suggests a non-linear approach for the description of the internal force. The Arctic Ice Dynamics Joint Experiment (AIDJEX) in the 1970s led to the conclusion that a non-linear approach can explain the occurrence of internal forces without simultaneously emerging deformation; and an elastic-plastic approach has been suggested (*Coon et al.*, 1974).

The approach that sea ice behaves like a plastic material has also been investigated. This describes the phenomena of shear strain in the coastal areas and almost deformation-free drift patterns far away from the coast (*Coon et al.*, 1974; *Pritchard*, 1975; *Rothrock*, 1975; *Hibler*, 1979). Consequently, other non-linear plastic rheologies have been investigated (*Flato and Hibler*, 1992; *Ip et al.*, 1991).

A survey of various rheologies has been carried out with identical model configurations which yields the conclusion that the viscous-plastic rheology (*Hibler*, 1979; *Harder*, 1996; *Zhang and Hibler*, 1997) gives the most realistic performance of the sea-ice simulation (*Harder*, 1997; *Lemke et al.*, 1997; *Kreyscher et al.*, 1997; *Kreyscher*, 1998). Here, the sea ice is described as a plastic medium which reacts with deformation in case of convergence as well as shear. A modification of the viscous-plastic rheology is used in the the elastic-viscous-plastic approach (*Hunke and Dukowicz*, 1997) which is a numerical rather than a physical improvement.

In recent years sea-ice models have been coupled to ocean models to obtain sophisticated simulations of the sea-ice and ocean interaction. Various sea-ice variability studies have been performed e.g. for the sea-ice drift variability in sea-ice ocean models. They reveal that the calculation of the momentum transfer from the atmosphere to the sea ice is critical for the sea-ice drift and the sensitivity to ocean drag and coupling methods are not negligible (*Martin and Gerdes*, 2006). For the variability of Arctic sea-ice volume and sea-ice export has been found that the wind forcing contributes significantly to the decadal variability in the Arctic ice volume and the important role of the meridional exchange of water and air between the Atlantic and the Arctic has been pointed out (*Köberle and Gerdes*, 2003; *Goosse et al.*, 2003). The sea-ice ocean models are also applied to investigate the Arctic warming such as the examination of the recent development of the sea-ice state in which very large extents of summer open water and winter first-year ice are the norm (*Lindsay and Zhang*, 2005). A more recent, numerical approach to model the sea-ice and ocean state is to use finite element methods (e.g. *Danilov and Yakovlev*, 2003; *Danilov et al.*, 2004) which have the advantage of unstructured meshes which allow model grid refinement in regions of scientific interest which can then be studied in more detail.

Uncoupled, stand-alone or simplified sea-ice models are commonly used as toy-models to check or examine new techniques or approaches. For example, the approximations of

local features like sea-ice ridges for a large-scale sea-ice model has been examined with an uncoupled sea-ice model (*Martin*, 2007) or the influence of sea-ice data assimilation to the model behavior has been studied with a simplified sea-ice model (*Dulière and Fichefet*, 2007). In this thesis, the Finite Element Sea-Ice Model (*Danilov and Yakovlev*, 2003) that has been developed at the Alfred Wegener Institute is applied for sea-ice data assimilation, and the assimilated sea-ice state is examined.

1.4 Data Assimilation in Sea-Ice Models

Data assimilation of sea ice observations has been carried out for 15 years. Since Arctic-wide satellite derived sea-ice concentration and drift have been recorded an adequate temporal and spatial coverage of observations can be used for sea-ice data assimilation. The concentration has been recorded since 35 years (e.g. *Bjørgo et al.* (1997); *Comiso et al.* (1997); *Cavalieri et al.* (2003)), the drift is derived either by buoy trajectories recorded since 1979 (*Ortmeyer and Rigor*, 2004) or derived by passive microwave satellite data which are partially available since the mid 1980s (*Agnew and Le*, 1996; *Emery et al.*, 1997; *Kwok et al.*, 1998). The concentration is available throughout the year. In contrast, the sea-ice drift from satellite is observable with sufficient quality only in winter months, when the sea-ice surface is dry and no melting occurs because the passive microwave data are not much affected by clouds but melt ponds and wet snow alter the signal. Therefore, often buoy derived sea-ice drift is used as data base for summer sea-ice drift assimilation (*Meier et al.*, 2000; *Meier and Maslanik*, 2001a; *Zhang et al.*, 2003). Another important sea-ice property, the thickness or volume, can not be assimilated yet due to lack of temporal and spatial coverage of sea-ice thickness observations. Therefore, it is aspired to improve the representation of sea-ice thickness and its variability by sea-ice concentration or drift data assimilation.

The studies of sea-ice concentration and velocity assimilation have been carried out mostly based on Optimal Interpolation (OI) schemes but also by Kalman methods. Here, some of these studies are presented to give a brief review of the recent scientific progress on sea-ice data assimilation.

A Kalman smoothing method has been applied by *Thomas and Rothrock* (1989, 1993) to assimilate microwave sea-ice concentration data. They have used a simple sea ice model which is forced by optimally interpolated buoy motions to obtain independent model derived sea-ice concentration estimates which are blended with the sea-ice concentration data. This work has been extended by *Thomas et al.* (1996) by additional sea-ice thickness computation. They utilize observed sea-ice motions, winds and concentration plus a thermodynamic sea-ice model to produce spatially and temporally varying Arctic sea-ice thickness distributions. A comparison with submarine-derived ice draft data reveals that the Arctic wide thickness estimates agree well with the observations but exhibit less spatial variability.

Data Assimilation of microwave sea-ice concentration data with an Ensemble Kalman Filter (EnKF) has been presented by *Lisæter et al.* (2003). They assimilate these data into a general circulation model of the Arctic ocean. The sea-ice concentration assim-

ilation is shown to be applicable to modify model sea ice concentration but does not deliver useful conclusions for the thickness.

Lieser (2004) has assimilated Special Sensor Microwave Imager (SSM/I) satellite derived sea-ice concentration data into a stand-alone sea-ice model via an OI scheme to optimize sea-ice conditions for a short term sea-ice forecast (5-10 days). It is mentioned that the sea-ice volume is directly related to the concentration and a corresponding variation of the volume is required regarding the assimilated concentration. Here, the thickness has been conserved and the volume and concentration are varying during the assimilation procedure. Then the sea-ice concentration prediction has been improved by 10% due to the assimilation.

The study of *Meier et al.* (2000) was the first attempt to assimilate sea-ice velocities into a large scale sea-ice model for the Arctic to maximize the accuracy of the model. An OI scheme has been applied to assimilate the sea-ice velocity. They have found that the assimilation substantially reduces the error standard deviation and enhanced the correlations of simulated motions relative to the buoy drift. However, the assimilation indicates unrealistic changes of the sea-ice thickness near the Greenland coast and Canadian Archipelago and in the mass outflow in the Fram Strait.

Other studies of *Meier and Maslanik* (2001a,b) have shown that the data assimilation is applicable for improving model estimation of buoy trajectories and for synoptic events of Arctic sea-ice velocities.

Arbetter et al. (2002) have combined satellite-derived and modeled sea-ice velocities in a large-scale Arctic sea-ice model to simulate the anomalous summer sea ice retreat in 1990 and 1998. In both years the simulated sea-ice extent seems to be in better agreement with the observations when sea-ice velocities are assimilated but excessive sea-ice melt occurs in central ice pack.

Meier and Maslanik (2003) have further investigated effects of local conditions, namely proximity to the coast, sea-ice thickness and wind forcing, on Arctic remotely sensed, modeled and assimilated sea-ice velocities. It has been found that the OI assimilation technique has improved the quality of sea-ice motion throughout most ranges of the wind speed and sea-ice thickness in coastal and non-coastal regions. The results suggest that the use of assimilation weights optimized for typical environmental conditions would further reduce errors and yield larger benefits from the assimilation.

In a recent study *Dai et al.* (2006) have analyzed the model sensitivity to ice strength parameterization by assimilating sea-ice velocities. It has been found that many parameters have little effect on assimilation results because the assimilation essentially bypasses the model dynamics. The issue of excessive summer sea-ice retreat is reported which is caused by the assimilation procedure. It is suggested that a feature emerging in summer is not well represented in the model dynamics and the assimilation leads to increased divergences which may bypass the model's physical assumptions.

Zhang et al. (2003) have conducted a hindcast simulation of Arctic sea-ice variations of the period 1992-1997 with a regional sea-ice ocean general circulation model where buoy and passive microwave sea-ice motion data are assimilated utilizing an OI scheme. The assimilation leads to an improved motion and substantially decreased stoppage which strengthened the ice outflow in the Fram Strait and enhanced ice deformation. Ice

draft is thus slightly closer to submarine draft measurements. *Lindsay et al.* (2003) have extended this work for a ten month period in 1997 and 1998. Comparisons of ice velocity data from the Radarsat Geophysical Processor System (RGPS) with the model velocities show an enhanced agreement of model results with assimilated velocities. However, the deformation results with assimilation are in only modest agreement with observations suggesting that the model features require further improvements.

Lindsay and Zhang (2006) have also extended the work of *Zhang et al.* (2003) by incorporating in their model of the Arctic ice-ocean system a nudging scheme using a nonlinear weighting function to assimilate passive microwave sea-ice concentration data. They have found that by assimilation of the sea-ice concentration alone the ice draft bias increases especially in the marginal seas but the correlation with ice draft measurements is improved. When ice velocity and concentration are assimilated an improvement in ice draft has been obtained although a significant bias remains in the large-scale sea ice thickness pattern. *Lindsay and Zhang* (2005) have applied this experimental set-up to investigate the recent changes in the Arctic ice pack.

Dulière and Fichefet (2007) and *Dulière* (2007) have assimilated sea-ice concentration and velocity into a simplified model of the Arctic sea-ice pack and have analyzed various twin experiments to study to what degree the assimilation of sea ice velocity and/or concentration data improves the global performance and reduces errors in sea-ice thickness estimation. They have utilized a simply OI scheme. The results indicate that under certain conditions, depending on assimilation weights and type of model error, the sea-ice velocity assimilation improves the model performance. The assimilation of concentration data is also helpful but has to be handled with care due to its strong connection to the sea-ice thickness already discussed by *Lieser* (2004). They suggest that in course of the assimilation the ice volume must not be conserved in the process of adding or removing ice to better fit the observed ice concentration.

Sea-ice data assimilation can be applied to improve sea ice model behavior as well as to optimize short-term sea-ice forecast. Other purposes for sea-ice assimilation can be improvement of sea ice transport estimates and investigation of the influence of the transport on the sea-ice thickness as well as the investigation of sea-ice export especially during synoptic scale drift events.

The problem in the assimilation of sea-ice drift so far has been that - compared to the sea-ice thickness or concentration - the ice drift has a larger short-term variability depending on wind, ocean, and internal ice stresses. Since the inertia of sea ice is small compared to the stresses, the system has very little memory beyond each model time step, making simple drift field corrections very short-lived. Therefore, even a perfectly corrected drift field has very little effect on the residual model state. However, ice-drift history is stored in the sea-ice thickness and concentration distributions.

In previous studies the sea-ice velocities have been assimilated by OI schemes. These modified fields are used to determine sea ice trajectories (*Meier and Maslanik*, 2001b), to compute the transport or advection of sea ice (*Dulière and Fichefet*, 2007), or to solve the thickness distribution of ridged and undeformed sea ice (*Zhang et al.*, 2003). In all of these cases the modified velocity fields have been used to determine advection of sea ice which leads to modified thickness and concentration distributions.

Another approach is to modify the whole model state by drift assimilation based on the knowledge of model results and observations and corresponding error estimates, covariances, and cross-correlation. Such a statistical approach to the redistribution of sea ice utilizes the Singular Evolutive Interpolated Kalman (SEIK) Filter (*Pham et al.*, 1998a; *Pham*, 2001). By considering the covariance of sea-ice thickness and drift as well as the covariance of sea-ice concentration and drift, the SEIK filter is able to modify the more conservative state variables "ice thickness" and "ice concentration" during the course of assimilation, which in turn leads to modifications of the large-scale sea-ice distribution. Already at this point it is clear that a sustainable velocity improvement is dependent on total sea ice state improvement.

The aim of this thesis is the assimilation of observed sea-ice velocity data into the regional Finite Element Sea Ice Model (FESIM) for the Arctic utilizing the SEIK Filter to analyze sea-ice dynamic behavior. This is a first exploration of the effects of the assimilation procedure on the model performance rather than a climate study based on improved sea-ice drift.

This thesis is structured as follows: first the resources for the data assimilation are described in Chapter 2. It comprises the description of the Finite Element Sea-Ice Model, the Singular Evolutive Interpolated Kalman Filter and the remotely sensed drift data which are used for the data assimilation, and buoy drift, sea-ice thickness observations and remotely sensed concentration which are utilized for the validation for the assimilation results. Then the sea-ice model reference simulation is presented in Chapter 3, which is used for the comparison with the assimilation results shown in Chapter 4. Here, the applied SEIK Filter setup, two case studies, the ensemble variability, the mass conservation in course of the assimilation and results of a local SEIK Filter setup are presented and discussed. At least the conclusions are drawn including suggestions for future work.

2 Tools and Resources: Sea-Ice Model, SEIK Filter and Sea-Ice Observations

This chapter comprises the descriptions of the sea-ice model, of the Singular Evolutive Interpolated Kalman (SEIK) Filter which is utilized to perform the sea-ice assimilation, and the observational data which are used for the assimilation and observations used for validation as well.

2.1 The Sea-Ice Model

In order to simulate the large-scale behavior of sea ice, the evolution of the atmosphere and ocean as well as thermodynamical and dynamical properties of the sea ice itself have to be considered by a numerical model. To take into account the influence of atmosphere and ocean on the state of the sea ice, a sea-ice model is either forced with atmospheric and oceanic data or coupled to ocean and/or atmospheric models. In order to maintain less computational cost in course of the assimilation procedure a mixed layer sea-ice model based on the Finite Element Sea-Ice Ocean Model (*Danilov and Yakovlev*, 2003; *Danilov et al.*, 2004) is applied which is forced by atmospheric and ocean data, cf. Section 2.1.4.

The dynamics of the sea-ice model is based on the viscous-plastic rheology approach (*Hibler*, 1979) and the more recent elastic-viscous-plastic rheology approach proposed by *Hunke and Dukowicz* (1997). The thermodynamics follows the work of *Semtner* (1976) with the zero-layer approach for heat conduction through the sea ice, and a budget of heat exchange with atmosphere and ocean from *Parkinson and Washington* (1979). Furthermore the model computes a prognostic snow layer which is based on *Owens and Lemke* (1990) and has an important effect on sea-ice atmosphere interactions. The sea-ice model has the finite element set-up of *Danilov and Yakovlev* (2003). This leads to a grid construction which is represented by triangular elements where the solution of the momentum balance differential equation is solved with the Finite Element Method (FEM). The ice-ocean interaction follows the equation suggested by *Timmermann et al.* (2002).

Here, the general assumptions and parameters for a large scale sea-ice model are presented in Section 2.1.1, followed by the specific physics for the model in Section 2.1.2, which include thermodynamic and dynamic processes and the sea-ice rheology. The principles of the finite elements are described in Section 2.1.3.

2.1.1 Introduction to a Large-Scale Sea-Ice Model: Variables, Continuum Hypothesis and Balance Equations

A large-scale model should represent the physical properties occurring on large scales. Effects of small-scale features on large scales presented in the model should be parameterized. Therefore the model studies are bound on the specified scale, and can not produce reliable results for effects or evolution of small scale properties. For example, in a large-scale sea-ice model a single sea-ice flow can not be represented with believable attributes.

Prognostic Variables

The sea ice is described with only a few variables which represent large-scale properties, such as the sea-ice extent, thickness and velocity as well as the snow thickness which covers the ice surface. The variables sea-ice volume per unit area h, snow volume per unit area h_s, sea-ice concentration A, and drift velocity $\mathbf{u}$ are in current use. They vary spatially and temporally.

- The sea-ice volume per unit area, h, is the mean sea-ice thickness averaged over the extent of a grid cell. If the sea-ice coverage is homogeneous over the whole grid cell, h would be the sea-ice thickness. Its dimension is a height, and the unit is in meters.

- The snow volume per unit area, h_s, is similar to the sea-ice volume h. h_s represents the mean snow thickness averaged over the extent of a grid cell. Dimension and unit are the same as for sea-ice volume.

- The sea-ice concentration, A, represents the grid cell fraction of sea-ice cover. It is dimensionless and has a value between 0 - no sea ice, open water - and 1 - total coverage of sea ice. With the aid of A it is possible to determine the expected or actual thickness $\hat{h}$ of floes,

  $$\hat{h} = \frac{h}{A} \tag{2.1}$$

  and expected or actual snow thickness $\hat{h}_s$

  $$\hat{h}_s = \frac{h_s}{A} \tag{2.2}$$

  for the sea-ice covered fraction of a grid cell.

- Snow and sea ice are advected with the drift velocity $\mathbf{u} = (u, v)$ with the zonal and meridional components u and v, respectively. Usually the ice pack consists of floes, but at large scale it is described as a continuum with flowing velocity $\mathbf{u}$. The unit is m s^{-1}.

Continuum Approximation

For the climate system the exact position and form of a single floe is less important than the ratio of sea ice and open water in a region which can be represented by such a large scale sea-ice model. Therefore, for large-scale analysis it is assumed that the sea-ice concentration is a continuous and continuously differentiable function of space and time, and is defined as:

$$A = \frac{1}{F_R} \iint\limits_R I(x,y)\mathrm{d}x\mathrm{d}y, \tag{2.3}$$

over a sea-ice covered area in a region R with the surface F_R

$$F_R = \iint\limits_R 1\mathrm{d}x\mathrm{d}y. \tag{2.4}$$

In Equation (2.3), $I(x,y)$ is the sea-ice indicator at the point (x,y) and has a value of 1, if this point is covered with sea ice, else it is 0.

For large-scale models with a grid-cell area of more than approximately 100 square kilometers the continuum hypothesis is a good approximation because a single grid cell is large enough to exceed typical dimensions of single sea-ice floes. Given a typical floe size, a lower limit for grid cell size seems to be 25 square kilometers (5 km $\times$ 5 km) for a large scale sea-ice model.

Balance Equations

The temporal and spatial evolution of the prognostic variables are determined by balance equations. Extent, volume and velocity of sea ice are dominated by two general processes: thermodynamic growth and advection of sea ice.

Thermodynamic growth is the source of sea ice. Sea ice is produced when the cold atmosphere in the polar regions has cooled down the upper ocean layer to the freezing point of sea water, which is approximately a temperature of $T_f \approx -1.87\,^{\circ}\mathrm{C}$, and the atmosphere is continuing to cool. Energy is delivered to the atmosphere by phase transition from liquid to solid state and latent heat is released into the atmosphere. Further cooling leads to decreasing ice temperatures at the surface and basal freezing which lead to a temperature gradient in the ice. Sea ice melts at its lateral and basal surfaces if the water temperature is above the freezing temperature T_f and the ice is already heated up to the freezing point. At the surface sea ice is heated and melted by absorbing solar radiation and long wave radiation which is emitted by clouds. So it is clear that the thermodynamic growth is based on the energy balance of the ocean-atmosphere boundary layer. In short: sea-ice growth and melt is determined by net energy balance of the atmosphere-ice-ocean boundary layer. If this energy balance is zero then the sea-ice volume is conserved.

Advection, transport of sea-ice volume via drift, modifies the spatial distribution of sea-ice volume. The balance equations combine both processes of sea-ice growth and

advection:

$$\frac{\partial h}{\partial t} + \nabla \cdot (\mathbf{u}h) = S_h, \tag{2.5}$$

$$\frac{\partial h_s}{\partial t} + \nabla \cdot (\mathbf{u}h_s) = S_{h_s}, \tag{2.6}$$

$$\frac{\partial A}{\partial t} + \nabla \cdot (\mathbf{u}A) = S_A. \tag{2.7}$$

The left-hand sides of these equations look like a continuity equation where the first term corresponds to the local change of time and the second term to the advection, where ice volume is advected out of or into neighboring regions. The S-terms on the right hand sides represent sources and sinks of these prognostic variables and when these terms are zero, the variables are conserved quantities.

2.1.2 Sea-Ice Physics

Various processes depend on the large-scale properties of sea ice. The extent and compactness of sea ice, described by its concentration, is important for the heat flux between atmosphere and ocean. The sea-ice thickness is important for dynamic processes especially for the internal strength of the sea ice. The thicker and more compact the ice is the higher is the internal force to resist the drag of atmosphere and ocean. The deformation of sea ice which results in thickness changes is estimated on a large-scale with the rheology approach which regards the sea ice as a flowing object. This section describes the thermodynamic and dynamic processes including the rheology of sea ice on which the physical sea ice model is based.

Thermodynamics of the Atmosphere - Sea Ice - Ocean Boundary

Sea ice is mainly produced in autumn and winter. New ice forms and already existing sea ice grows thermodynamically to an upper limit of approximately 2.5 - 3 m (*Maykut and Untersteiner*, 1971). This is defined by a balance of heat transfer between atmosphere and ocean through the ice. The thermodynamic changes of sea-ice coverage and volume in space and time can be described with the energy balance at the sea-ice surface and bottom of sea ice.

Energy Balance: The thermodynamic of the air-(snow-)sea-ice-ocean layer is determined by the heat fluxes from the atmosphere and ocean and a heat conduction through the sea ice. In case of open water the term for the heat conduction vanishes.

Based on *Parkinson and Washington* (1979) this energy balance can be written as:

$$Q_a + Q_o + \rho_{\mathrm{i}} L_i \left(\frac{\partial h}{\partial t} \right) = 0. \tag{2.8}$$

Here, Q_a and Q_o are the heat fluxes of the atmosphere and the ocean, respectively - they are positive for heat flux into the sea ice - ρ_{i} and ρ_{s} are the densities of sea ice and

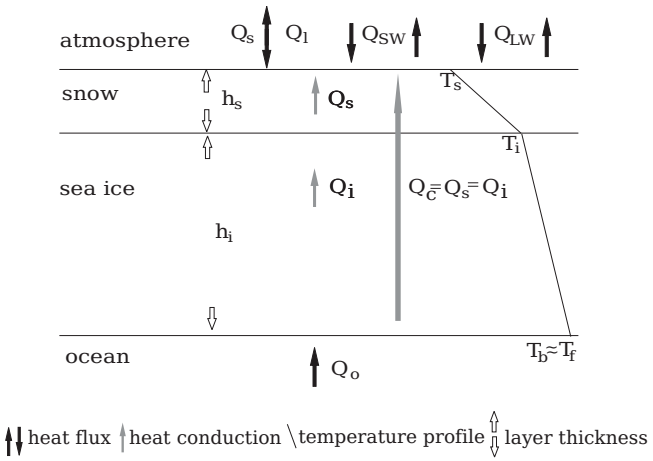

Figure 2.1: Scheme of the heat transfer at the atmosphere-ice-ocean boundary after the thermodynamic model from *Semtner* (1976) and *Parkinson and Washington* (1979) with: Q_s sensible heat flux, Q_l latent heat flux, Q_{SW} short wave radiation, Q_{LW} long wave radiation, h_s snow thickness, Q_s heat conduction through the snow, T_s snow temperature, h_i sea-ice thickness, Q_i heat conduction through the sea ice, T_i sea-ice temperature, Q_o ocean heat flux, T_b ice-ocean interface temperature, T_f freezing point temperature.

snow, and L_i the specific latent heat for phase transition (liquid $\leftrightarrow$ solid). The values of these constant parameters can be seen in Table 2.2.

Atmospheric Heat Flux at the Sea-Ice Surface: The energy budget at the ocean or sea-ice surface is described by the heat transfer of the atmosphere into the water or ice, respectively,

$$Q_a = Q_{SW\downarrow} + Q_{SW\uparrow} + Q_{LW\downarrow} + Q_{LW\uparrow} + Q_s + Q_l, \tag{2.9}$$

with the downward and upward long- and short wave radiation $Q_{LW\downarrow}$, $Q_{SW\downarrow}$ and $Q_{LW\uparrow}$, $Q_{SW\uparrow}$, respectively, and the sensible and latent heat fluxes Q_s and Q_l. The short wave solar radiation is determined by an empiric formula that has been developed by *Zillman* (1972) which assumes a clear sky and a correction for cloudiness[1] (*Laevastu*, 1960). It depends on the position of the sun, which varies with the daily and seasonal cycles, and the state of the atmosphere. Then the solar irradiation $Q_{SW\downarrow}$ is defined as:

$$Q_{SW\downarrow} = S_0 \cdot \frac{\cos^2 Z}{(\cos Z + 2.7)\, e_v \cdot 10^{-5} + 1.085 \cos Z + 0.1} \cdot \left(1 - A_c^3\right), \tag{2.10}$$

with $S_0 = 1368\,\mathrm{W\,m^{-2}}$ the solar constant, Z the solar zenith angle, and e_v the partial pressure of water vapor in the air. The zenith angle Z depends on the latitude φ, declination δ of the sun and the hour angle α_h:

$$\cos Z = \sin\varphi \sin\delta + \cos\varphi \cos\delta \cos\alpha_h. \tag{2.11}$$

[1]This procedure has been described in detail by *Parkinson and Washington* (1979).

Table 2.1: Albedo values for different surface types.

surface type	albedo α
frozen snow	0.85
melting snow	0.75
ice without snow layer	0.75
melting ice	0.66
open water	0.10

The shortwave, reflected radiation is defined as

$$Q_{SW\uparrow} = \alpha Q_{SW\downarrow}, \tag{2.12}$$

where α is the albedo. It defines the ability of a surface to reflect solar radiation. In Table 2.1 different types of surfaces and their empirically determined albedo (*Fischer*, 1995) are listed.

Incoming long wave radiation $Q_{LW\downarrow}$ is defined by the Stefan-Boltzmann law:

$$Q_{LW\downarrow} = \epsilon_a \sigma T_a^4, \tag{2.13}$$

where T_a is the air temperature at height of 2 m, σ the Stefan-Boltzmann constant, and ϵ_a the emissivity of the atmosphere in the infrared. For ϵ_a, *König-Langlo and Augstein* (1994) have found an empirical formula as a function of the cloud coverage A_c:

$$\epsilon_a\left(A_c\right) = 0.765 + 0.22 \cdot A_c^3. \tag{2.14}$$

The long wave, thermal radiation, coming from the surface of water or sea ice, is a function of surface temperature T_s:

$$Q_{LW\uparrow} = \epsilon_s \sigma T_s^4. \tag{2.15}$$

The surface emissivity ϵ_s is assumed to be constant for sea ice and open water. The surface temperature, however, is different for sea ice and open water.

The sensible and latent heat flux, Q_s and Q_l, are calculated from bulk formulae:

$$Q_s = \rho_a c_p C_s \mid \mathbf{u}_a \mid \left(T_a - T_s\right), \tag{2.16}$$

$$Q_l = \rho_a L C_l \mid \mathbf{u}_a \mid \left(q_a - q_s\right), \tag{2.17}$$

with ρ_a air density at 2 m height, c_p its specific heat capacity, C_s the turbulent heat transfer coefficient for sensible heat; $\mathbf{u}_a$ is the wind velocity at 10 m height, T_a the air temperature at 2 m height and T_s the surface temperature; L is the specific heat of evaporation of water or sublimation of ice, C_l is the turbulent heat transfer coefficient

Table 2.2: Parameters for the thermodynamic sea-ice model

Parameter	Symbol	Value
latent heat conduction coefficient	C_l	1.75
sensible heat conduction coefficient	C_s	1.75
sensible heat transfer coefficient	c_h	10^{-4}
specific heat capacity of air	c_p	$1004\,\mathrm{J\,kg^{-1}K^{-1}}$
surface emissivity sea ice or snow	ϵ_s	0.97
lead closing parameter	$h0$	1.0 m
heat conductivity of ice	κ_i	$2.17\mathrm{W\,m^{-1}K^{-1}}$
heat conductivity of snow	κ_s	$0.31\mathrm{W\,m^{-1}K^{-1}}$
specific heat (evaporation)	L	$2.5 \cdot 10^6\mathrm{J\,kg^{-1}}$
specific heat (sublimation)	L	$2.834 \cdot 10^6\mathrm{J\,kg^{-1}}$
specific latent heat	L_i	$3.34 \cdot 10^5\,\mathrm{J\,kg^{-1}}$
density of air in 2 m height	ρ_a	$1.3\,\mathrm{kg\,m^{-3}}$
density of sea ice	ρ_i	$910\,\mathrm{kg\,m^{-3}}$
density of water	ρ_o	$1025\ \mathrm{kg\tilde{m}^{-3}}$
density of snow	ρ_s	$290\,\mathrm{kg\,m^{-3}}$
Stefan-Boltzmann constant	σ_B	$5.67 \cdot 10^{-8}\mathrm{W\,m^{-2}K^{-4}}$
freezing temperature of freshwater	$T_{f,a}$	0°C
freezing point of sea water	T_f	
depending on salinity S (*Gill*, 1982)	$T_f(S)$	$= -0.0575S + 1.7105 \cdot 10^{-3}\sqrt{S^3} - 2.155 \cdot 10^4 S^2$
air pressure	P_a	1013 hPa

of latent heat, q_a the specific humidity at 2 m height, and q_s the specific humidity at the ocean or sea ice surface. The specific humidities are determined by

$$q_a = 0.622\frac{p_v}{P_a - (1-0.622)p_v} \approx 0.622\frac{p_v}{P_a} \tag{2.18}$$

with p_v the partial pressure of water vapor in the air and the air pressure P_a. The value 0.622 is the average ratio of the molecular weights of water vapor and dry air (*Parkinson and Washington*, 1979). The partial pressure p_v is determined by an empirical formula proposed by *Murray* (1967) from the dew point temperature T_{dew},

$$p_v = 6.11\,\mathrm{hPa}\ \mathrm{e}^{\frac{21.9\cdot T_{dew}}{T_{dew}+265.5}}. \tag{2.19}$$

For the specific humidity q_s it is assumed that the air mass at the surface is always saturated and is determined similarly as q_a (Equation (2.18)) but with the sea-ice or ocean surface temperature T_s.

Heat Conduction: The heat transport through the ice takes place in the form of heat conduction. Then the energy balance, Equation (2.8), can be divided in two separate

formulas (*Semtner*, 1976):

$$Q_a + Q_c + \rho_{\mathrm{i}} L_i \left(\frac{\partial h}{\partial t}\right)_a = 0, \tag{2.20}$$

$$Q_o - Q_c + \rho_{\mathrm{i}} L_i \left(\frac{\partial h}{\partial t}\right)_o = 0. \tag{2.21}$$

Equation (2.20) describes the balance of heat transfer at the atmosphere-ice interface, and the Equation (2.21) at the sea-ice-ocean boundary. Here, Q_c is the conductive heat flux through the sea ice (and snow if present). The zero layer model of *Semtner* (1976) assumes that the sea ice and snow have no heat capacity and so the conductive heat flux is constant in vertical direction. A linear temperature profile through the ice results. In case of a snow layer there are two different heat conductivities, sea-ice and snow heat conductivity κ_i and κ_s, which result in two different temperature gradients. As it is shown in Figure 2.1 the conductive heat flux of ice, Q_i, and snow, Q_s, is assumed to be the same and equal to the entire conductive heat flux Q_c:

$$Q_c = Q_i = \frac{\kappa_i \left(T_b - T_i\right)}{h_i} = Q_s = \frac{\kappa_s \left(T_i - T_s\right)}{h_s}. \tag{2.22}$$

After eliminating the temperature at the ice-snow boundary layer, T_i, and introducing the effective thermodynamic ice thickness, h^*, considering the insulation effect of snow:

$$h^* = h_i + h_s \frac{\kappa_i}{\kappa_s}, \tag{2.23}$$

the conductive heat flux becomes

$$Q_c = \frac{\kappa_i \left(T_b - T_s\right)}{h^*}. \tag{2.24}$$

The bottom temperature, T_b, is assumed to be at the freezing point. From Equations (2.23) and (2.24) it can be seen that the heat transfer through the ice decreases with increasing snow and ice thickness. When no ice is present T_b and T_s coincide and Q_c becomes zero.

Oceanic Heat Flux: The heat flux between ocean and sea ice is parameterized as

$$Q_{o_{\mathrm{ice}}} = \rho_o c_p c_h u_* \left(T_o - T_f\right), \tag{2.25}$$

with ρ_o density of ocean water, c_p its specific heat capacity at constant pressure, and c_h coefficient for turbulent heat transfer between the ocean and the bottom of sea ice. u_* is the friction velocity which is defined as

$$u_* = \sqrt{c_o} \mid \mathbf{u}_o - \mathbf{u} \mid, \tag{2.26}$$

with $\mathbf{u}_o$ the velocity in the upper ocean layer, $\mathbf{u}$ the sea-ice velocity and c_o the oceanic drag coefficient. The temperature difference in Equation (2.25) is the difference between temperature at the upper ocean layer, T_o, and freezing point temperature, T_f. For the

open water part of each grid cell the surface heat flux Q_{o_s} is computed after *Parkinson and Washington* (1979). If the surface of the ocean has been cooled down to the freezing temperature additional heat loss is converted into sea-ice formation.

The total ocean surface heat flux Q_o then is computed as a weighted average

$$Q_o = (1 - A)Q_{o_\mathrm{s}} - AQ_{o_\mathrm{ice}} \tag{2.27}$$

depending on ice concentration A.

Due to the insulating effect of sea ice the heat flux between ocean and atmosphere can differ by up to two order of magnitudes in areas of open water and a thick ice cover. Consequently, thinner sea ice allows a larger heat exchange than thicker ice. Taking varying sea-ice thicknesses within a grid cell into account seven ice class categories are implemented with evenly distributed ice thickness in the interval between 0 and $2h/A$. The thermodynamic energy balance is then solved for every thickness class separately and the corresponding net heat fluxes are added. The energy balance for open water is solved directly.

Thermodynamic Growth When the energy budget produces a surface temperature T_s larger than zero degree Celsius, T_s is set to zero and the energy balance is computed again. The excess of energy at the sea-ice surface is used to melt snow or ice. Melting of snow and sea-ice can then be described as:

$$\frac{\partial h_s}{\partial t} = -\frac{Q_a + Q_c}{\rho_s L_i}, \tag{2.28}$$

$$\left(\frac{\partial h}{\partial t}\right)_a = -\frac{Q_a + Q_c}{\rho_i L_i} - \frac{\partial h_s}{\partial t}. \tag{2.29}$$

Here, it is assumed that first all snow is melted and once no more snow is present then the sea-ice thickness is decreased. Equation (2.29) describes the sea-ice thickness change depending on atmospheric heat fluxes.

Melting and formation of sea ice at the bottom of the sea ice can be described analogous to Equation (2.29),

$$\left(\frac{\partial h}{\partial t}\right)_o = -\frac{Q_o - Q_c}{\rho_i L_i}. \tag{2.30}$$

For the open water fraction Equations (2.29) and (2.30) reduce to one equation because no snow is present and Q_c is zero:

$$\left(\frac{\partial h}{\partial t}\right)_{ow} = -\frac{Q_{o_s}}{\rho_i L_i}. \tag{2.31}$$

In sum, thermodynamic ice growth is written as:

$$\frac{\partial h}{\partial t} = A\left(\frac{\partial h}{\partial t}\right)_a + A\left(\frac{\partial h}{\partial t}\right)_o + (1 - A)\left(\frac{\partial h}{\partial t}\right)_{ow}, \tag{2.32}$$

which is positive defined for freezing and negative for melting.

Table 2.3: Empirical parameters for the dynamic sea-ice model.

Parameter	Symbol	Value
Atmospheric drag coefficient		
atmosphere - ice	c_a	$1.32 \cdot 10^{-3}$
Oceanic drag coefficient		
atmosphere - ocean	c_{ao}	$1.0 \cdot 10^{-3}$
ocean - ice	c_{io}	$3.0 \cdot 10^{-3}$
Eccentricity of the elliptical yield curve	e	2
Sea-ice strength parameter	$P^\star$	15000
Sea-ice concentration parameter	C	20

Modification of the sea-ice thickness alters the sea-ice concentration following

$$\left(\frac{\partial A}{\partial t}\right)_{td} = \frac{1-A}{h_0} \max\left(\frac{\partial h}{\partial t}, 0\right) + \frac{A}{2h} \min\left(\frac{\partial h}{\partial t}, 0\right). \tag{2.33}$$

h_0 is an empiric parameter which determines the closing rate of leads when sea ice is produced. For melting it is assumed to have a uniformly distributed sea-ice thickness between zero and $A/2h$.

Dynamics of Sea Ice

Sea-ice motion is driven by wind stress and ocean currents. Sea-ice drift is described by the sea-ice velocity $\mathbf{u}$. Its magnitude does not depend on the wind stress or ocean velocities alone but it also highly depends on sea-ice compactness. Only a compact sea-ice cover is able to produce substantial resistance to external stresses. The empirical parameters which address the sea-ice dynamics and rheology are similar to those of *Kreyscher et al.* (2000) and are listed in Table 2.3.

The sea-ice velocity is determined by the forces acting on the sea ice. This can be described by the momentum balance (*Hibler*, 1979):

$$m\frac{\mathrm{d}\mathbf{u}}{\mathrm{d}t} = \mathbf{F} = \tau_a + \tau_o + \mathbf{F}_I + \mathbf{F}_C + \mathbf{F}_H \tag{2.34}$$

with m mass per unit area of the sea ice, $\mathbf{u}$ sea-ice velocity, t time, $\mathbf{F}$ total force, τ_a atmospheric shear stress caused by the wind, τ_o oceanic shear stress caused by the ocean currents, $\mathbf{F}_I$ internal force, $\mathbf{F}_C$ Coriolis force introduced by the use of a rotating reference frame, and $\mathbf{F}_H$ force caused by the oceanic surface tilt relative to the surface of the geoid. The air stress is described by the wind velocity $\mathbf{u}_a$ at 10 m height

$$\tau_a = \rho_a c_a \mid \mathbf{u}_a \mid \mathbf{u}_a, \tag{2.35}$$

where ρ_a is the air density at sea or ice surface, and c_a is the atmospheric drag coefficient. The ocean stress at the ice-ocean interface is described with the bulk formula:

$$\tau_{io} = \rho_o c_{io} \mid \mathbf{u}_o - \mathbf{u} \mid ((\mathbf{u}_o - \mathbf{u}) \cos\vartheta + \mathbf{k} \times (\mathbf{u}_o - \mathbf{u}) \sin\vartheta), \tag{2.36}$$

with c_{io} turbulent drag coefficient and ϑ water turning angle between direction of τ_o and $\mathbf{u}_o - \mathbf{u}$ and is assumed as zero in the recent model algorithm. For the ice-free ocean the formula is described as

$$\tau_{ao} = \rho_a c_{ao} \mid \mathbf{u}_a \mid \mathbf{u}_a. \tag{2.37}$$

It is assumed that for Equations (2.35) and (2.37) the ice drift and ocean surface velocities are negligible compared to the 10 m wind speed of the atmosphere (*Hibler*, 1979), and the relative velocity of wind and ice or ocean surface is essentially the wind velocity, and that the surface stress and the 10 m wind are parallel. A grid cell may be partly covered with ice such that the total ocean surface stress is calculated as an area weighted average:

$$\tau_o = A \cdot \tau_{io} + (1 - A) \cdot \tau_{ao}. \tag{2.38}$$

The Coriolis force[2] is defined as:

$$\mathbf{F}_C = -mf\mathbf{k} \times \mathbf{u}, \tag{2.39}$$

with the Coriolis parameter

$$f = 2\Omega \sin\varphi, \tag{2.40}$$

depending on the earth rotation frequency $\Omega = 7.29 \cdot 10^{-5}\mathrm{s}^{-1}$ and geographic latitude φ.

The sea surface dynamic height, ∇H, is the tilt of the sea surface with respect to the constant surface potential of the geoid and causes a force into the direction of the negative gradient of the dynamic height:

$$\mathbf{F}_H = -mg\nabla H, \tag{2.41}$$

with g being the acceleration of gravity. The internal forces are discussed separately in the following paragraph.

Rheology of Sea Ice

Deformation processes of sea ice are described within the continuum approximation that is called rheology, the law of flux and deformation of objects which means the relative motion of the particles of the objects. The rheology of sea ice has an important influence on the dynamics of sea ice. Sea-ice drift is mainly caused by wind and ocean currents, but can be reduced by interacting ice floes. A convergent ice drift can result in deformation

[2]The Coriolis force is a fictitious force which appears in a rotating reference frame and has its cause in the conservation of the angular momentum. It represents an acceleration perpendicular to the direction of movement depending on the rotation velocity. That leads to the effect that linear, not accelerated motions in an inertia reference frame appear curved in a rotated reference frame.

of sea ice, e.g. rafting or ridging. Internal forces can stop locally sea-ice drift completely especially in winter season when a compact sea-ice surface often occurs over the Arctic ocean. Therefore, the rheology is an important factor in the momentum balance, see Equation (2.34). For non-interacting floes a free drift is assumed. Then a balance of atmospheric and oceanic forcing, considering Coriolis force and force of sea surface tilt, determines the drift. In this case the drift direction is correlated with the wind direction because the wind is the dominant part for the sea-ice drift regarding short-time scales (*Timmermann et al.*, 2002). On the other hand, a compact sea ice field shows a very different behavior: a reduced sea-ice velocity with a direction only weakly correlated to the wind direction.

For a realistic description of a dense sea-ice cover a formulation of the internal forces is required. In the mid 70s within the Arctic Ice Dynamics Joint Experiment (AIDJEX), extensive measurements have been performed of ice dynamics and of atmospheric and oceanic forcing at a drift station on the Arctic sea ice. In context with this project dynamic sea-ice models including internal forces have been developed (*Coon et al.*, 1974). They are based on the approach of continuum mechanics, i.e. the internal forces are described as the divergence of the stress tensor:

$$\mathbf{F}_I = \nabla \cdot \sigma. \tag{2.42}$$

The tensor $\sigma(\dot{\epsilon})$ is a function of the strain rate tensor $\dot{\epsilon} = \nabla\mathbf{u}$ containing spatial derivatives of the velocity field. The internal stress σ is a dynamic and the strain rate $\dot{\epsilon}$ is a kinematic variable. The connection between dynamics and kinematics is described by the rheology law[3] $\sigma = \sigma(\dot{\epsilon})$. The different rheological models differ in their description of the relation of internal stress and strain rate.

Kinematics of Sea Ice Kinematics of sea ice describes its motion in space and time without information of the reason for the drift. Deformation are described with a tensor containing spatial derivatives of the velocity components:

$$(\nabla\mathbf{u})_{i,j} = \frac{\partial u_i}{\partial x_j}. \tag{2.43}$$

The tensor is split into a symmetric ($\dot{\epsilon}$) and an antisymmetric (Ω) part so that $\nabla\mathbf{u} = \dot{\epsilon}+\Omega$ with

$$\dot{\epsilon}_{i,j} = \frac{1}{2}\left(\frac{\partial u_i}{\partial x_j} + \frac{\partial u_j}{\partial x_i}\right), \tag{2.44}$$

$$\Omega_{i,j} = \frac{1}{2}\left(\frac{\partial u_i}{\partial x_j} - \frac{\partial u_j}{\partial x_i}\right). \tag{2.45}$$

As already mentioned, $\dot{\epsilon}$ is the tensor of strain rates and describes the deformation without rotation and the vorticity Ω is the rotation without deformation, which is equivalent to a rotation of a solid object. In general, it is assumed that sea ice behaves dynamically

[3] An introduction to continuum mechanics is given by *Long* (1964)

like a fluid. This means that the internal forces as a response of deformation is only approximated by $\dot{\epsilon}$. The vorticity Ω does not generate internal forces.

Various rheologies have been suggested for sea ice. A widely used sea-ice rheology is the Viscous-Plastic (VP) rheology proposed by *Hibler* (1979) along with the more recent Elastic-Viscous-Plastic (EVP) rheology approach by *Hunke and Dukowicz* (1997).

Viscous-plastic model equations The viscous-plastic model equations described in this paragraph are based on the work of *Hibler* (1979). The constitutive law is proposed as

$$\sigma_{ij} = 2\eta\dot{\epsilon}_{ij} + (\zeta - \eta)\left(\dot{\epsilon}_{11} + \dot{\epsilon}_{22}\right)\delta_{ij} - \frac{P}{2}\delta_{ij}, \tag{2.46}$$

which comprises internal sea-ice stresses σ_{ij}, strain rates $\dot{\epsilon}_{ij}$ and an internal sea-ice pressure P, a variable describing sea-ice strength, and the nonlinear bulk and shear viscosities, ζ and η. Alternatively, it can be rewritten as

$$\frac{1}{2\eta}\sigma_{ij} + \frac{\eta - \zeta}{4\eta\zeta}\left(\sigma_{11} + \sigma_{22}\right)\delta_{ij} + \frac{P}{4\zeta}\sigma_{ij} = \dot{\epsilon}_{ij}, \tag{2.47}$$

with $i, j \in \{1, 2\}$ which will be useful later for comparison with EVP model equations. The VP rheology allows ice pack to diverge with little or no stress and under convergent conditions to resist compression and shearing motion. The pressure P is proposed to be a function of sea-ice thickness and compactness and is parameterized as (*Hibler*, 1979):

$$P = P^* h \exp[-C(1 - A)], \tag{2.48}$$

where P^* and C are empirical constants (cf. Table 2.3). The bulk and shear viscosities increase with internal pressure and decreasing strain rates. If the internal stresses obtain the yield point the sea ice behaves plastic and breaks and piles up. For a 2 dimensional system a yield curve instead of a yield point has to be determined. A realistic description for sea-ice delivers an elliptical yield curve that determines the non-linear viscosities (*Hibler*, 1979):

$$\zeta = \frac{P}{2\Delta}, \tag{2.49}$$

$$\eta = \frac{\zeta}{e^2}, \tag{2.50}$$

$$\Delta\left(\dot{\epsilon}\right) = \sqrt{\left(\dot{\epsilon}_{11} + \dot{\epsilon}_{22}\right)\left(1 + e^{-2}\right) + 4e^{-2}\dot{\epsilon}_{12}^2 + 2\dot{\epsilon}_{11}\dot{\epsilon}_{22}\left(1 - e^{-2}\right)}, \tag{2.51}$$

with the eccentricity e of the elliptical yield curve with an empirical value of two. Δ represents the degree of deformation rate. These parameters represent an idealized viscous-plastic material. For zero strain rate the viscosities become infinity. Regulating this behavior the viscosities are bound when strain rates are small and ice pack moves like an essentially rigid object. These limited, large viscosities make the ice pack behave like a linear viscous fluid flowing very slowly.

Elastic-Viscous-Plastic Model Equations The EVP rheology was developed in order to solve the problem of zero strain rates mentioned in the previous paragraph. *Hunke and Dukowicz* (1997) introduced a model in which the regularization of zero strain rate is a simplified elastic model whose parameters are chosen for numerical rather than physical reasons. For that, the strain rate is separated into the sum of plastic and elastic contributions. The plastic part is already defined by Equation (2.47). The elastic part is approximated by

$$\frac{1}{E}\frac{\partial \sigma_{ij}}{\partial t} = \dot{\epsilon}_{ij}, \tag{2.52}$$

where E is the modulus of elasticity or Young's modulus. It has to be mentioned that it is not a physically realistic elastic equation, but one that is simplified for use as a regularization. Adding the two contributions the strain rate, Equations (2.47) and (2.52), becomes

$$\frac{1}{E}\frac{\partial \sigma_{ij}}{\partial t} + \frac{1}{2\eta}\sigma_{ij} + \frac{\eta - \zeta}{4\eta\zeta}\left(\sigma_{11} + \sigma_{22}\right)\delta_{ij} + \frac{P}{4\zeta}\sigma_{ij} = \dot{\epsilon}_{ij}. \tag{2.53}$$

Then, if $E \to \infty$ Equation (2.47) is valid and if $\eta, \zeta \to \infty$ Equation (2.52), the elastic part, is valid. Both rheologies are implemented in the sea-ice model and the EVP rheology is applied due to numerical advantages.

2.1.3 The Finite Element Method for Solving the Momentum Balance

The Fundamental Idea of Finite Elements

Physical problems are often described in (partial) differential equations. In many cases the analytical solution of such equation is difficult to find. Therefore, a discretization is necessary for their solution. Discretization methods are based on finite differences, spectral methods or finite elements. The Finite Element Method (FEM) has been described first by *Galerkin* (1915). The idea is to convert the differential equation into an integral form, the so-called weak form. Such an integral can be described again with a sum of integrals. These integrals lead to a partition of the regarded model region into a finite number of elements on which they have to be solved. The FEM is an approximation to the solution of the differential equation.

Often in applications, these elements are used in the shape of triangles. Thus, there is no regular configuration of the elements necessary, which results in a possible application of unstructured grids. This partitioning has a defined number of nodes (points of the triangles) and elements (triangles) (Figure 2.2). Based on *Courant* (1943), the preferred solution can be determined as a so called Spline function. This means that the solution on each element is a low order polynomial, which connects continuously to the neighboring elements. Thus, for each element, a basis function is found, and only the basis functions on a node patch have to be considered, because they are defined in such a way that they are zero outside of the regarded patch. A patch ω_n of a node n contains all the surrounding elements which are connected to node n (Figure 2.2). Based on these basis

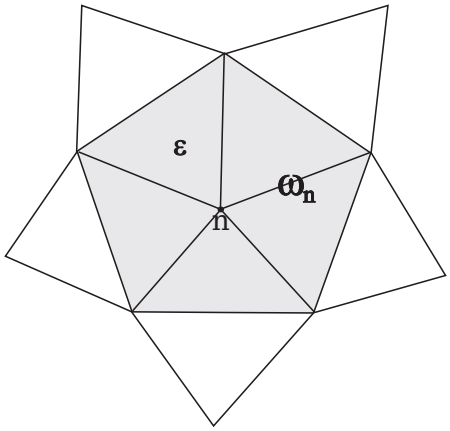

Figure 2.2: Notations for finite elements: nodes n, elements ϵ, and patches ω_n which contains all surrounding elements connected to the node n.

functions, a linear system of equations can be derived:

$$\tilde{\mathbf{A}}x = b, \tag{2.54}$$

which has to be solved. The basis functions have the advantage that they exist locally, so that the matrix $\tilde{\mathbf{A}}$ can be computed for each element because outside of the patch the basis function is zero per definition. In the simplest case the matrix can be computed analytically. Therefore, the local matrix for each element is computed and they are assembled to the global Matrix $\mathbf{A}$.

Advantage of Finite Elements

There are some advantages using finite elements as well as some disadvantages. A big advantage is the flexible regional geometry which is relatively easy to realize. The grid can be unstructured, with a higher resolution in regions of scientific interests. In the case of a sea ice model for the Arctic this area could be Fram Strait or the region near the coast where polynyas occur.

Depending on different types of finite elements, triangular or rectangular shape, and the choice of polynomials, there is a wide spectrum of applications of finite elements in physics or mathematics. Also, adaptive grids can be realized.

In general, a simple implementation using local matrices is possible only for low order finite elements. Also, generating the finite element grid can be complex because the grid is possibly unstructured and nodes can have different distances to each other. The integrals still have to be solved numerically, which results in higher computational cost.

Finite Elements Discretization in the Sea-Ice Model: FESIM

This paragraph describes the realization of the FEM in the sea-ice model, based on *Danilov and Yakovlev* (2003).

Finite elements discretization: The ice mass h - here including ice volume and snow volume - balance equations (2.5) and (2.6) is rewritten as a mass continuity equation:

$$\partial_t h + \nabla\,(h\mathbf{u}) = q, \tag{2.55}$$

where $\mathbf{u}$ is the sea-ice velocity and q are the thermodynamic sources and sinks. Equation (2.55) is treated in two steps. First, the right-hand side of the equation is set to zero to compute the advection effects. Then the mass is updated with calculating sources and sinks which is part of the conventional thermodynamic computation already described in Section 2.1.2. To solve Equation (2.55) with FEM the first step is to convert it to an integral with the help of suitable test functions $\tilde{h}$:

$$\int \tilde{h}\,(\partial_t h + \nabla(h\mathbf{u}))\,\mathrm{d}S = 0 \tag{2.56}$$

and with integration by parts the weak form is obtained:

$$\int \left(\tilde{h}\partial_t h - \nabla\tilde{h}\cdot\mathbf{u}h\right)\mathrm{d}S = -\int \tilde{h}h\mathbf{u}\,\mathbf{n}\,\mathrm{d}\Gamma. \tag{2.57}$$

Here, S is the ocean surface, Γ the boundary of S. If it is a solid boundary, the coast, ($\mathbf{u}\cdot\mathbf{n}$=0, which means no sea-ice drift at coastal nodes) or an open boundary located far from the ice covered region ($m = 0$), the boundary integral is zero. Otherwise it has to be prescribed. The right hand side of Equation (2.57) sets the boundary conditions for the problem (finally on the single element). The flux boundary conditions are called natural in the finite element formalism and appear always on the right hand side of the equation.

For the integral it is required that the equation is valid for any $\tilde{h}$ that belongs to the basis functions $\varphi_i(x,y), i = 1:N$. With the basis functions the mass is discretized and expanded in the series:

$$h(x,y) = \sum_j^N h_j\varphi_j(x,y). \tag{2.58}$$

Here, N is the total number of basis functions and h_j the corresponding coefficients. The basis functions are chosen such that they are one at the node j and decay linearly to zero at the neighboring nodes. This gives a continuous representation of h. Then the Galerkin system of equations on nodal values h_j is obtained:

$$M_{ij}\partial_t h_j + A_{ij}h_j = R_i, \tag{2.59}$$

with

$$M_{ij} = \int \varphi_i\varphi_j\mathrm{d}S\,, \quad A_{ij} = \int \nabla\varphi_i\mathbf{u}\varphi_j\mathrm{d}S\,, \quad R_i = \int \varphi_i h_j\varphi_j\mathbf{u}\,\mathbf{n}\,\mathrm{d}\Gamma. \tag{2.60}$$

R_i is non-zero if there is a mass flux through the open boundaries of the computational domain. M_{ij} is called the mass matrix of the problem. It is not diagonal but has a limited band width which is defined by the number of neighbors. Discretizing

$$\partial_t h_j = \frac{h_j^{n+1} - h_j^n}{\Delta t}, \tag{2.61}$$

where n is the index of time steps and Δt the time step duration, the matrix problem is rewritten as

$$S_{ij}h_j^{n+1} = \left(\frac{M_{ij}}{\Delta t} + A_{ij}\right) h_j^{n+1} = R_i^n + \frac{M_{ij}h_j^n}{\Delta t} \quad . \tag{2.62}$$

S_i is called the stiffness matrix of the problem and the advection step consists of solving the obtained system of equations iteratively.

Finite Element Grid for the Entire Arctic The finite element grid for the entire Arctic is derived from the regular 1/4° rotated grid of *Lieser* (2004) and *Martin* (2007). Due to the singularity at the North Pole it is rotated such that the model equator is along longitude 30° W and 150° E through the geographical North Pole and the model meridian is crossing along 120° W and 60° E so that the model North Pole is at 0° N 60° O which leads to an almost regular spatial resolution of about 25 km. However, there are no nodes on land and the representation of the coast are modified for the finite element grid setup. The Arctic grid setup is shown in Figure 2.3 with an additional section of the Lincoln Sea in the north west of Greenland. The triangular shape of the elements is clearly visible. The FESIM grid setup also comprises an ocean grid that has maximum 26 layers and the bottom topography is based on ETOPO5 (*NOAA Satellite and Information Service*, 1988).

2.1.4 Forcing

Atmospheric Forcing

The National Centers for Environmental Prediction (NCEP) supply a uniform reanalysis data base using a state-of-the-art analysis system and data from 1948 to the present (*Kistler et al.*, 2001; *Kalney et al.*, 1996). Daily averaged data sets are provided[4], which are used to force the sea ice model: the 2 m air temperature and 10 m wind velocities. The NCEP reanalysis data are gridded with a resolution of approximately 1.9° and have to be interpolated spatially onto the model grid.

Additional atmospheric boundary conditions are provided by climatological monthly means. These are the European Centre for Medium-Range Weather Forecasts (ECMWF) reanalysis monthly means of the humidity (*Gibson et al.*, 1997) with a maximum spatial resolution of 1.125° interpolated to the model grid. The climatological monthly means of the precipitation (*Vowinckel and Orvig*, 1970) and the cloudiness (*Ebert and Curry*, 1993) which have no spatial resolution, are interpolated to daily values.

A uniform NCEP atmospheric forcing including additional precipitation and other reanalysis data was tested, but gave no satisfying model results for the Arctic model setup, especially for summer month, where less ice remains due to massive melting resulting from atmospheric conditions, which has also been reported by *Timmermann et al.* (2005).

A composite of atmospheric forcing for NCEP (2 m air temperature and 10 m wind, daily), ECMWF (humidity, monthly means) reanalysis data and climatological means

[4]URL: *http://www.cdc.noaa.gov/cdc/data.ncep.reanalysis.html*

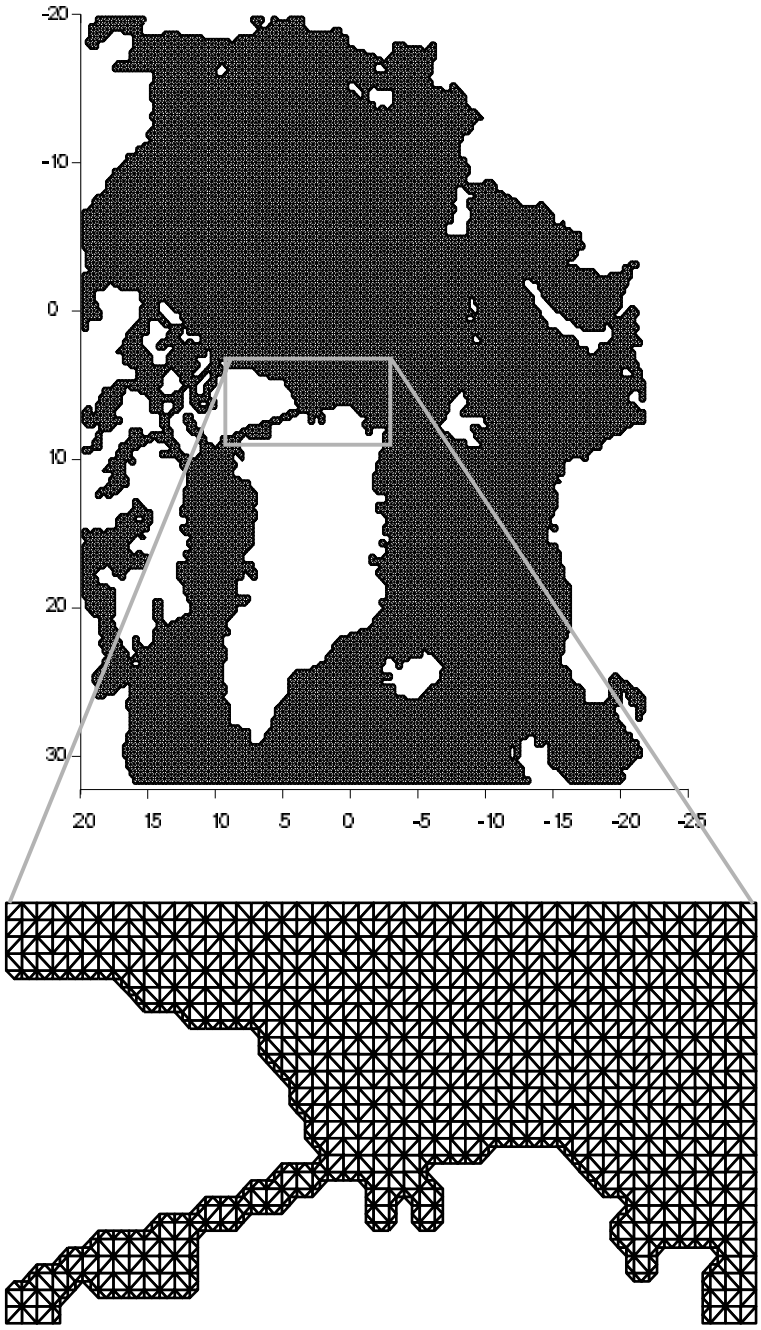

Figure 2.3: The model domain: the finite element surface grid for the entire Arctic (upper panel); the section of the Lincoln Sea is selected to show the triangular structure of the grid (lower panel)

derived from observations for precipitation and cloudiness has been found to produce a reasonable sea ice simulation, see Section 3. Thus, these atmospheric conditions are chosen for the forcing of the sea-ice model.

Ocean Forcing for FESIM

The FESIM requires ocean currents at least at the sea-ice ocean interface to determine the oceanic stress on the sea ice. Therefore, the Finite Element Sea-Ice Ocean Model (*Timmermann et al.*, in preparation) with the Arctic setup has been run for 18 years. Ocean velocities are averaged over the last 15 years to obtain a mean field. The mean ocean velocities have been used for ocean forcing in the FESIM set-up. Vertical diffusion is computed but the horizontal advection of the heat and salt flux in the ocean is neglected in FESIM.

2.2 Data Assimilation: Utilizing the SEIK Filter

There are different methods of estimating the state of a physical system using observations and a numerical model which is referred to as data assimilation. The assimilation of data and dynamics is a powerful methodology, which makes it possible to obtain efficient, accurate and realistic estimations which might not be otherwise feasible. A data assimilation system comprises of three components: a set of observations, a dynamical model and a data assimilation scheme. The central concept of data assimilation is the concept of errors, error estimation and error modeling. The numerical models have errors arising from various sources. Dynamical models are imperfect, with errors arising from the approximate physics, which govern the explicit evolution of the scale restricted state variable, and the discretization of continuum dynamics into a numerical model. Further, observational data have errors that for example arise from instruments used for measurements. Data assimilation schemes should take all these errors into consideration.

The specific uses of data assimilation include the control of errors for state estimates, the estimation of parameters, the explanation of real (ocean or atmosphere) dynamical processes, and monitoring and prediction. Consider state estimate with adequate data but a somewhat deficient dynamical model, assimilated data are able to compensate for the imperfect physics so as to provide estimates in agreement with the nature. This is possible if dynamical errors are treated adequately. For instance, if a model is considered perfect and real data is assimilated the state estimate will remain the model state characteristics. Even though assimilated estimates with deficient models are useful. It is of course important to attempt to correct model dynamics.

Here, the Singular Evolutive Interpolated Kalman (SEIK) Filter is utilized to assimilate satellite-derived sea-ice drift observations. The original Kalman Filter theory was derived first by *Kalman* (1960) for linear models and was extended to use nonlinear models with various filter types like the Extended Kalman Filter (EKF) (*Jazwinski*, 1970), the Ensemble Kalman Filter (EnKF) (*Evensen*, 1994b; *Burgers et al.*, 1998), and the SEIK Filter (*Pham et al.*, 1998b; *Pham*, 2001), which can be seen as a combination of EnKF and the Singular Evolutive Extended Kalman (SEEK) Filter (*Pham et al.*,

1998a). The SEIK Filter is considered to be robust and to give best assimilation performance with lowest computational cost which is essential for data assimilation in complex models because of its high demand on computing time (*Nerger et al.*, 2007).

2.2.1 Theoretical Formulation of the Kalman Filter Method

This section gives an overview of the sequential data assimilation methodology of Kalman Filters. First there is a brief description of statistical moments required for the method followed by the general formalism of the Kalman Filter.

Statistical Moments

The Kalman Filter method requires the first and second order statistical moments. The first order moment is the expectation $E(x)$ (mean, average, first moment) and for a continuous random variable x and its probability density function $p_x(x)$ it is defined by

$$E(x) = \int_{-\infty}^{\infty} x p_x(x) \mathrm{d}x. \tag{2.63}$$

In practice it is not feasible to compute the $p_x(x)$ explicitly due to the high complexity of a large-scale model system. Thus, one relies on the calculation of the moments through estimators. Therefore, in the ensemble Kalman Filter algorithm the first moment is approximated by the average $\overline{x}$ over the ensemble members $x^{(i)}$

$$\overline{x} = E(x) \approx \frac{1}{N} \sum_{i=1}^{N} x^{(i)}. \tag{2.64}$$

The second moment of x_k is given by

$$E(x_k^2) = \int ... \int x_k^2 p_{x_1,...,x_n}(x_1, ..., x_n) \mathrm{d}x_1 ... \mathrm{d}x_n \tag{2.65}$$

In the Kalman Filter algorithm the error covariance is required, which is defined for ϵ_k and ϵ_l by

$$\mathrm{cov}(\epsilon_k, \epsilon_l) = E\left(\left[x_k - E\left(x_k\right)\right]\left[x_l - E\left(x_l\right)\right]\right). \tag{2.66}$$

The error covariance describes the relation between two variables that in ensemble Kalman Filter algorithms are approximated by

$$\mathrm{cov}(\epsilon_k, \epsilon_l) \approx \frac{1}{N-1} \sum_{i=1}^{N} \left(x_k^{(i)} - \overline{x_k}\right)\left(x_l^{(i)} - \overline{x_l}\right). \tag{2.67}$$

The diagonal elements of the covariance matrix contain the variance of the model system, which corresponds to the squared standard deviation and results from

$$\mathrm{var}(\epsilon_k) = \mathrm{cov}(\epsilon_k, \epsilon_k) \approx \frac{1}{N-1} \sum_{i=1}^{N} \left(x_k^{(i)} - \overline{x_k}\right)^2 = \sigma_x^2 \ . \tag{2.68}$$

Higher order moments are not used by the Kalman Filter algorithm.

Introduction to the Kalman Filter Method

The Kalman Filter method is a sequential assimilation procedure, which combines the state estimate of a model with observations. Filtering is divided in two phases: prediction and update. In the forecast phase (prediction) the statistical moments are computed forward in time. When observations are available, the analysis phase (update) computes a new state estimate combining the forecast and the observation, and their error estimates. This cycle of forecast and analysis is repeated. The Kalman Filter theory requires unbiased, random error vectors with a Gaussian distribution function; a geophysical model can not fulfill these conditions completely which consequently influences the filter performance.

Computation of the updated state The updated (analyzed) state $\mathbf{x}_k^a$ at time k is derived from a linear, recursive form that contains the observation vector $\mathbf{y}_k^o$ and the state forecast vector $\mathbf{x}_k^f$

$$\mathbf{x}_k^a = \mathbf{A}_k \mathbf{y}_k^o + \mathbf{B}_k \mathbf{x}_k^f, \tag{2.69}$$

where $\mathbf{A}_k$ and $\mathbf{B}_k$ are time-varying weighting matrices, as yet unspecified. Here the observation vector is given by

$$\mathbf{y}_k^o = \mathbf{H}\hat{\mathbf{x}}_k + \epsilon_k^o, \tag{2.70}$$

where $\hat{\mathbf{x}}_k$ is the true state vector which is projected with the measurement operator $\mathbf{H}$ onto the observation location and ϵ_k^o is the observation error vector. The model state forecast $\mathbf{x}_k^f$ is obtained from a model operator $\mathbf{M}$, which might be nonlinear, describing the state propagation between two consecutive time steps. Then the forecasted model state $\mathbf{x}_k^f$ and its (symmetric) covariance matrix $\mathbf{P}_k^f$ are:

$$\begin{aligned}
\mathbf{x}_k^f &= \mathbf{M}\mathbf{x}_{k-1}^a && (2.71)\\
&= \hat{\mathbf{x}}_k + \epsilon_k^f, && (2.72)\\
\hat{\mathbf{x}}_k &= \mathbf{M}\hat{\mathbf{x}}_{k-1} + \epsilon_k^m, && (2.73)\\
\mathbf{P}_k^f &= E\left(\epsilon_k^f \epsilon_k^{f^{\mathrm{T}}}\right), && (2.74)\\
&= E[(\mathbf{x}_k^f - \hat{\mathbf{x}}_k)(\mathbf{x}_k^f - \hat{\mathbf{x}}_k)^{\mathrm{T}}], && (2.75)\\
&= E[(\mathbf{M}\mathbf{x}_{k-1}^a - \mathbf{M}\hat{\mathbf{x}}_{k-1})(\mathbf{M}\mathbf{x}_{k-1}^a - \mathbf{M}\hat{\mathbf{x}}_{k-1})^{\mathrm{T}}] + E[\epsilon_k^m \epsilon_k^{m^{\mathrm{T}}}], && (2.76)\\
\mathbf{P}_k^f &= \mathbf{M}\mathbf{P}_{k-1}^a\mathbf{M}^T + \mathbf{Q}. && (2.77)
\end{aligned}$$

$\mathbf{x}_{k-1}^a$ is the updated state of the previous assimilation step $k-1$ and $\mathbf{P}_{k-1}^a$ the corresponding updated covariance matrix; ϵ_k^f is the forecast error and $\mathbf{Q}$ is the estimated model error covariance matrix depending on the model error ϵ_k^m (*Pham*, 2001). To obtain the updated state $\mathbf{x}_k^a$ it is assumed that

$$\mathbf{x}_k^a = \hat{\mathbf{x}}_k + \epsilon_k^a, \tag{2.78}$$

where $E(\mathbf{x}_k^a) = E(\hat{\mathbf{x}}_k)$ and consequently

$$\begin{aligned} 0 = E(\epsilon_k^a) &= E(\mathbf{x}_k^a - \hat{\mathbf{x}}_k), && (2.79)\\ &= E(\mathbf{A}_k\mathbf{y}_k^o + \mathbf{B}_k\mathbf{x}_k^f - \hat{\mathbf{x}}_k), && (2.80)\\ &= E(\mathbf{A}_k\mathbf{H}\hat{\mathbf{x}}_k + \mathbf{A}_k\epsilon_k^o + \mathbf{B}_k\hat{\mathbf{x}}_k + \mathbf{B}_k\epsilon_k^f - \hat{\mathbf{x}}_k). && (2.81)\end{aligned}$$

If $E(\epsilon_k^f) = E(\epsilon_k^o) = 0$, ϵ_k^a is unbiased and it follows that

$$\begin{aligned} 0 = E(\epsilon_k^a) &= E((\mathbf{A}_k\mathbf{H} + \mathbf{B}_k - \mathbf{I})\,\hat{\mathbf{x}}_k) + E(\mathbf{A}_k\epsilon_k^o) + E(\mathbf{B}_k\epsilon_k^f), && (2.82)\\ 0 &= E((\mathbf{A}_k\mathbf{H} + \mathbf{B}_k - \mathbf{I})\,\hat{\mathbf{x}}_k), && (2.83)\\ 0 &= (\mathbf{A}_k\mathbf{H} + \mathbf{B}_k - \mathbf{I})\,, && (2.84)\\ \mathbf{B}_k &= \mathbf{I} - \mathbf{A}_k\mathbf{H}, && (2.85)\end{aligned}$$

where $\mathbf{I}$ is the identity matrix. Then the updated state is given by

$$\begin{aligned} \mathbf{x}_k^a &= \mathbf{A}_k\mathbf{y}_k^o + (\mathbf{I} - \mathbf{A}_k\mathbf{H})\,\mathbf{x}_k^f && (2.86)\\ &= \mathbf{A}_k\mathbf{y}_k^o + \mathbf{x}_k^f - \mathbf{A}_k\mathbf{H}\mathbf{x}_k^f && (2.87)\\ &= \mathbf{x}_k^f + \mathbf{A}_k\left(\mathbf{y}_k^o - \mathbf{H}\mathbf{x}_k^f\right). && (2.88)\end{aligned}$$

For a constant $\mathbf{A}_k$ this is equal to a simple restoring mechanism.

Derivation of the updated error covariance The analyzed error estimate is derived from the error estimations of the observation and state forecast, similar as for Equation (2.69) and with Equation (2.85) ϵ_k^a is estimated with

$$\begin{aligned} \epsilon_k^a &= \mathbf{A}_k\epsilon_k^o + \mathbf{B}_k\epsilon_k^f, && (2.89)\\ &= \mathbf{A}_k\epsilon_k^o + (\mathbf{I} - \mathbf{A}_k\mathbf{H})\,\epsilon_k^f. && (2.90)\end{aligned}$$

Then the updated error covariance estimation $\mathbf{P}_k^a$ is given by

$$\begin{aligned} \mathbf{P}_k^a &= E\left(\epsilon_k^a\epsilon_k^{a^{\mathrm{T}}}\right) && (2.91)\\ &= E\left(\left[(\mathbf{I} - \mathbf{A}_k\mathbf{H})\epsilon_k^f + \mathbf{A}_k\epsilon_k^o\right]\left[(\mathbf{I} - \mathbf{A}_k\mathbf{H})\epsilon_k^f + \mathbf{A}_k\epsilon_k^o\right]^{\mathrm{T}}\right) && (2.92)\\ &= E\Big((\mathbf{I} - \mathbf{A}_k\mathbf{H})\epsilon_k^f\epsilon_k^{f^{\mathrm{T}}}(\mathbf{I} - \mathbf{A}_k\mathbf{H})^{\mathrm{T}} + (\mathbf{I} - \mathbf{A}_k\mathbf{H})\epsilon_k^f\epsilon_k^{o^{\mathrm{T}}}\mathbf{A}_k^{\mathrm{T}} + && (2.93)\\ &\quad + \mathbf{A}_k\epsilon_k^o\epsilon_k^{f^{\mathrm{T}}}(\mathbf{I} - \mathbf{A}_k\mathbf{H})^{\mathrm{T}} + \mathbf{A}_k\epsilon_k^o\epsilon_k^{o^{\mathrm{T}}}\mathbf{A}_k^{\mathrm{T}}\Big).\end{aligned}$$

Assuming that the observation error ϵ_k^o is uncorrelated with the other error estimates, we have $E(\epsilon_k^f\epsilon_k^{o^{\mathrm{T}}}) = E(\epsilon_k^o\epsilon_k^{f^{\mathrm{T}}}) = 0$. Setting the error covariances $\mathbf{P}_k^f = E\left(\epsilon_k^f\epsilon_k^{f^{\mathrm{T}}}\right)$ and observation error matrix $\mathbf{R}_k = E\left(\epsilon_k^o\epsilon_k^{o^{\mathrm{T}}}\right)$ the updated error covariance matrix becomes

$$\begin{aligned} \mathbf{P}_k^a &= (\mathbf{I} - \mathbf{A}_k\mathbf{H})\,\mathbf{P}_k^f\,(\mathbf{I} - \mathbf{A}_k\mathbf{H})^{\mathrm{T}} + \mathbf{A}_k\mathbf{R}_k\mathbf{A}_k^{\mathrm{T}} && (2.94)\\ &= \mathbf{P}_k^f - \mathbf{A}_k\mathbf{H}\mathbf{P}_k^f - \mathbf{P}^f\mathbf{H}^{\mathrm{T}}\mathbf{A}_k^{\mathrm{T}} + \mathbf{A}_k\left(\mathbf{H}\mathbf{P}_k^f\mathbf{H}^{\mathrm{T}} + \mathbf{R}_k\right)\mathbf{A}_k^{\mathrm{T}}. && (2.95)\end{aligned}$$

To obtain the optimal choice of $\mathbf{A}_k$, the minimum of the sum of the diagonal elements of the error covariance matrix $\mathbf{P}_k^a$ has to be found. Therefore, the partial derivative of the trace with respect to $\mathbf{A}_k$ is set to zero.

$$\frac{\partial tr(\mathbf{P}_k^a)}{\partial \mathbf{A}_k} = 0. \tag{2.96}$$

The individual matrix derivatives are:

$$\begin{aligned}
\frac{\partial tr(\mathbf{P}_k^f)}{\partial \mathbf{A}_k} &= 0, & (2.97)\\
\frac{\partial tr(\mathbf{A}_k\mathbf{H}\mathbf{P}_k^f)}{\partial \mathbf{A}_k} &= \frac{\partial tr(\mathbf{I}\mathbf{A}_k\mathbf{H}\mathbf{P}_k^f)}{\partial \mathbf{A}_k} = \left(\mathbf{H}\mathbf{P}_k^f\right)^{\mathrm{T}}, & (2.98)\\
\frac{\partial tr(\mathbf{P}_k^f\mathbf{H}^{\mathrm{T}}\mathbf{A}_k^{\mathrm{T}})}{\partial \mathbf{A}_k} &= \frac{\partial tr((\mathbf{H}\mathbf{P}_k^f)^{\mathrm{T}}\mathbf{A}_k^{\mathrm{T}}\mathbf{I}^{\mathrm{T}})}{\partial \mathbf{A}_k} = \left(\mathbf{H}\mathbf{P}_k^f\right)^{\mathrm{T}}, & (2.99)\\
\frac{\partial tr(\mathbf{A}_k(\mathbf{H}\mathbf{P}_k^f\mathbf{H}^{\mathrm{T}}+\mathbf{R})\mathbf{A}_k^{\mathrm{T}})}{\partial \mathbf{A}_k} &= 2\mathbf{A}_k\left(\mathbf{H}\mathbf{P}_k^f\mathbf{H}^{\mathrm{T}}+\mathbf{R}\right). & (2.100)
\end{aligned}$$

Since $\mathbf{P}^f$ is symmetric, $\mathbf{P}^f = \mathbf{P}^{f^{\mathrm{T}}}$. From the Equations (2.96), (2.97), (2.98), (2.99) and (2.100) the matrix $\mathbf{A}_k$, usually denoted as the Kalman gain matrix $\mathbf{K}_k$, is found as

$$\mathbf{A}_k = \mathbf{K}_k = \mathbf{P}_k^f\mathbf{H}^{\mathrm{T}}[\mathbf{H}\mathbf{P}_k^f\mathbf{H}^{\mathrm{T}}+\mathbf{R}]^{-1}. \tag{2.101}$$

From the equations (2.88) and (2.101) the updated state and from equations (2.95) and (2.101) the posterior error covariance are given by

$$\begin{aligned}
\mathbf{x}_k^a &= \mathbf{x}_k^f + \mathbf{P}_k^f\mathbf{H}^{\mathrm{T}}[\mathbf{H}\mathbf{P}_k^f\mathbf{H}^{\mathrm{T}}+\mathbf{R}_k]^{-1}(\mathbf{y}_k^o - \mathbf{H}\mathbf{x}_k^f), & (2.102)\\
\mathbf{P}_k^a &= \mathbf{P}_k^f - \mathbf{P}_k^f\mathbf{H}^{\mathrm{T}}[\mathbf{H}\mathbf{P}_k^f\mathbf{H}^{\mathrm{T}}+\mathbf{R}]^{-1}\mathbf{H}\mathbf{P}_k^f & (2.103)\\
&= \mathbf{P}_k^f - \mathbf{K}_k\mathbf{H}\mathbf{P}_k^f. & (2.104)
\end{aligned}$$

2.2.2 The Singular Evolutive Interpolated Kalman (SEIK) Filter

The SEIK Filter is a modified Kalman filter which combines advantages of EnKF and SEEK. The forecast state and error estimation in the SEIK Filter are realized by a model ensemble integration, as in the EnKF, and the analysis is according to the efficient update algorithm of the SEEK Filter. The SEIK Filter algorithm is divided into four phases: initialization, forecast, analysis and re-initialization. The initialization occurs only before the first assimilation step. Figure 2.4 shows these phases and how SEIK, implemented in the Parallel Data Assimilation Framework (PDAF, *Nerger et al.* (2005b)), and FESIM interact.

Initialization The SEIK Filter uses a low rank representation of the covariance matrix so that the filter analysis operates only in a low dimensional subspace, which is defined by the number of model ensemble members. The rank r is the largest number of linearly

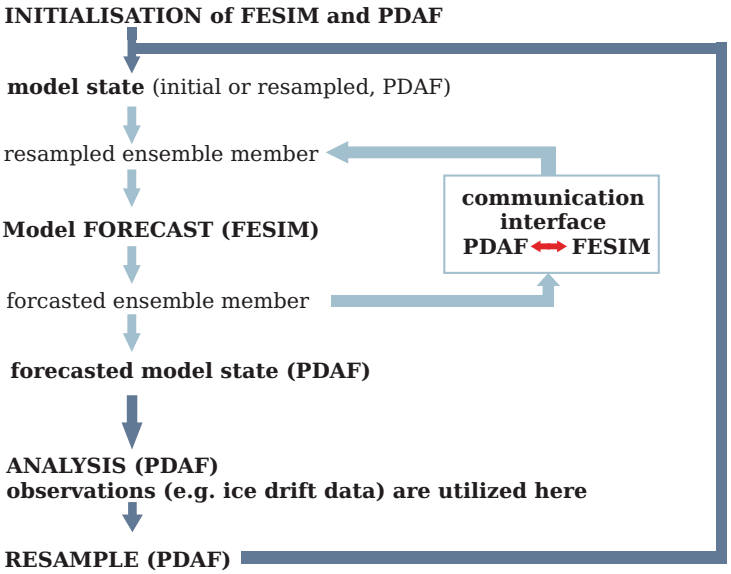

Figure 2.4: General data assimilation scheme: PDAF = Parallel Data Assimilation Framework (SEIK is implemented in PDAF, *Nerger et al.* (2005b)); FESIM = Finite Element Sea Ice Model. Inner loop (light blue): forecast of model ensemble to next observation time which is required for data assimilation; outer loop (blue): Analysis and re-initialization for next ensemble forecast. Communication interface realizes state information exchange between SEIK and FESIM.

independent row or column vectors of a matrix. The rank has to be sufficiently large such that the statistical model behavior is maintained. The determination of rank r is performed with a number of prior simulated model states $\mathbf{x}^{(i)}$, $i = 1, ..., k$ and their mean state $\overline{\mathbf{x}}$, which build the initial approximation of the total covariance matrix $\mathbf{P}$:

$$\mathbf{P} \approx \sum_{i=1}^{k} \frac{(\mathbf{x}^{(i)} - \overline{\mathbf{x}})(\mathbf{x}^{(i)} - \overline{\mathbf{x}})^{\mathrm{T}}}{k-1} = \mathbf{V}\mathbf{U}\mathbf{V}^{\mathrm{T}} \tag{2.105}$$

With a singular value decomposition the singular values, which are held in the diagonal matrix $\mathbf{U}$, and eigenvectors $\mathbf{V}$ can be determined. The sum of the singular values corresponds to 100 % coverage of model statistics. So the rank can be reduced to 99 or 90 %. Then the initial rank-reduced covariance matrix $\mathbf{P}_0^a$ is approximated with r largest singular values and corresponding eigenvectors.

With the mean state $\overline{\mathbf{x}} \equiv \overline{\mathbf{x}_0^a}$ and the initial rank-reduced covariance matrix $\mathbf{P}_0^a$ in the decomposed form the ensemble $\mathbf{x}_0^{a(l)}$, $l = 1, ..., r+1$ of minimum size is generated by Equation (2.107). The covariance matrix in a decomposed form is

$$\mathbf{P}_0^a = \mathbf{V}_0 \mathbf{C}_0^T \mathbf{\Omega}_0^T \mathbf{\Omega}_0 \mathbf{C}_0 \mathbf{V}_0^T, \tag{2.106}$$

where $\mathbf{C}_0$ contains in its diagonal elements the square root of the eigenvalues of $\mathbf{P}_0^a$, and $\mathbf{\Omega}_0$ is a $(r+1) \times r$ random matrix with orthogonal columns. $\mathbf{V}_0$ contains in its columns

the corresponding eigenvectors of $\mathbf{P}_0^a$. The ensemble states are then given by

$$\mathbf{x}_0^{a(l)} = \overline{\mathbf{x}_0^a} + \sqrt{r+1}\mathbf{V}_0\mathbf{C}_0^T\mathbf{\Omega}_{0,l}^T, \tag{2.107}$$

where $\mathbf{\Omega}_{0,l}^T$ denotes the l-th column.

Forecast Each ensemble member is forecasted with the nonlinear model. The model operator $\mathbf{M}$ symbolizes the nonlinear integration of the applied model to determine the model forecast:

$$\mathbf{x}_k^{f(l)} = \mathbf{M}\mathbf{x}_{k-1}^{a(l)}. \tag{2.108}$$

The formulation of the SEIK Filter is based on an efficient description of $\mathbf{P}_k^f$, in terms of the ensemble states, which are denoted as:

$$\mathbf{X}_k^f = [\mathbf{x}_k^{f(1)}, ..., \mathbf{x}_k^{f(r+1)}]. \tag{2.109}$$

Furthermore a $(r+1) \times r$ matrix $\mathbf{T}$ with zero column sums is introduced as

$$\mathbf{T} = \begin{pmatrix} \mathbf{I_{r\times r}} \\ \mathbf{0}_{1\times r} \end{pmatrix} - \frac{1}{r+1}\left(\mathbf{1}_{(r+1)\times r}\right), \tag{2.110}$$

so that $\mathbf{X}_k^f\mathbf{T}$ contains the residuals of the ensemble mean. An efficient description of $\mathbf{P}_k^f$ is obtained with

$$\mathbf{P}_k^f = \frac{1}{1+r}\mathbf{X}_k^f\mathbf{T}\left(\mathbf{T}^T\mathbf{T}\right)^{-1}\mathbf{T}^T\left(\mathbf{X}_k^f\right)^T \tag{2.111}$$

so that the matrix $\mathbf{T}$ fulfills the purpose of implicitly subtracting the ensemble mean when computing $\mathbf{P}_k^f$. Additionally $\mathbf{L}_k$ and $\mathbf{G}$ are defined as follows

$$\mathbf{L}_k := \mathbf{X}_k^f\mathbf{T}, \tag{2.112}$$

$$\mathbf{G} := \frac{1}{r+1}\left(\mathbf{T}^T\mathbf{T}\right)^{-1}. \tag{2.113}$$

$\mathbf{L}_k$ is the matrix with columns $\overline{\mathbf{x}_k^f} - \mathbf{x}_k^{f(1)}, ..., \overline{\mathbf{x}_k^f} - \mathbf{x}_k^{f(r)}$. For the covariance matrix then follows

$$\mathbf{P}_k^f = \mathbf{L}_k\mathbf{G}\mathbf{L}_k^T. \tag{2.114}$$

Analysis The correction or increment for the analysis update is computed as a weighted average over vectors of the error subspace. The corrections made by the analysis are indirect and in those directions in which the error is amplified or the error was not decreased sufficiently by the system (*Pham*, 2001). Additionally, cross correlations lead to an update of the total state. That means, if observations of only one physical variable, as ice velocities, are supplied to the filter algorithm, also the other model fields in the state vector are modified by the analysis.

The full model error covariance matrix $\mathbf{Q}_k$ is projected onto the error subspace in the SEIK algorithm:

$$\check{\mathbf{Q}}_k = \left(\mathbf{L}_k^T\mathbf{L}_k\right)^{-1}\mathbf{L}_k^T\mathbf{Q}_k\mathbf{L}_k\left(\mathbf{L}_k^T\mathbf{L}_k\right)^{-1}. \tag{2.115}$$

Here, matrix $\mathbf{L}_k$ contains the forecasted residuals of the ensemble mean, similar to Equation (2.112). The analysis equations are defined as

$$\mathbf{U}_k^{-1} = [\mathbf{G} + \check{\mathbf{Q}}_k]^{-1} + (\mathbf{H}\mathbf{L}_k)^T \mathbf{R}^{-1}\mathbf{H}\mathbf{L}_k, \tag{2.116}$$

$$\mathbf{x}_k^a = \overline{\mathbf{x}_k^f} + \mathbf{K}_k \left(\mathbf{y}_k^o - \mathbf{H}\overline{\mathbf{x}_k^f}\right), \tag{2.117}$$

$$\mathbf{K}_k = \mathbf{L}_k\mathbf{U}_k\mathbf{L}_k^T\mathbf{H}^T\mathbf{R}_k^{-1}, \tag{2.118}$$

which are analog to the SEEK algorithm. The weights are defined by

$$\mathbf{U}_k\mathbf{L}^T\mathbf{H}^T\mathbf{R}_k^{-1}\left(\mathbf{y}_k^o - \mathbf{H}\overline{\mathbf{x}_k^f}\right). \tag{2.119}$$

The analysis covariance matrix is implicitly given by $\mathbf{P}_k^a := \mathbf{L}_k\mathbf{U}_k\mathbf{L}_k^T$.

Re-Initialization As already mentioned above the analysis does not deliver a simple ensemble correction for the observed model state, e.g. velocities, but an update of the entire mean model state and the covariance matrix. From the updated statistics a new ensemble is generated similar to the initialization and a Cholesky decomposition is utilized to obtain $\mathbf{U}_k^{-1} = \mathbf{C}_k\mathbf{C}_k^T$. Then similar to the initialization, the covariance matrix is written as:

$$\mathbf{P}_k^a = \mathbf{L}_k\left(\mathbf{C}_k^{-1}\right)^T\mathbf{\Omega}_k^T\mathbf{\Omega}_k\mathbf{C}_k^{-1}\mathbf{L}_k^T, \tag{2.120}$$

which is not explicitly computed in the SEIK algorithm. Accordingly the reinitialized ensemble state is given as

$$\mathbf{x}_k^{a(l)} = \overline{\mathbf{x}_k^a} + \sqrt{r+1}\mathbf{L}_k\left(\mathbf{C}_k^{-1}\right)^T\mathbf{\Omega}_{k,l}^T. \tag{2.121}$$

This new ensemble represents the updated statistics with the mean $\overline{\mathbf{x}_k^a}$ and the covariance matrix $\mathbf{P}_k^a$.

Modifications to Original SEIK Setup *Pham* (2001) suggests to use a forgetting factor to enhance filter stability which is referred to be the most vexing problem in nonlinear data assimilation. The forgetting factor is able to prevent "filter excursions" and is able to maintain a robust rms error approximation of the model state. Here, the convenient value of 0.8 is chosen for sea-ice drift data assimilation. Additionally the model error covariance matrix $\mathbf{Q}_k$ is not employed. Then Equation (2.116) becomes

$$\mathbf{U}_k^{-1} = \rho\mathbf{G}^{-1} + (\mathbf{H}\mathbf{L}_k)^T\mathbf{R}_k^{-1}\mathbf{H}\mathbf{L}_k \tag{2.122}$$

where ρ is the forgetting factor and leads to an inflation of the estimated variances of the model state.

A common problem in Kalman-type filters that may also arise in the SEIK Filter is that the randomly drawn ensemble member is not a physical realizable state (*Pham*, 2001). If this occurs the sea-ice model might collapse so that the unrealistic states have to be replaced with a nearby realizable state before the next model forecast.

2.2.3 SEIK Filter with Local Analysis Update

Another SEIK Filter derivative is used for sea-ice drift assimilation. The Local SEIK (LSEIK) Filter is based on the same equations as the original SEIK Filter presented in the previous section. Here, the model area is split into smaller domains. The analysis is done by a sequence of local updates in these sub-domains. To update the full model domain, the local analysis and re-initialization is done also as a sequence of independent local updates on each of the local domains (*Nerger et al.*, 2006).

Mitchell et al. (2002) point out that the neglect of remote observations together with the independent local analysis can lead to an imbalance in the ensemble states. Further, this may lead to discontinuities in the ensemble states. The localized analysis is often preferred relative to a global analysis because the noise of the long-range covariances will be rather large compared to existing long-range covariances, which are mostly small. Thus, the information of the long-range covariance can be neglected (*Houtekamer and Mitchell*, 1998). The noise can even result in spurious correlations which can deteriorate the state estimate (*Nerger et al.*, 2005a).

Two simple localizations are realized. First the sea-ice state at each surface node of the model grid is updated sequentially. The other localization comprises the sea-ice and ocean state at each surface node and the water column beneath, which is also updated sequentially in the analysis phase. Sea-ice drift observations within an influence radius of 150 km to the current node are considered for the local analysis.

2.3 Observations

Generally, sea-ice observations are sparsely distributed in space and time. This fact especially concerns in situ observations due to poor accessibility of polar regions. Therefore, satellite missions monitoring the polar regions represent a great advancement for large-scale (spatial) and continuous (temporal) sea-ice observations. At present, the sea-ice concentration and sea-ice drift can reliably be observed with satellites. The sea-ice thickness, which is representative for sea-ice volume, so far can not be observed satisfactorily on large scales. Sea-ice thickness measurements exists only on regional or local scales; widely scattered spatially and temporally and can hardly form a coherent data set.

With the help of satellite-derived sea-ice drift, which is applied for data assimilation, it is hoped to improve the sea-ice thickness distribution in the Arctic Basin. Therefore sea-ice thickness data from a submarine cruise in 2000 and the GreenIce campaign in 2004 are taken to validate sea-ice drift assimilation effects on sea-ice thickness. Validation of assimilated sea-ice drift can also be done with position data from drifting buoys which are independent from satellite derived sea-ice drift. This section describes the data which are employed for data assimilation and validation of assimilation results.

2.3.1 Sea-Ice Drift Fields Derived from Satellite Observations

All techniques deriving sea-ice drift from satellite measurements so far can only detect the displacements of features that are large compared to the pixel resolution. For the Special Sensor Microwave Imager (SSM/I) satellite the tracking of single floes is not possible but the Synthetic Aperture Radar (SAR) Satellite is able to track single floes. Buoy drift measurements feature winter drift speeds of less than 0.3 $\mathrm{m\,s^{-1}}$ with a large number of observations of even less than 0.01 $\mathrm{m\,s^{-1}}$ (*Lemke et al.*, 1997). Such a slow drift is hard to detect with SSM/I data, which have a resolution of 12.5 km and requires a time difference of approximately 14 days, so that the feature identification does not lead to useful results (*Martin and Augstein*, 2000). So the satellite-derived drift does not satisfactorily represent very slow drifts. This is also true for very fast sea-ice drift because the features can change significantly within a shorter period and can thus not be tracked. This especially occurs at the ice edge and export areas, where the sea-ice concentration is small and the sea-ice movement is strongly correlated with the wind, when strong atmospheric events occur, which support fast drifting sea ice. The derived sea-ice drift is representative for the mean velocity over a predefined time period and on large scale and not for single floes like buoy observations are. The satellite data are also restricted due to snow and sea-ice conditions (melt ponds, wet snow) which leads to a good data coverage only for winter months (early October to end of April) due to the cold atmosphere. Even those datasets have missing or corrupted data on single pixels or even for entire data sets for particular time periods (*Ezraty and Piollé*, 2004a). However, these data provide sea-ice drift fields with a large spatial and temporal coverage and are suitable for data assimilation with a large scale sea-ice model like FESIM.

SSM/I and Quikscat Derived Drift Maps

In recent years sea-ice motion over polar oceans has been estimated from microwave brightness temperature data obtained from space borne radiometers like the SSM/I. Additionally, there are satellite data from active sensors like the Quick Scatterometer (Quikscat). These data sets have been merged to increase density of drift estimates over entire polar region (*Ezraty and Piollé*, 2004a). The merged sea-ice drift datasets are provided by the French Processing and Archiving Facility CERSAT[5] and are used for sea-ice drift data assimilation. The data used in the experiments are provided as 3 day mean sea-ice drift data mapped on the National Snow and Ice Data Center[6] (NSIDC) grid that has an almost constant grid cell size of 12.5 km $\times$ 12.5 km but the ice motion is estimated every 5 pixels in both directions. Thus, the actual resolution of provided drift observations is 62.5 km $\times$ 62.5 km

The backbone of the merged map is built from drift grid nodes where triplets (two drift estimates from SSM/I of the horizontally and vertically polarized channels at 85 GHz and one drift estimate from Quikscat) and pairs of identical vectors are found. A single drift vector at a certain grid node has to be validated by comparison to the

[5]URL: *http://www.ifremer.fr/cersat/en/index.htm*
[6]URL: *http://nsidc.org/data/*

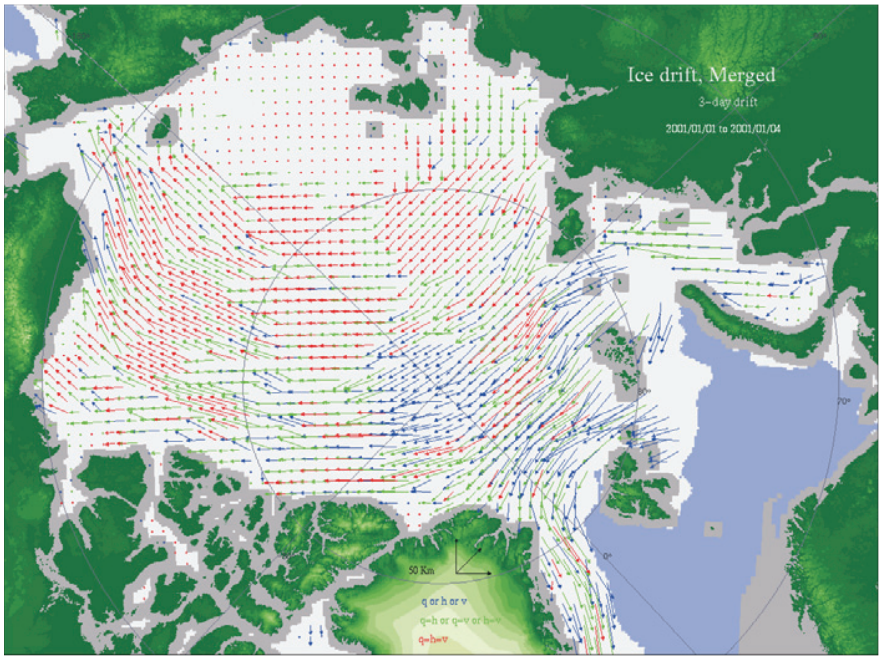

Figure 2.5: Merged Quikscat and SSM/I 3 day mean drift map provided by CERSAT. Different colors of drift arrows are due to different coincidences of signals from the different channels of SSM/I and Quikscat.

surrounding drift vectors. The merged drift product relies on the local consistency of the drift vector field, therefore a typical coherence area of 250 km × 250 km was taken. More detailed data processing procedures can be found in the user's manuals (*Ezraty and Piollé*, 2004a,b; *Ezraty et al.*, 2004).

Figure 2.5 shows a 3 day mean drift map derived from these satellite data. The different colors of the arrows represent differently validated coincident drift vectors: red drift vectors indicate where all three drift estimates of SSM/I and Quikscat result in the same drift (triplets), green are drift vectors where two of three have identical drift vectors (pairs), and blue are validated single drift vector solutions.

Error Estimation

For data assimilation an estimate of the observation errors is required, see Section 2.2. In *Ezraty and Piollé* (2001) the estimate of the technical error due to pixel-size and grid setup is suggested as follows: The position uncertainty is derived from the nominal pixel size of the NSIDC grid which is 12.5 km × 12.5 km. The probability that the tip of a drift vector is located in pixel $P(i, j)$ is 1. The zonal and meridional sizes of this rectangular pixel are $\delta_x = \delta_y = 12.5$ km. For an arbitrary element within this pixel the

probability density function is:

$$p = \frac{1}{\delta_x \delta_y}. \tag{2.123}$$

The variance for the displacement in zonal σ_x^2 or meridional σ_y^2 direction within the pixel is estimated as:

$$\sigma_x^2 = \iint\limits_S p x^2 \mathrm{d}x\mathrm{d}y = p \int x^2 \mathrm{d}x \int \mathrm{d}y = \frac{1}{\delta_x \delta_y} \frac{1}{3} x^3 \mid_{-\frac{\delta_x}{2}}^{\frac{\delta_x}{2}} y \mid_{-\frac{\delta_y}{2}}^{\frac{\delta_y}{2}} = \frac{\delta_x^2}{12}, \tag{2.124}$$

$$\sigma_x = \frac{\delta_x}{\sqrt{12}}. \tag{2.125}$$

with the pixel surface $S = \delta_x \delta_y$. The variance of the y component is similarly given by

$$\sigma_y^2 = \iint\limits_S p y^2 \mathrm{d}x\mathrm{d}y = p \int \mathrm{d}x \int y^2 \mathrm{d}y = \frac{\delta_y^2}{12}. \tag{2.126}$$

The variances for the velocity and its zonal and meridional component, with time step $\Delta t = \mid t_1 - t_2 \mid$, are:

$$\sigma_{v_x}^2 = \frac{\sigma_x^2}{\Delta t^2}, \tag{2.127}$$

$$\sigma_{v_y}^2 = \frac{\sigma_y^2}{\Delta t^2}. \tag{2.128}$$

As mentioned before, there is an additional uncertainty due to grid set up, which means that the actual pixel size depends on latitude. The largest deviation from the nominal pixel size is defined with 0.493 km at 60° N for one pixel (*Ezraty and Piollé*, 2004b). Therefore the single uncertainties are:

$$\sigma_x = \sqrt{\sigma_x^2} + \frac{0.493}{12.5} \mid x \mid, \tag{2.129}$$

$$\sigma_y = \sqrt{\sigma_y^2} + \frac{0.493}{12.5} \mid y \mid, \tag{2.130}$$

$$\sigma_{v_x} = \sqrt{\sigma_{v_x}^2} + \frac{0.493}{12.5} \left| \frac{y}{\Delta t} \right|, \tag{2.131}$$

$$\sigma_{v_y} = \sqrt{\sigma_{v_y}^2} + \frac{0.493}{12.5} \left| \frac{y}{\Delta t} \right|. \tag{2.132}$$

The typical drift observation error amounts to approximately 1.4 to 1.6 $\mathrm{cm\,s^{-1}}$.

2.3.2 Buoy Data from the International Arctic Buoy Programme

The International Arctic Buoy Programme (IABP)[7] maintains a network of drifting buoys since 1991 (former Arctic Ocean Buoy Program established in 1978) to provide

[7] Annual reports on this program were published from 1979 through the present.
URL: *http://iabp.apl.washington.edu/*

Figure 2.6: Buoy trajectories of the year 2000 in the Arctic; picture provided by AWI Buoy Arctic and Antarctic Archive with current URL: *http://zzz.awi-bremerhaven.de:8002/servlet/Init.*

meteorological and oceanographic data (*Ortmeyer and Rigor*, 2004). This data set contains 12 hourly interpolated pressure, temperature, position and sea-ice drift data available from 1979. The buoy locating often results in positions with a measurement error less than 300 m (*Ortmeyer and Rigor*, 2004). Global Positioning Systems (GPS) have been installed on many of the newer buoys, so that their position is detected within 100 m. Figure 2.6 shows a map of drift trajectories of selected buoys from the year 2000.

Determine Drift Velocity Using Buoy Positions

The buoy position data are used as an additional independent sea-ice drift data set besides the satellite derived ice drift data. Here, they are applied to validate assimilated ice drift.

Two buoy positions at time t_1 and t_2 are required to determine ice drift. It is assumed that a buoy covers the shortest distance between 2 positions within a predefined time period. These two locations and the north pole build a spherical rectangular triangle (Figure 2.7). Point A and C are the two buoy positions with latitudes φ_A and φ_C and longitudes λ_A and λ_C. Point B corresponds to the north pole.

Determining the distance between A and C spherical trigonometry is used. The min-

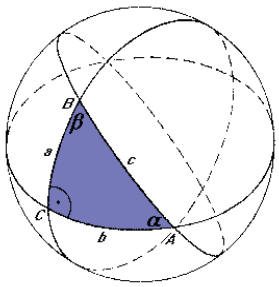

Figure 2.7: A spherical rectangular triangle.

imum drift d between A and C is defined as:

$$\cos d = \cos(90 - \varphi_A)\cos(90 - \varphi_C) + \sin(90 - \varphi_A)\sin(90 - \varphi_C)\cos(\lambda_C - \lambda_A), \quad (2.133)$$

$$d = \frac{\pi R_\mathrm{E}}{180^\circ}\arccos(\cos d). \quad (2.134)$$

The displacement in y or meridional direction is

$$y = \frac{\pi R_\mathrm{E}}{180}(\varphi_C - \varphi_A), \quad (2.135)$$

because the latitudes are equidistant. One degree corresponds to $\frac{\pi R_\mathrm{E}}{180}$ with Earth's radius $R_\mathrm{E} = 6\,371,110\,\mathrm{km}$. For the longitude, the distance varies with changing latitude. But the drift distance d, displacement along latitude and longitude or x and y respectively, build a spherical rectangular triangle too, because x and y are perpendicular. The displacement in x or zonal direction is then:

$$x = \frac{\pi R_\mathrm{E}}{180}\arccos\left(\frac{\cos d}{\cos(\varphi_C - \varphi_A)}\right). \quad (2.136)$$

The minimum, averaged drift velocity v is from time t_1 to t_2:

$$v = \frac{d}{\Delta t} = \frac{\pi R_\mathrm{E}}{180} \cdot \frac{\arccos(\sin\varphi_A \sin\varphi_C + \cos\varphi_A \cos\varphi_C \cos(\lambda_C - \lambda_A))}{\mid t_2 - t_1 \mid}. \quad (2.137)$$

The velocity components in zonal and meridional direction are

$$v_x = \frac{x}{\Delta t} \qquad \text{and} \qquad v_y = \frac{y}{\Delta t}. \quad (2.138)$$

Drift Velocity Uncertainty due to Position Error

Buoy position data have a maximum uncertainty of 300 m (*Ortmeyer and Rigor*, 2004). Therefore it is assumed that the origin as well as the end of a displacement vector is located in a circle with a radius of $R = 300\,\mathrm{m}$. The centers of these two error circles are

the buoy position at time t_1 and t_2. It is also assumed to have a uniform probability distribution of the location within a circle. Then the probability density function for the position of the origin or end of the vector is:

$$p_p = \frac{1}{\pi R^2}. \tag{2.139}$$

For determining the buoy drift two points are necessary. Therefore the variance σ^2 of zonal displacement is:

$$\sigma_x^2 = p_p \iint x^2 \mathrm{d}x\mathrm{d}y + p_p \iint x^2 \mathrm{d}x\mathrm{d}y = 2p_p \iint x^2 \mathrm{d}x\mathrm{d}y. \tag{2.140}$$

This is also true for the meridional displacement. The surface integral is encompassed by the circle. Therefore a practical substitution into polar coordinates is done:

$$x = \quad r\cos\alpha \qquad y = r\sin\alpha \tag{2.141}$$

$$\mathrm{d}x = \quad \mathrm{d}r\ \cos\alpha \qquad \mathrm{d}y = \mathrm{d}\alpha\, r\cos\alpha \tag{2.142}$$

$$\mathrm{d}x = \quad -\mathrm{d}\alpha\, r\sin\alpha \quad \mathrm{d}y = \mathrm{d}r\ \sin\alpha. \tag{2.143}$$

Then Equation (2.140) together with Equations (2.141) and (2.142) turns into

$$\sigma_x^2 = 2p_p \iint r^3 \cos^4\alpha\, \mathrm{d}r\mathrm{d}\alpha = 2p_p \int_0^R r^3 \left[\int_0^{2\pi} \cos^4\alpha\, \mathrm{d}\alpha\right] \mathrm{d}r \tag{2.144}$$

$$= \frac{2}{\pi R^2}\frac{r^4}{4}\bigg|_0^R \left[\frac{3\alpha}{8} + \frac{1}{2}\sin 2\alpha + \frac{1}{32}\sin 4\alpha\right]_0^{2\pi} = \frac{3}{8}R^2. \tag{2.145}$$

Similarly, but substituting Equations (2.141) and (2.143) the variance for the meridional displacement is determined as:

$$\sigma_y^2 = 2p_p \left| \iint -r^3 \sin^4\alpha\, \mathrm{d}r\mathrm{d}\alpha \right| = 2p_p \left| -\int_0^R r^3 \left[\int_0^{2\pi} \sin^4\alpha\, \mathrm{d}\alpha\right] \mathrm{d}r \right| \tag{2.146}$$

$$= \frac{2}{\pi R^2}\frac{r^4}{4}\bigg|_0^R \left[\frac{3\alpha}{8} + \frac{1}{2}\sin 2\alpha + \frac{1}{32}\sin 4\alpha\right]_0^{2\pi} = \frac{3}{8}R^2. \tag{2.147}$$

The total displacement error is approximately 367 m. The variance of the velocity components are:

$$\sigma_{v_x}^2 = \sigma_{v_y}^2 = \frac{3}{8}\frac{R^2}{\Delta t^2}. \tag{2.148}$$

For comparisons with assimilation drift results a time period of 3 days is required. The drift and velocity determination and their error approximation should take into consideration that fact. For that, the 12 hourly buoy-drift observations are averaged over the relevant time period and an additional position error depending on the number of available data sets within that time period is used. Then the drift error is approximately 2.2 km for three days which corresponds to a velocity error of less than 1 $\mathrm{cm\,s^{-1}}$.

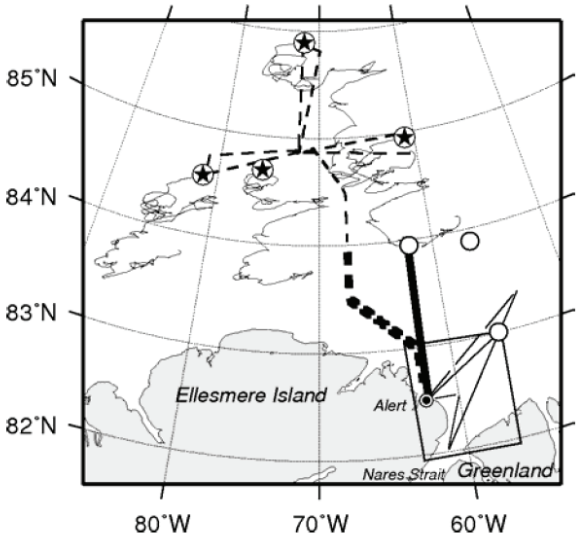

Figure 2.8: Map of HEM sample location of GreenIce campaign 2004 and 2005, from *Haas et al.* (2006): the region north of Ellesmere Island, Canada, and Nares Strait; the dashed line shows the flight track where profiles were measured in May 2004, the solid line shows the track of May 2005, the thin lines represent buoy trajectories between May 2004 and 2005.

2.3.3 Sea-Ice Thickness Derived from HEM Measurements

Helicopter borne electromagnetic (HEM) measurements of total (sea ice plus snow) sea ice thickness have been performed since 2001. In the central Arctic a relatively large area - for this type of observation - was sampled during the GreenIce campaign in 2004. The flight tracks (dashed lines) can be seen in Figure 2.8. This campaign was performed on May 12 and 13, 2004. A 400 km long meridional profile was obtained between Alert (Ellesmere Island, Canada) and 86°N. At 85°N, 72°W an ice camp for refueling the helicopter was established. From this point four east-west flights more than 100 km long were conducted (*Haas et al.*, 2006).

The HEM components are sensitive to the sensor height above the conductive sea water surface, which corresponds to the distance to the lower surface of the sea ice. The system also contains a laser altimeter which determines the distance to the sea ice or open ocean surface. So the difference of altitude (from laser altimeter) and sea-ice bottom surface (derived from EM measurements) results in the total sea-ice thickness. Detailed data processing procedures can be found in *Haas* (1998) and *Haas et al.* (2006).

Comparisons with drill-hole sea-ice thickness data show an agreement within ±0.1 m over level sea ice (*Haas et al.*, 2006). The accuracy over sea-ice pressure ridges[8] is worse due to the "footprint" of the em field and porous nature of ridge keels. The maximum ridge thickness could be underestimated by as much as 50 % in worst cases (*Haas and*

[8]Sea-ice pressure ridges are deformed sea-ice due to dynamic processes and separates into a sail above the water level and a keel below and they vary in porosity, extent and volume.

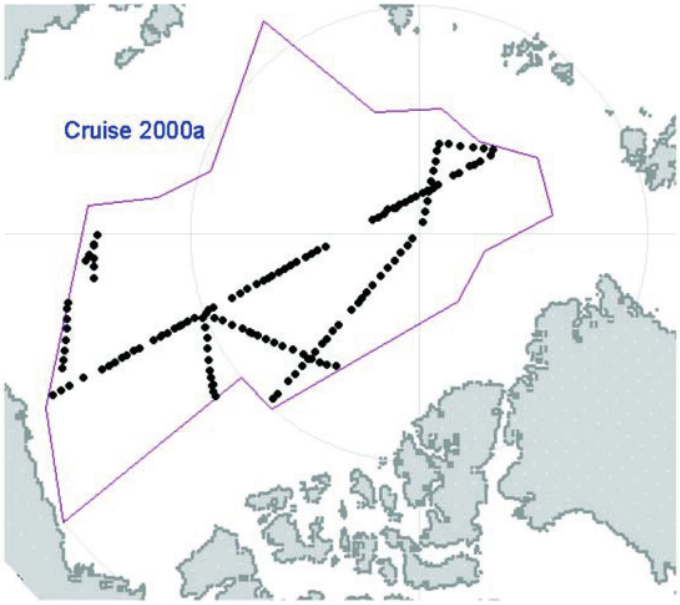

Figure 2.9: Map of ULS sample location of the submarine cruise in October 2000; the line marks the border of the Exclusive Economic Zones of the adjacent countries, the black dots mark the single samples taken during the cruise (*NSIDC*, 1998, updated 2006).

Jochmann, 2003). Consequently the mean sea-ice thickness is underestimated in these data because the thickness of ridges are generally underestimated by em data.

The observed sea-ice area is dominated by multi-year sea ice with a modal sea-ice thickness of 3.9 m and a mean sea-ice thickness of 4.67 m. The meridional track, from Alert up to 86 °N, was broken up in smaller segments of 0.5° where a slightly decrease of modal sea-ice thickness was observed. The standard sea-ice thickness deviation does not represent the observational error but shows the variability of sea-ice thickness along the regarded track (*Haas et al.*, 2006).

2.3.4 Sea-Ice Thickness Derived from Submarine ULS Measurements

Measurements of Arctic sea-ice drafts have been taken by US Navy submarines for some decades. These submarines are equipped with an upward looking sonar (ULS) that continually measures the distance to the sea-ice bottom while a pressure sensor provides the distance to the sea surface (*Rothrock et al.*, 2003). Sea-ice draft is then defined by the difference between these distances. The ice draft is calculated from the total travel time of the pulse from the sonar, to the overlying ice or ocean surface and back, and from the depth of the sensor given by the pressure using an assumed sound speed. The resulting recorded profiles have different sampling lengths depending on the track. The data were processed by the Polar Science Center at the University of Washington and

were derived by digitizing analog paper charts. The digitizing procedures for these data can be found in *Wensnahan and Rothrock* (2005).

The US Navy released these data which are available from the National Snow and Ice Data Center (*NSIDC*, 1998, updated 2006). These data are all located outside the Exclusive Economic Zones in the central Arctic, which is shown by the line in Figure 2.9. The position information is accurate to within $1/12^\circ$ which corresponds to an accuracy of approximately 5.6 km, which is less than the FESIM grid resolution, and the date is given within a 10 day leg (*Wensnahan*, 2006).

The lengths of the observed sea-ice draft profiles range widely from a few to hundreds of kilometers. The variations of submarine's travel properties are restricted to ±2 knots and 34 % in speed, 50 ft in depth which corresponds to 15.24 m, and a few degrees in course. In addition to the sea-ice draft files, sea-ice statistics are provided for each profile regardless of sampling length. They contain a histogram of the profile drafts plus the mean, standard deviation, and the mode of the drafts. All statistics use the entire draft profile including open water.

The submarine cruise of the year 2000 has been chosen for comparison with model simulation and assimilation results. For this year merged SSM/I and Quikscat data are available for data assimilation. Currently, this is the most recent data set provided by *NSIDC* (1998, updated 2006).

The sea-ice draft has to be corrected to sea-ice thickness for comparisons with the modeled sea-ice thickness. The simple relation neglecting a possible snow cover

$$h_{\text{ice}} = d * \frac{\rho_{\text{water}}}{\rho_{\text{ice}}} \tag{2.149}$$

is used to compute ice thickness h_{ice} from draft d.

2.3.5 Sea-Ice Concentration Maps derived from SSM/I Satellite Data

The Special Sensor Microwave Imager (SSM/I) satellite provides brightness temperature which has been widely and regularly used since 1987 to estimate sea-ice extent and sea-ice concentration. The microwave radiometer measures the thermal emission at the Earth surface and various effects of the transfer through the atmosphere at frequencies of 19.35, 22.23, 37.0 and 85.5 GHz. These data are provided daily and the NSIDC distributes them through its web site (*http://nsidc.org*). Sea-ice concentration data for validation of data assimilation results where taken from the CERSAT data base[9]. These data where derived from the 85 GHz brightness temperature maps processed with the Artist Sea Ice algorithm (*Kaleschke et al.*, 2001; *Kaleschke*, 2003). The sea-ice concentration data is mapped over the NSIDC 12.5 km × 12.5 km grid. A rough approximation of a general observational error is about 5 to 10 % of sea-ice concentration depending on the season and polar regions (*Kaleschke*, 2003; *Comiso et al.*, 1997).

[9]Sea-ice concentration data are available from ftp-server:
ftp://ftp.ifremer/ifremer/cersat/products/gridded/psi-concentration

3 Sea-Ice Model Reference Simulation

The results of long-term modeled sea-ice concentration, drift and thickness are presented in this section. Also a comparison with satellite-derived sea-ice concentration and drift data is given. Here, monthly means are analyzed and compared. Comparisons to assimilation results in Chapter 4 are shown with a dataset of three-day means which corresponds to the assimilation interval.

3.1 Sea-Ice Concentration and Extent

The seasonal cycle of sea-ice cover is reproduced realistically by the model (Figure 3.1). In winter a sea-ice concentration of 90 - 100 % is prevalent in the Central Arctic. Sea-ice concentrations below 80 % occur at the ice edge which is sharply defined by the oceanic and atmospheric conditions. The marginal ice zone in the Greenland and Barents Sea is overestimated by the model simulation compared to the climatological mean of observed sea-ice concentration in winter (Figure 3.2). In summer the sea-ice concentration reduces especially in the Siberian Seas (Figure 3.1) but in the Beaufort Sea not as much as observed (Figure 3.2).

A comparison with monthly mean satellite derived sea-ice concentration data from 1992 - 2005 provided by CERSAT reveals that the modeled winter sea-ice concentration agrees very well with the observation. In contrast, the summer sea-ice concentration is over- or underestimated in some areas (Figure 3.3). The sea-ice cover of the central Arctic (latitude $> 81^\circ$ N) is simulated very well in winter but the summer sea-ice concentration is underestimated because the simulated mean concentration is below 70 % in that region (Figure 3.1). This feature does not appear in the observations, which indicate that the sea-ice concentration exceeds 90 %. In Winter the Beaufort Sea is covered with sea ice, which is simulated as observed. In Contrast to the Central Arctic the sea-ice cover is overestimated in the Beaufort Sea in summer. Here, the model maintains a high sea-ice concentration which is supported by thick sea ice in that region (Figure 3.13). The sea-ice model simulates a realistic sea-ice cover in the Siberian Seas in winter as well. These seas exhibit a strong variability in summer. Here, the scatter is wide between simulation and observation (Figure 3.3), but the average sea-ice concentration of the summer is well represented in these marginal seas. The discrepancy in winter in the Greenland and Barents Seas is mainly due to errors concerning the location of the sea ice edge. There the sea-ice concentration is overestimated, which also reveals the concentration maps (Figure 3.1 and 3.2). Despite less sea ice in summer the representation of sea ice is well simulated in the Greenland Sea. Additionally the summer sea-ice edge north of Svalbard does not coincide well and discrepancies of more than 20 % are seen. Summarizing,

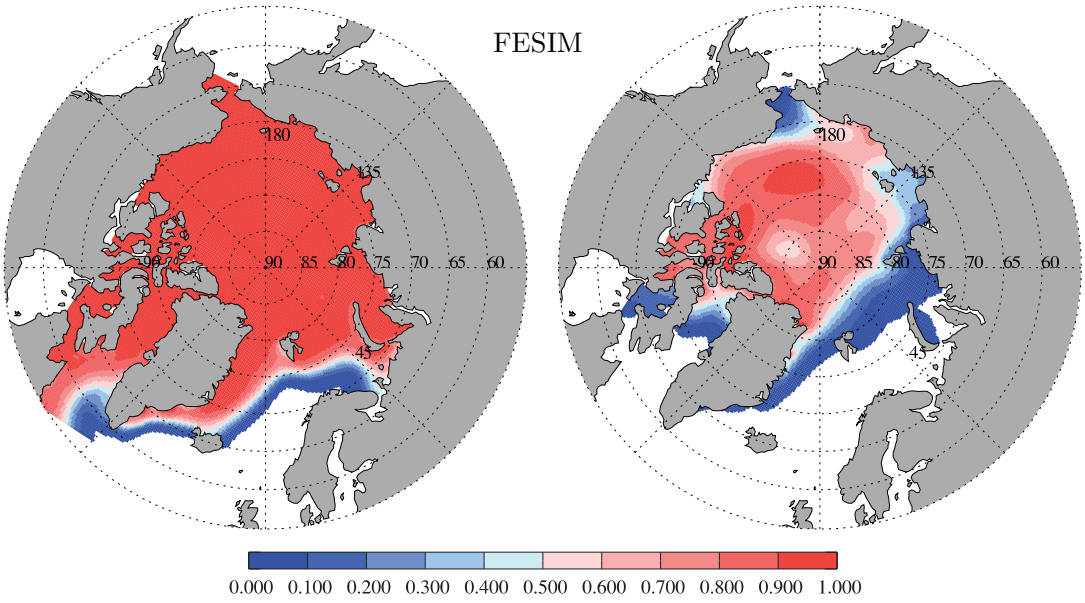

Figure 3.1: Winter (left) and summer (right) mean (1978 - 2005) of simulated sea-ice concentration in the Arctic.

the winter sea-ice concentration agrees very well with the observations and is better represented than in summer.

The summer sea ice extent has a larger variability (approximately 2.5 million km^2) than the winter sea-ice extent (approximately 0.5 million km^2)(Figure 3.4). This is due to the continents around the Arctic Ocean which limit the winter sea-ice extent and its variability. The summer sea-ice extent is not that much restricted by the coastal boundaries and is more dependent and sensitive to warmer atmospheric and oceanic conditions. Thus, the modeled September sea-ice extent (Figure 3.5) is compared with the observed summer sea-ice extent from *Stroeve et al.* (2005). The minima and maxima in summer sea-ice extent coincide qualitatively, except for the year 1993, but the absolute values of the observation are smaller (cf. Figure 2 from *Stroeve et al.* (2005)). This is most likely due to the overestimation of sea-ice concentration in the Beaufort Sea and also partially in the Siberian Seas (Figure 3.1). In these Arctic regions the highest annual summer variability occurs. For example the FESIM simulation in September 2002 - 2004 shows almost no open water in the Beaufort Sea contrary to the satellite derived concentration data. The model produces compact and thick sea ice such that a more compact ice cover is maintained during summer, which leads to the conclusion that the summer sea-ice thickness is overestimated or the drift conditions support sea-ice overestimation in that region.

In addition to a large variability of the sea-ice extent a continuous sea-ice decline is prominent in recent years (Figure 3.5). This agrees with the observed sea ice decline (*National Snow and Ice Data Center*, 2005) which is mainly revealed in summer with fluctuating minima of sea ice extent. The observed trend of decreasing sea ice between

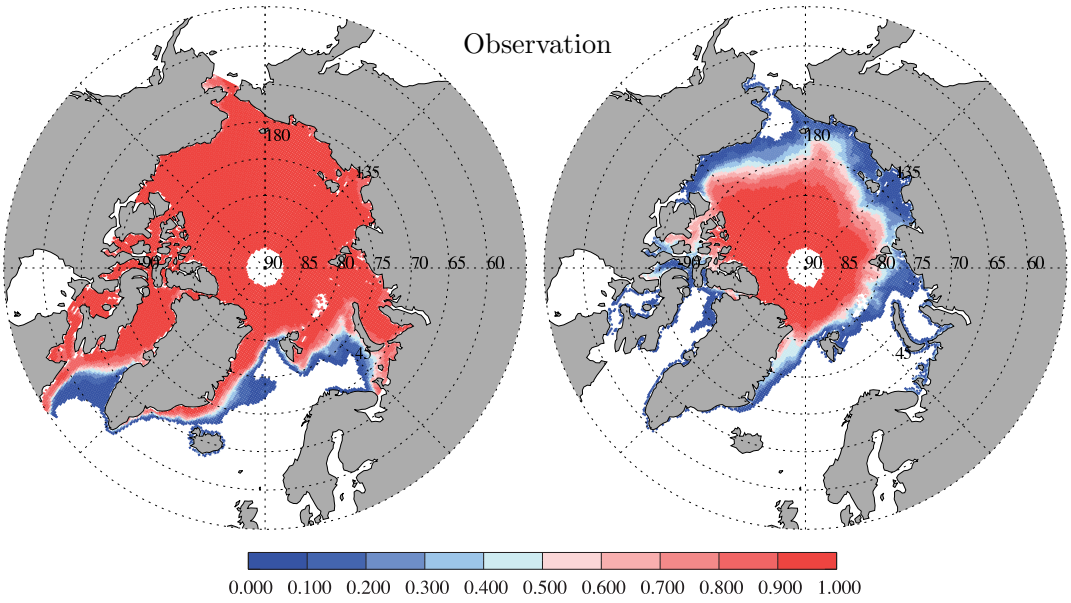

Figure 3.2: Winter (left) and summer (right) climatology of observed sea-ice concentration in the Arctic.

1979 and 2005 amounts to -7.4 % per decade (*IPCC*, 2007). The trend in the model simulation results in -4.7 % per decade for the same period but intensifies for the recent 15 years to -6.3 % per decade. Consequently the observed sea-ice decline is reproduced qualitatively by the model.

3.2 Sea-Ice Drift

The sea-ice drift varies within short time scales due to the high variability of the atmosphere. The wind forcing has a temporal resolution of one day and affects mostly the sea-ice drift. Therefore the drift pattern change within a few days which is well reproduced by the sea-ice model. However, on long-time scales the typical drift pattern, the Beaufort Gyre and Transpolar Drift Stream (TDS), are prevalent with various intensities and the more steady ocean currents have a significant effect on the drift.

Two typical drift regimes are discussed and compared with satellite derived observations. This is on the one hand the January 1994, where a distinct Beaufort Gyre appears (Figure 3.6) and on the other hand the January 1995 where the TDS dominates in the Arctic (Figure 3.8). These two typical drift regimes are simulated well by FESIM, especially the direction is very well represented (Figure 3.7 and 3.9). Discrepancies in the drift direction occur only close to the coast in both cases and in the center of the gyre in January 1994. These are areas where slow drift predominates and small differences in velocities components lead to directional differences.

Differences between simulated and observed speeds are more obvious (Figure 3.6 and

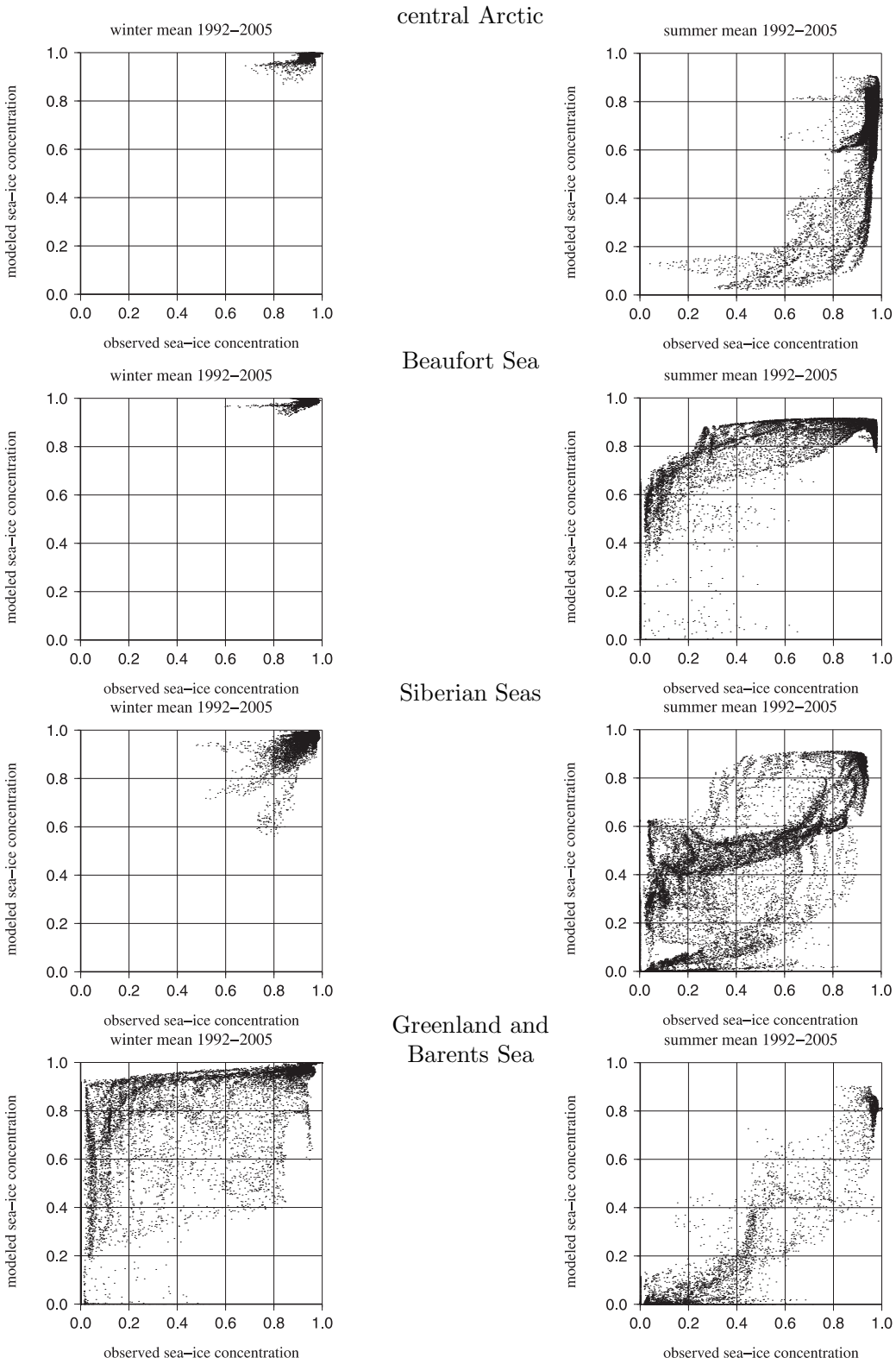

Figure 3.3: Modeled vs. satellite sea-ice concentration data: monthly means of March (winter, left) and September (summer, right) from 1992-2005 for the Central Arctic (latitude $> 81^\circ$ N), Beaufort Sea, Siberian Seas (including Chukchi, East Siberian, Laptev and Kara Sea), and Greenland and Barents Sea.

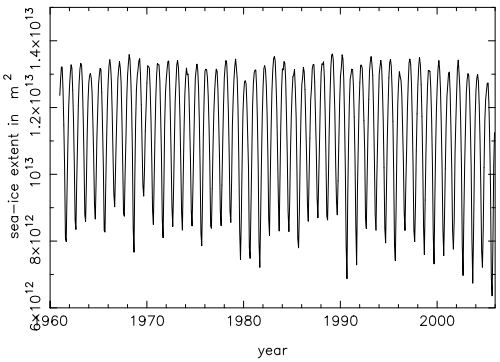

Figure 3.4: The seasonal cycle of sea-ice extent from 1961 - 2005.

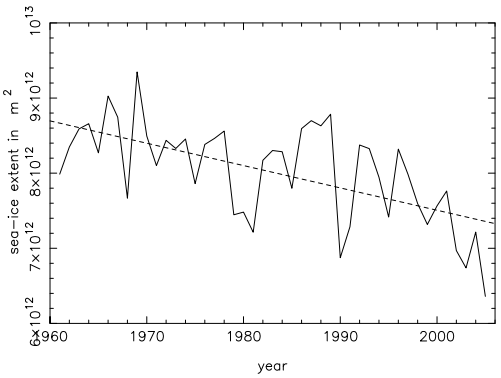

Figure 3.5: Temporal change of the simulated September mean of the Arctic sea-ice extent from 1961 - 2005 (solid line). The linear regression indicates a decrease of ice extent of about -3.7 % per decade (dashed line).

Figure 3.8). The velocities are overestimated for the Beaufort Gyre by approximately 8 - 10 cm s^{-1} especially at the outer boundary of the gyre (Figure 3.7). In contrast, the velocities in the TDS are underestimated by approximately 3 - 5 cm s^{-1} (Figure 3.9). Usually the ice concentration is between 90 and 100 % in January, and the resistance of sea-ice to wind stress is strong, and small differences in sea-ice concentration affect the drift but since FESIM overestimates the concentration in both month by about 2 - 5 % the model should either underestimate or overestimate the drift in both cases. The wind forcing data uncertainties might be one reason for the various differences. Also the different sea-ice thicknesses might be responsible because the thickness influences the internal forces as well as the concentration (Equation (2.48)). The sea-ice thickness distribution for both months is a bit different. The simulated thick ice feature of more than 3.50 m in the Beaufort Sea and in the north of Canadian Archipelago (Figure 3.13) is more pronounced in January 1995 than in January 1994. In course of the simulation the simulated thicker ice might cause an additional resistance (underestimation of ice speed) for the sea-ice drift through the Arctic, which was not observed. Unfortunately, there are no continuous sea-ice thickness observations over the entire Arctic to verify the thickness conditions.

A continuous inadequate tendency in sea-ice velocities for specific drift regimes leads consequently to a trend in sea-ice thickness and concentration distribution. An underestimated drift across the Arctic decreases the transport of thick ice polewards and a dynamic thinning in the Beaufort Sea is suppressed. An overestimated ice drift like for the Beaufort Gyre leads to an increased transport to the East Siberian Sea, where sea ice can accumulate. Still, the sea ice in the Beaufort Sea is not decreasing because the strong drift parallel to Greenland and Canadian Archipelago delivers additional sea ice. This process is not abrupt or instantly because the ice mass can be moved some kilometers within a month: for a velocity of 8 cm s^{-1} this corresponds to a displacement

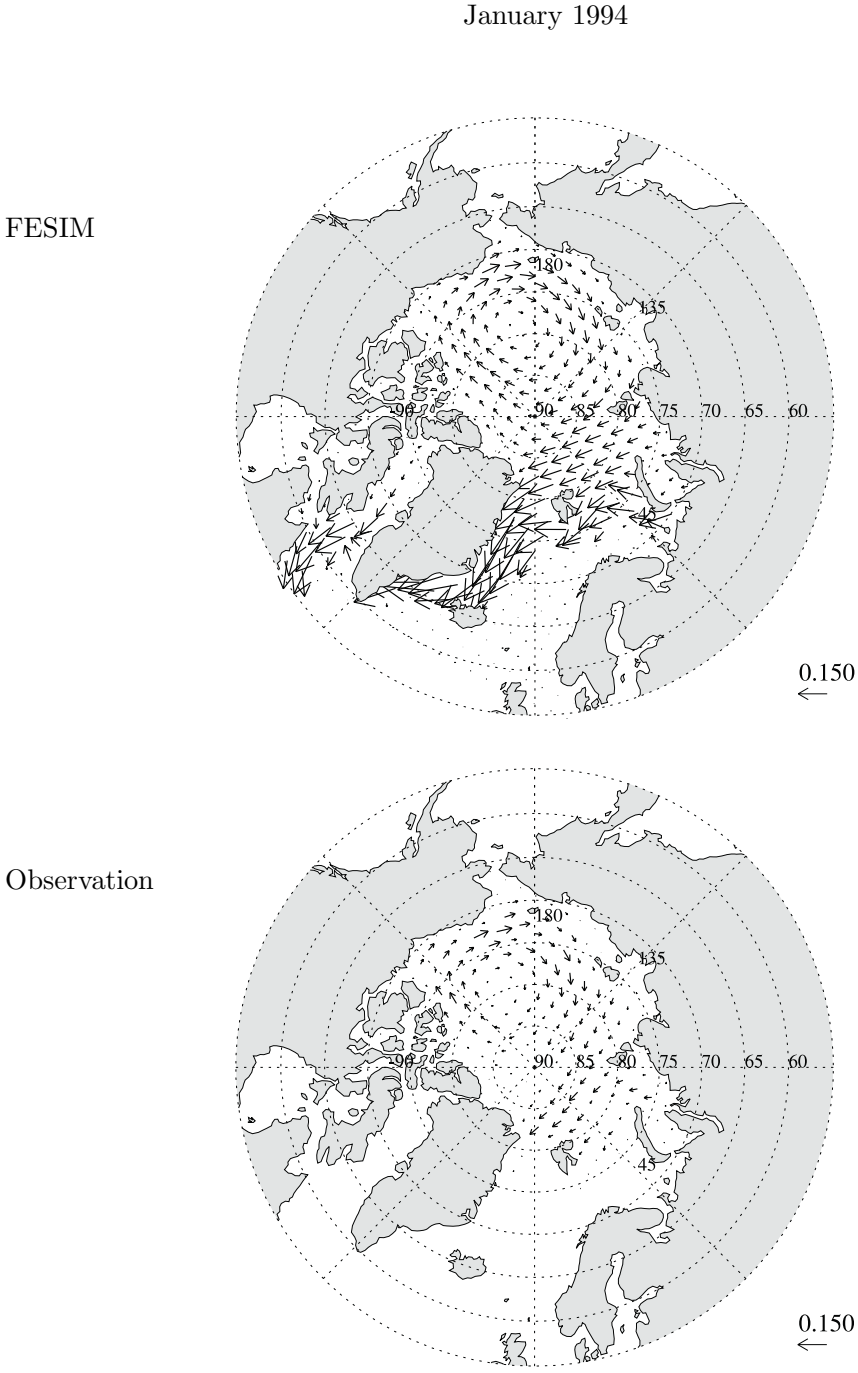

Figure 3.6: Monthly mean sea-ice velocity [$\mathrm{m\,s^{-1}}$] of January 1994 with a strong Beaufort Gyre: simulation (top) and observation (bottom).

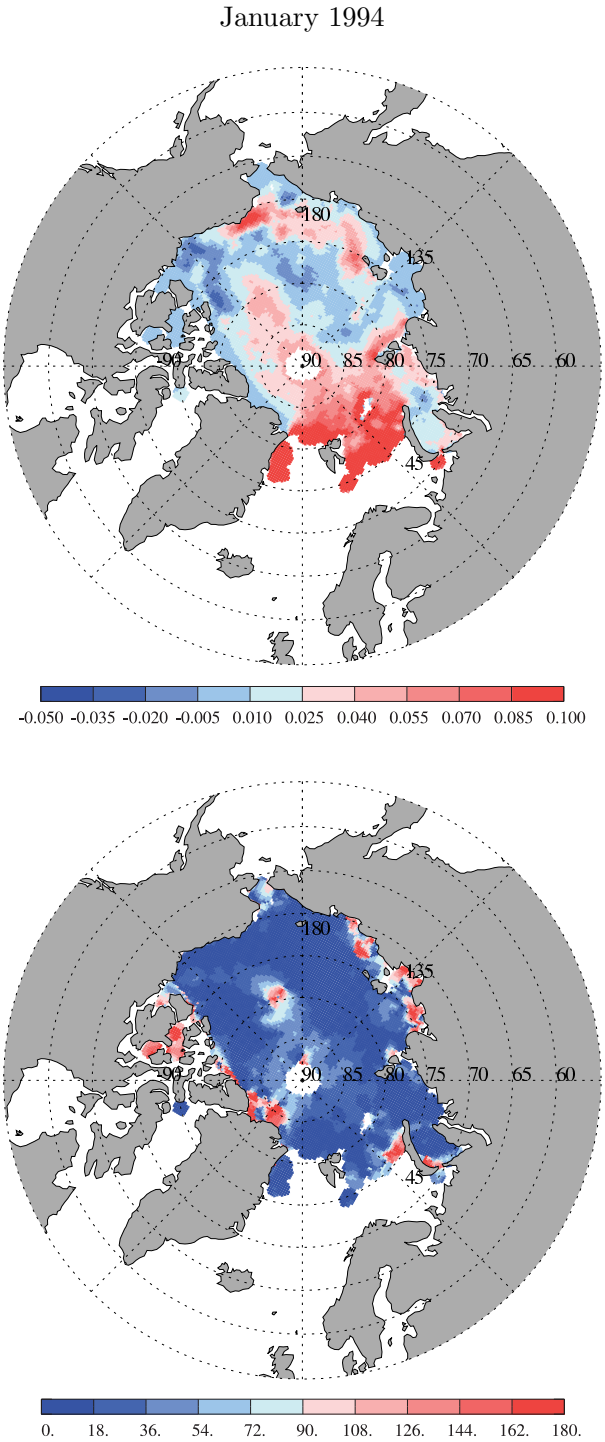

Figure 3.7: The sea-ice velocity difference [$\mathrm{m\,s^{-1}}$] (top) and absolute direction difference [°] (bottom) of simulated and observed drift vectors for January 1994.

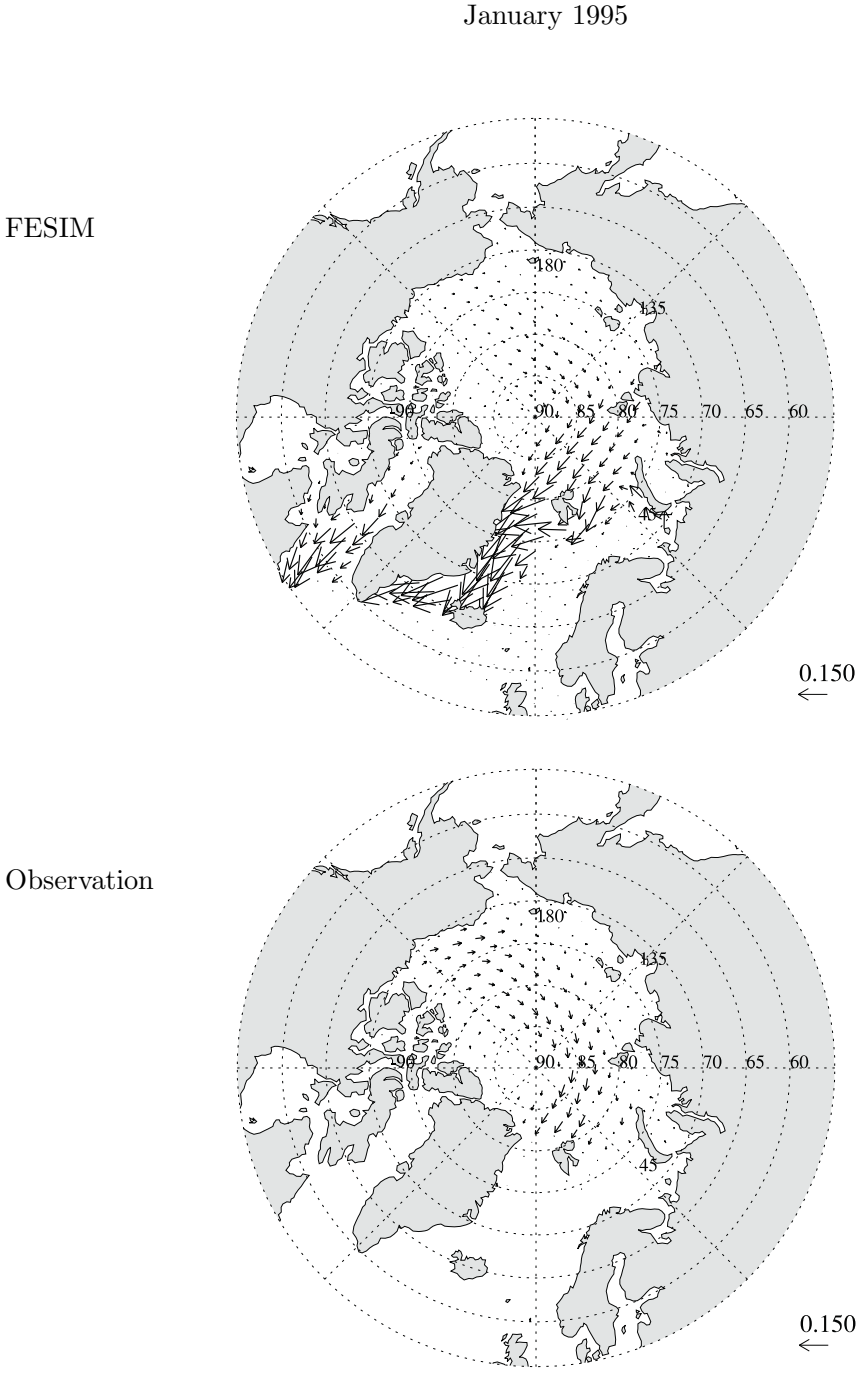

Figure 3.8: Monthly mean sea-ice velocity [$\mathrm{m\,s^{-1}}$] of January 1995 with Transpolar Drift Stream: simulation (top) and observation (bottom).

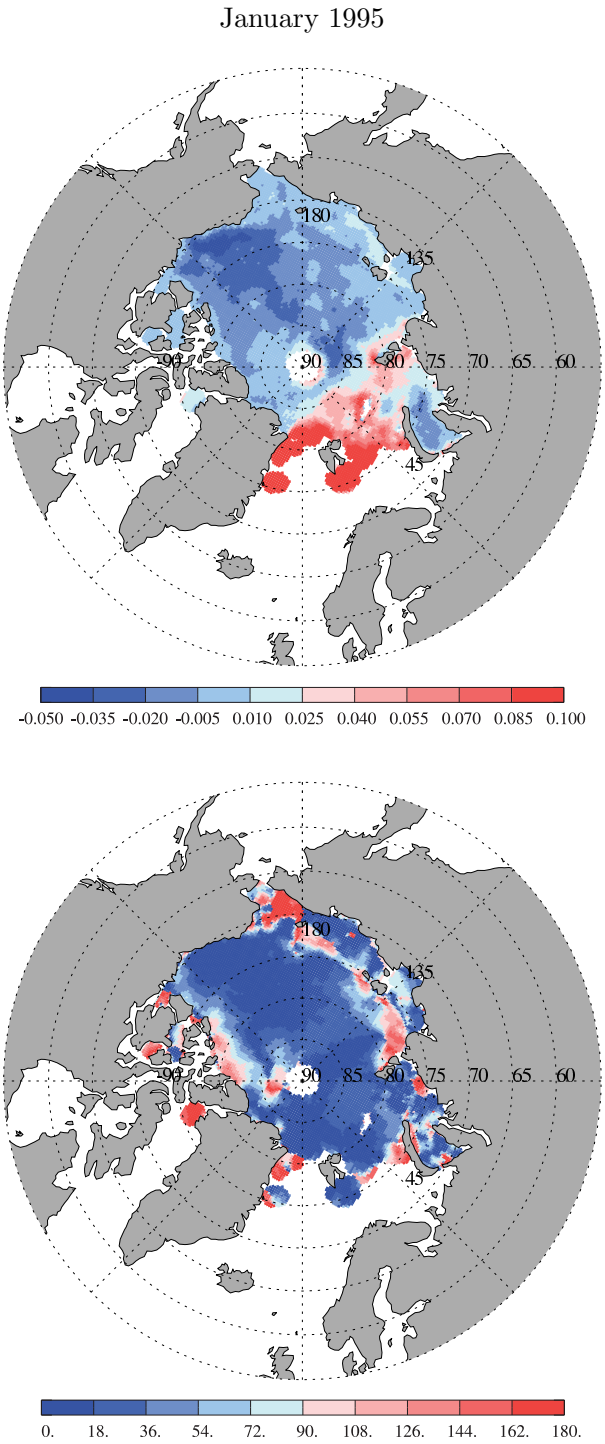

Figure 3.9: The sea-ice velocity difference [$\mathrm{m\,s^{-1}}$] (top) and absolute direction difference [°] of simulated and observed drift vectors for January 1995

January - March, 1992 - 2005

FESIM

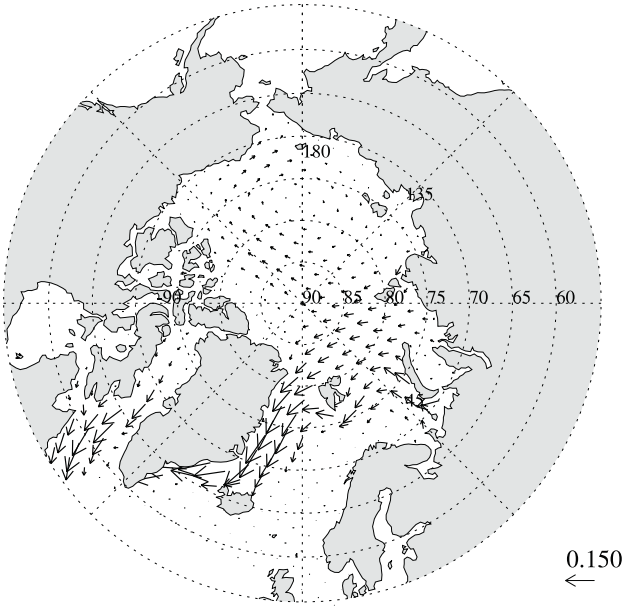

FESIM-Observation

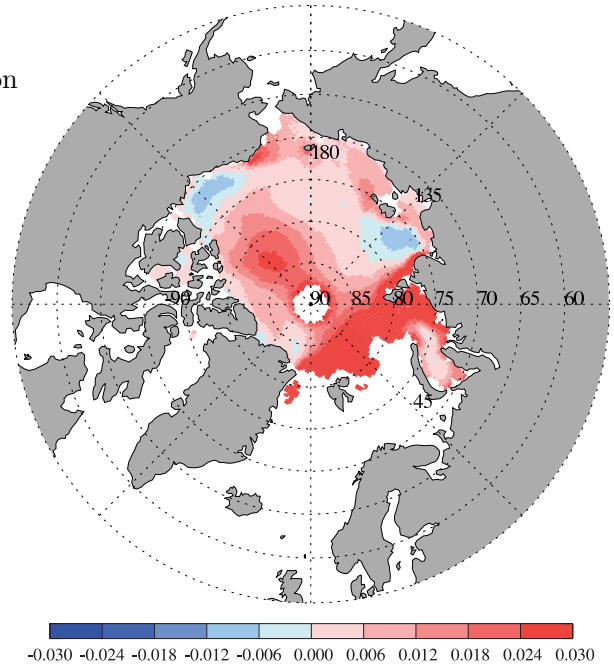

Figure 3.10: General sea-ice circulation of January - March from 1992 - 2005 (top) and mean sea-ice velocity difference [$\mathrm{m\,s^{-1}}$] (bottom) of simulated and observed drift vectors for same period.

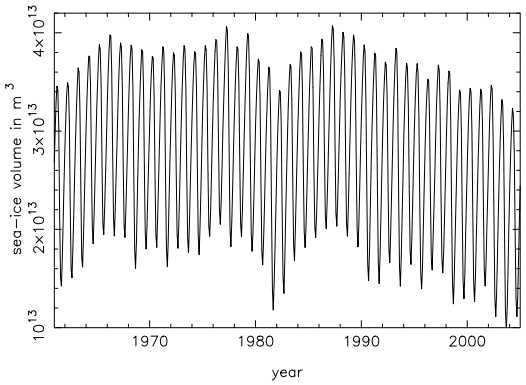

Figure 3.11: Simulated seasonal cycle of sea-ice volume for 1961 - 2005.

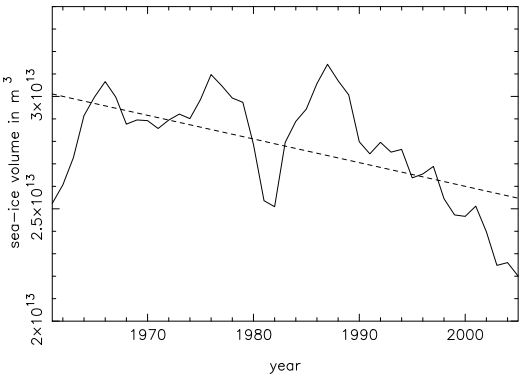

Figure 3.12: Annual mean of sea-ice volume in the Arctic from 1961 - 2005 (solid line). The linear regression indicates a decrease of sea-ice volume of about -3.8 % per decade (dashed line).

of approximately 200 km and for 3 $\mathrm{cm\,s^{-1}}$ approximately 75 km. However, if such a tendency is maintained over the years it is evident that too much sea ice remains in summer in the Beaufort Sea such that the sea-ice concentration is higher than observed. The mean difference of sea-ice velocity of the winter months January-March of the years 1992 - 2005 (Figure 3.10, bottom) reveals an underestimated velocity in the Beaufort and Laptev Sea and a more distinctive overestimation of sea-ice drift across the pole towards the Beaufort Sea regarding the mean drift field (Figure 3.10, top). Thus, it can be concluded that more sea ice is accumulated in winter in the Beaufort Sea, which also explains the overestimated summer sea-ice concentration. By the assimilation of sea-ice drift observations it is aspired to cure such a bias in the sea-ice motion and obtain a sea-ice drift representation that is even closer to the observations.

3.3 Sea-Ice Volume and Thickness

The seasonal cycle of sea-ice volume amounts to approximately $2{\cdot}10^{13}$ $\mathrm{m^3}$. It is mainly due to thermodynamic processes. The absolute minima and maxima are fluctuating significantly from year to year (Figure 3.11). The variability of the annual mean ice volume (Figure 3.12) is compared with that of *Hilmer and Lemke* (2000). The minima and maxima coincide qualitatively. The long-term trend of FESIM volume results is -3.8 % per decade and corresponds to that of *Hilmer and Lemke* (2000). For the years 1978 - 2005 the negative trend increases to -7.8 %. FESIM features less sea-ice volume, which is probably due to different grid and time resolution as well as different boundary conditions, e.g. for the ocean.

Changes in total sea-ice volume are correlated to export events or to periods with little sea-ice export. In 1981 much sea ice was exported through the Fram Strait (*Martin*

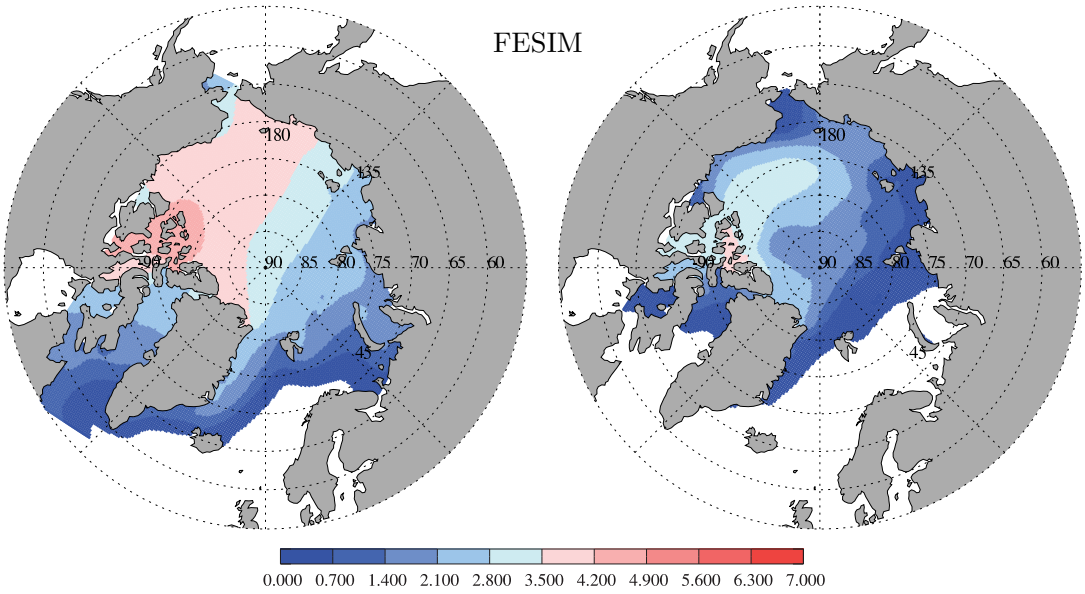

Figure 3.13: Winter (left) and summer (right) mean (1978 - 2005) of simulated sea-ice thickness [m] in the Arctic.

and Martin, 2006), which coincides with a volume loss (Figure 3.12). In 1985 less ice was transported out through the Fram Strait, which leads to a growing sea-ice volume because the sea ice was recirculated in the Arctic Basin. Since the end of the 1980s there were rarely periods with little ice export, and frequent export events lead to a lasting decrease in the sea-ice volume. However, the decline cannot be explained only by export events, because *Martin* (2007) shows that between 1997 and 2000 a reduced export occurred similar to that in 1985 and the volume did not increase as much as in the mid 1980s (Figure 3.12). An observed lengthened melt season since the late 1980s (*Belchansky et al.*, 2004) indicates warmer temperatures, which leads to an increased ice albedo feedback and sea ice loss. The warming might be responsible for a stagnating or even decreasing ice volume in a period of little ice export.

The FESIM setup produces a maximum sea-ice thickness of 4 - 5 m in winter which is less than *Bourke and Garrett* (1987) and *Rothrock et al.* (2003) have observed. In summer the thick ice reduces to 3 m (Figure 3.13). The thickest sea ice appears at the coast north of Greenland, Canadian Archipelago, and in the Beaufort Sea. In winter the thickness decreases towards the Laptev, Kara, Barents and Greenland Sea. A similar winter distribution was derived from observations from several submarine cruises between 1960 and 1982 (*Bourke and Garrett*, 1987) but there the 2 m isoline passes the East Siberian Sea into the Bering Strait which is not the case for FESIM sea-ice thickness results. The number of observations for the Laptev and East Siberian Seas was very small and may not provide a true depiction of mean sea-ice values. Thus, there the ice conditions can be generally more severe (*Bourke and Garrett*, 1987). The contour maps derived from ULS data of some submarine cruises indicate very thick ice of 5 - 7 m (occasionally 8 m) as

a narrow band along the Greenland-Canadian-Archipelago coast in winter (*Bourke and Garrett*, 1987; *Bourke and McLaren*, 1992). The model is able to simulate this feature only for few winters with maximum thicknesses between 4 - 5 m. The simulated mean sea-ice thickness distribution, however, is realistic.

For summer thickness the comparison is somewhat more difficult. There, the summer thickness pattern derived from ULS data reveals up to 7 m thick mean sea ice draft at the northern coast of Greenland and an extension of 4 m thick sea ice draft towards the pole which represents the multi-year sea ice (*Bourke and Garrett*, 1987; *Bourke and McLaren*, 1992). A similar summer distribution with up to 3 m thick sea ice near the pole and a decrease of ice down to 1 m in the Beaufort Sea was also reported by *Rothrock et al.* (2003). Such a feature has to be dynamic, because the seasonal maps presented in *Bourke and Garrett* (1987) indicate a sea-ice accretion near the pole from spring to summer which cannot be due to thermodynamic growth. The pattern of thickest ice between the North Pole and the Lincoln Sea cannot be reproduced in any year of simulation because FESIM simulates the thickest sea ice in the Beaufort Sea in summer (Figure 3.13, right).

The drift conditions north-east of Greenland and north of Svalbard are important for sea-ice export and recirculation. A slightly different drift direction decides if ice is transported out of the Arctic or towards the northern coast of Greenland, or parallel to that coast, which results in a recirculation of ice into the Arctic Basin. The differences between modeled and observed sea-ice drift occur in that region (Figure 3.7 and 3.9). The overestimated drift impedes cumulating and thickening of sea ice which is also supported by the overestimated velocity trend across the Arctic (Figure 3.10). Additionally the apparent drift tendency leads to an overestimation of sea ice in the Beaufort Sea and seems to be one reason for the thickness distribution with thickest ice in that area (Figure 3.13). On the basis of the sparse sea-ice thickness observations the Arctic sea-ice thickness seems to be more variable even on large scales within a year than the current model setup can simulate. This variability seems to be due to dynamic processes. One of the goals of this study is to improve the seasonal thickness variability by assimilation of sea-ice drift data.

4 Sea-Ice Data Assimilation Results

In this section the sea-ice drift data assimilation results are presented. The focus lies on two time periods: winter 2004 and autumn 2000. For the winter 2004 the assimilated drift is examined as well as the ability of the SEIK Filter to provide physical reliable states of the sea-ice concentration and thickness which are considered as unobserved in terms of data assimilation. That means that the SEIK Filter has only observation informations for the sea-ice motion. For the second time period of autumn 2000 a validation of sea-ice drift, concentration and thickness is done, as well as a sea-ice thickness variability study. In addition, the ensemble variability and the mass conservation during the data assimilation are discussed. Further, the results obtained using the Local SEIK Filter are also presented for the winter 2004 case to point out the differences in the assimilation results between the SEIK and Local SEIK Filters.

4.1 SEIK Filter Set-up

For the data assimilation of sea-ice drift with the SEIK Filter the model state includes the sea-ice velocity components, thickness, concentration, snow thickness, ocean temperature and salinity. Since the SEIK Filter framework has no information about the model, it appears that the model integration is incoherent and multiple for a prognostic variable that is only known in the model but not known in the the state vector of the SEIK Filter framework. Thus, the ensemble state in this framework contains all prognostic variables of each ensemble member.

An ensemble of 23 model state realizations are initiated with the initial covariance matrix $\mathbf{P}_0^a$ (c.f. Section 2.2.2) around the initial model mean state $\mathbf{x}_0^a$. The initial mean state is created from an appropriate prior model simulation corresponding to the initial simulation time. For the construction of the initial covariance matrix $\mathbf{P}_0^a$ more than 23 different model states of monthly means (either monthly means from different years and/or different months of prior model simulations) are used to compute a first guess of the model variability. Since the time interval between two SEIK analyses is three days due to the three day mean drift observations, the initial correlations derived from monthly mean values, e.g. between sea-ice velocity and thickness, is biased. This is explained easily because the advection of sea-ice within a month is larger than within three days. Therefore, the initial correlation between drift and thickness is overestimated regarding a three day assimilation period. However, this bias is reduced by the assimilation method due to the ensemble integration and the forecast covariance estimation.

From the forecasted ensemble the forecast covariance $\mathbf{P}^f$ is calculated. The observation error is estimated as described in Section 2.3.1. The measurement operator $\mathbf{H}$ linearly interpolates the forecasted state onto the observation location using the values from

the three grid points of the element in which the observation is located. Since the observation data are provided in geographical coordinates and the model computes the sea-ice velocity components on the rotated model grid the observations are processed such that the drift vectors are rotated onto the model grid. Then the forecasted and observed drift vectors correspond to the model grid. For the examination of the simulation and assimilation results the velocity components are rotated back to the geographical grid.

As suggested by *Pham* (2001) a forgetting factor is applied for the analysis so that the forecast error estimation is inflated (c.f. Equation (2.122)) and the observation is given more confidence. Some tests with different forgetting factors have been done. It is found that the choice of the forgetting factor of 0.8 provides the best results for the presented set-up. A model error covariance matrix $\mathbf{Q}$ is not employed.

The SEIK Filter re-initialization procedure can produce unphysical states. If the forecast phase starts with these model states the sea-ice model causes numerical instabilities. Thus, the unphysical states have to be replaced with nearby physical values.

4.2 Case Study I: Winter 2004

In this section a four month active assimilation period from January to April 2004 is presented. For the sea-ice drift validation the independent data set of drifting buoy data are utilized. The sea-ice concentration is validated with satellite derived sea-ice concentration data. Additionally, the last analysis state ensemble is further integrated without assimilation until end of May because there are HEM sea-ice thickness data for two days in May 2004 which are used to verify thickness estimation of the assimilation results. It is not known if the variables, the sea-ice concentration and thickness, that provide no observation information in course of the assimilation, are maintained in a physical state by the statistical data assimilation method. Therefore, it is examined if the SEIK Filter with sea-ice drift observations alone is able to estimate realistically the sea-ice concentration and thickness.

4.2.1 Validation of Sea-Ice Drift

To validate the sea-ice velocity modification due to the assimilation procedure the Arctic-wide sea-ice velocity root mean squared (rms) error from the observed sea-ice velocity is determined :

$$\mathrm{rmse}(t) = \sqrt{\frac{1}{N(t)} \sum_{i=1}^{N(t)} \left(\sqrt{[\mathbf{H}u_i^{\mathrm{m}}(t)]^2 + [\mathbf{H}v_i^{\mathrm{m}}(t)]^2} - \sqrt{[u_i^{\mathrm{o}}(t)]^2 + [v_i^{\mathrm{o}}(t)]^2} \right)^2} \qquad (4.1)$$

with $N(t)$ the number of observations at time t, $\mathbf{H}u_i^{\mathrm{m}}(t)$ the forecasted or analyzed zonal velocity at the observation location i, $\mathbf{H}v_i^{\mathrm{m}}(t)$ the forecasted or analyzed meridional velocity at the observation location i, $u_i^{\mathrm{o}}(t)$ the observed zonal velocity and $v_i^{\mathrm{o}}(t)$ the observed meridional velocity. In Figure 4.1 the black triangles are the rms errors between the forecasted/analyzed and observed sea-ice velocity. The rms error of the analysis state is connected with a line to the rms error of the following forecast state. The change from

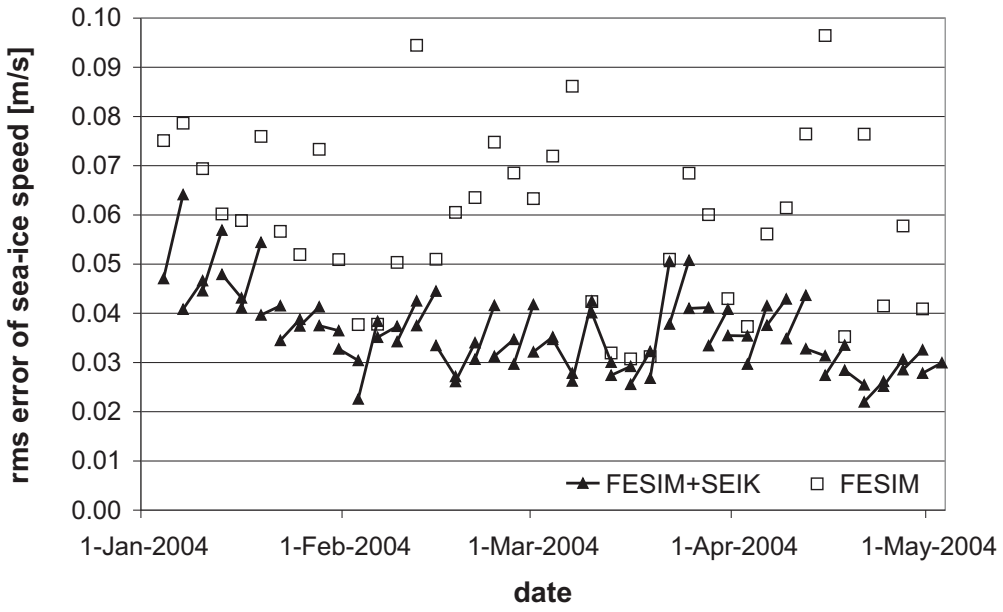

Figure 4.1: Arctic-wide averaged sea-ice velocity rms error of the reference simulation (squares) and assimilation (triangles) with respect to the observed sea-ice velocity. The lines between triangles represent the change of sea-ice velocity rms error due to model forecast integration before the next SEIK analysis. The alteration between triangles at same date represents the corrections by the SEIK Filter analysis.

the forecast to the analysis at the same time represents the averaged sea-ice velocity correction done by the SEIK Filter analysis. These corrections vary between a few $\mathrm{mm\,s^{-1}}$ and 2 $\mathrm{cm\,s^{-1}}$ (overall mean is 0.4 $\mathrm{cm\,s^{-1}}$) at different dates. The analysis-derived sea-ice velocities corrections lead to a decrease of the deviation. The Arctic-wide averaged drift derived from the assimilation procedure shows that the SEIK Filter analysis produces an almost constant drift rms error between 2 - 5 $\mathrm{cm\,s^{-1}}$ relative to the satellite observations (Figure 4.1). In contrast, the reference simulation has a large scatter of Arctic-wide averaged drift rms error (empty squares) from 2 $\mathrm{cm\,s^{-1}}$ up to 10 $\mathrm{cm\,s^{-1}}$. The difference compared to the observation is reduced by the SEIK Filter and remains almost constant. It should be mentioned that the approximated observation error is about 1.6 $\mathrm{cm\,s^{-1}}$ on average. The SEIK Filter setup is therefore not able to reduce the deviation below the observational error. However, from 1 January to 30 April 2004 the mean drift deviation is reduced from 5.8 $\mathrm{cm\,s^{-1}}$ (no assimilation) to 3.6 $\mathrm{cm\,s^{-1}}$ (with assimilation).

The comparison of Arctic-wide derived sea-ice drift vectors with satellite-derived drift vectors reveals that the difference between the mean sea-ice drift of assimilation and reference simulation in the first two months appears rather small (Figure 4.2). However, the filter reduces most of the drift deviations (see Figure 4.1). For the last two months, March and April, a better drift behavior is achieved. The SEIK Filter was able to

Observation

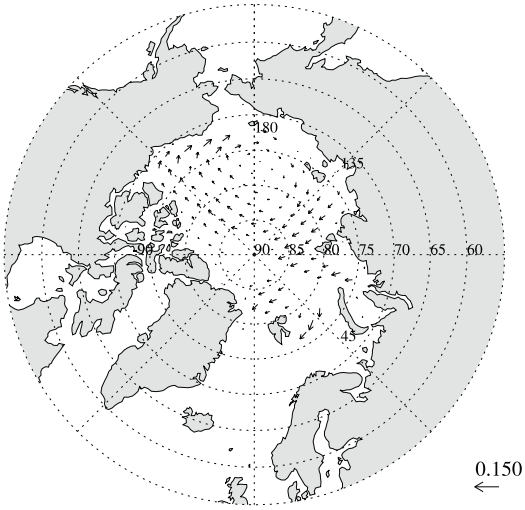

FESIM

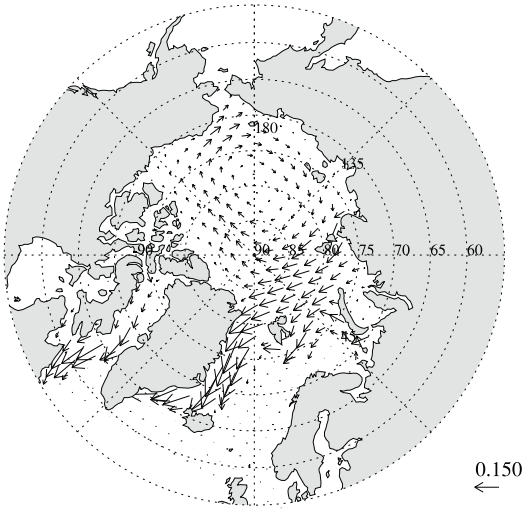

FESIM+SEIK

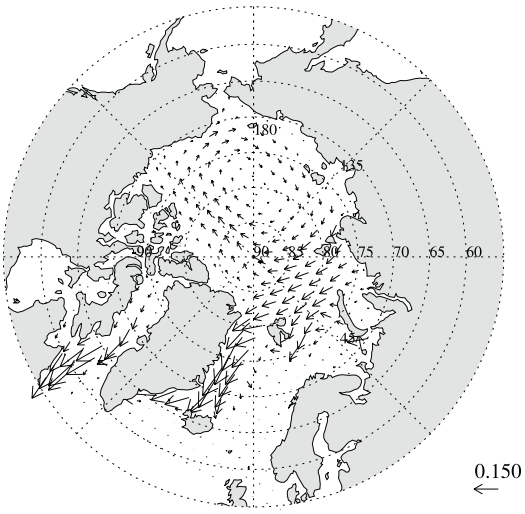

Figure 4.2: Sea-ice drift vectors [m s^{-1}] from 1 January - 29 February 2004 of satellite derived drift (top), reference drift simulation (center) and assimilation analysis drift results (bottom)

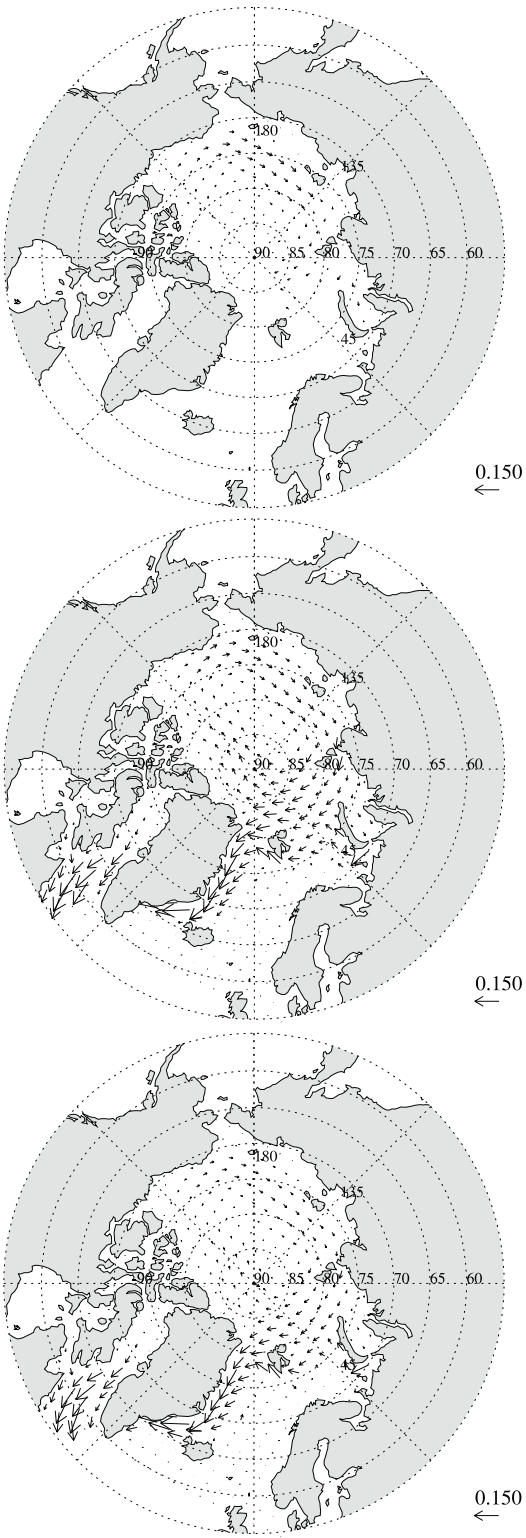

Figure 4.3: Sea-ice drift vectors [m s^{-1}] from 1 March - 30 April 2004 of satellite derived drift (top), reference drift results (center) and SEIK analysis drift results (bottom).

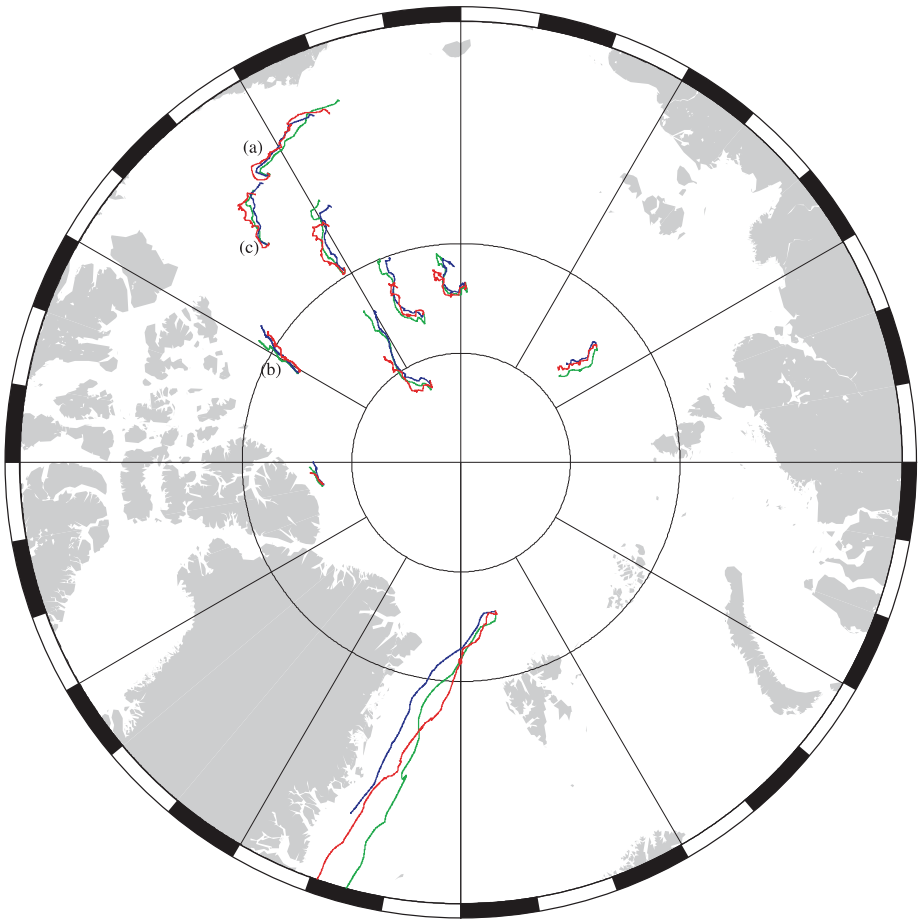

Figure 4.4: Arctic buoy trajectories from 1 January - 30 May 2004: red - deployed drifting buoys, green - trajectory from reference simulation, blue - trajectory from assimilation results. The trajectories of the buoys no. 3982 (a), 24293 (b), and 40299 (c) are displayed in more detail in Figure 4.5.

improve the large scale sea-ice drift significantly compared to the reference simulation so that the model drift agrees well with the observation. Especially the drift along the Greenland and Canadian coast is better represented with sea-ice drift assimilation (Figure 4.3).

The validation of sea-ice drift corrections is also done with buoy data. They are independent from the assimilation procedure because only satellite derived data are used for the data assimilation. The buoy data sets are spread over the Arctic Basin non-uniformly because the buoy deployment depends on regional sea-ice conditions and mainly on political frontiers (c.f. Figure 2.9). For example, on the Siberian shelves there are almost no buoys. Newly formed ice is transported out of this region by the Transpolar Drift Stream or can be melted in summer more easily due to thin ice, so

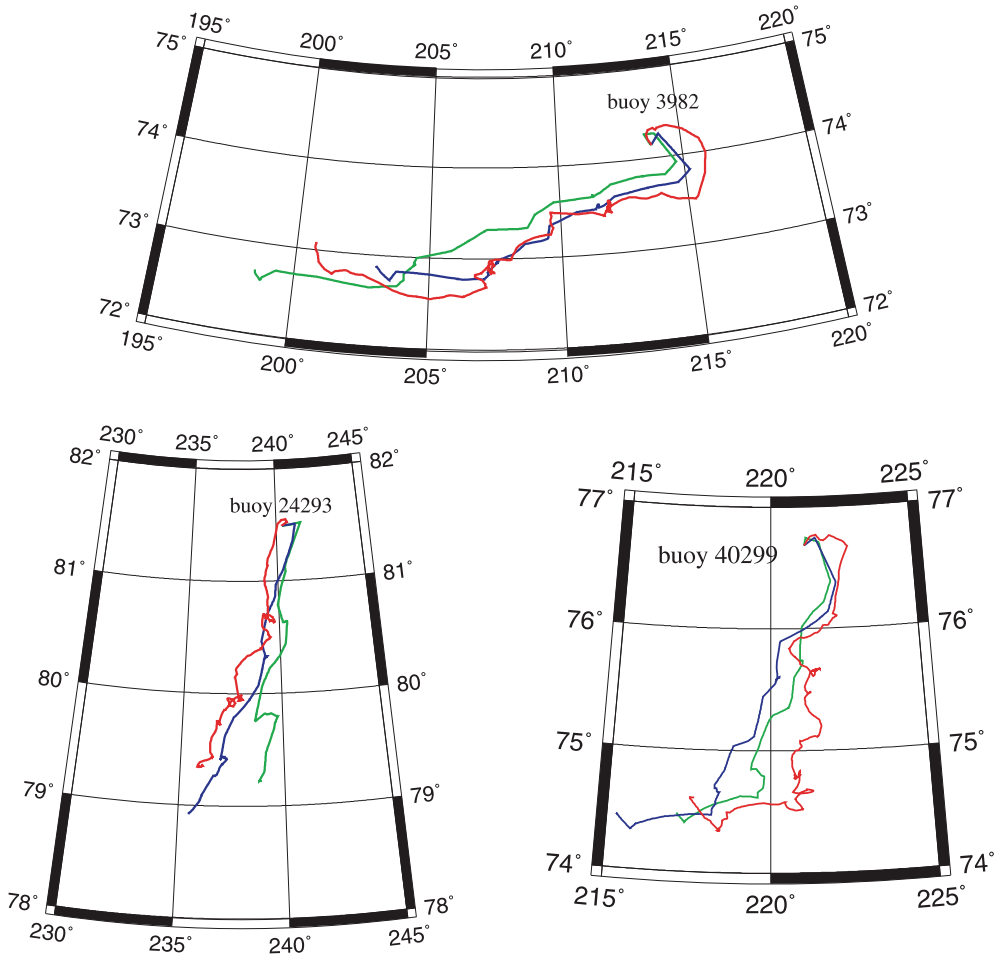

Figure 4.5: Three selected buoy trajectories from 1 January - 30 April 2004: buoy no. 3982 (top) between the Beaufort and Chukchi Seas, 24293 (bottom, left) in north of Canadian Archipelago and 40299 (bottom, right) in the Beaufort Sea. Red - deployed drifting buoy, green - trajectory from the reference simulation, blue - trajectory from the assimilation results.

that almost no multi-year ice can develop. Therefore, deployed buoys would survive only for a short time. Most buoys are deployed in the regions where ice accumulates and survives over several years, like in the Beaufort Sea or north of Greenland and the Canadian Archipelago.

Figure 4.4 shows sea-ice drift verification for Arctic buoy trajectories in the period from 1 January - 30 May 2004. The trajectories start at the true buoy location on 1 January 2004 and the reference simulation and assimilation drift results are taken to determine the artificial buoy tracks. So differences between the drift of buoy data and model simulation or assimilation can result in different tracks. No correction of the position regarding the buoy data are done for the artificial tracks (green and blue lines)

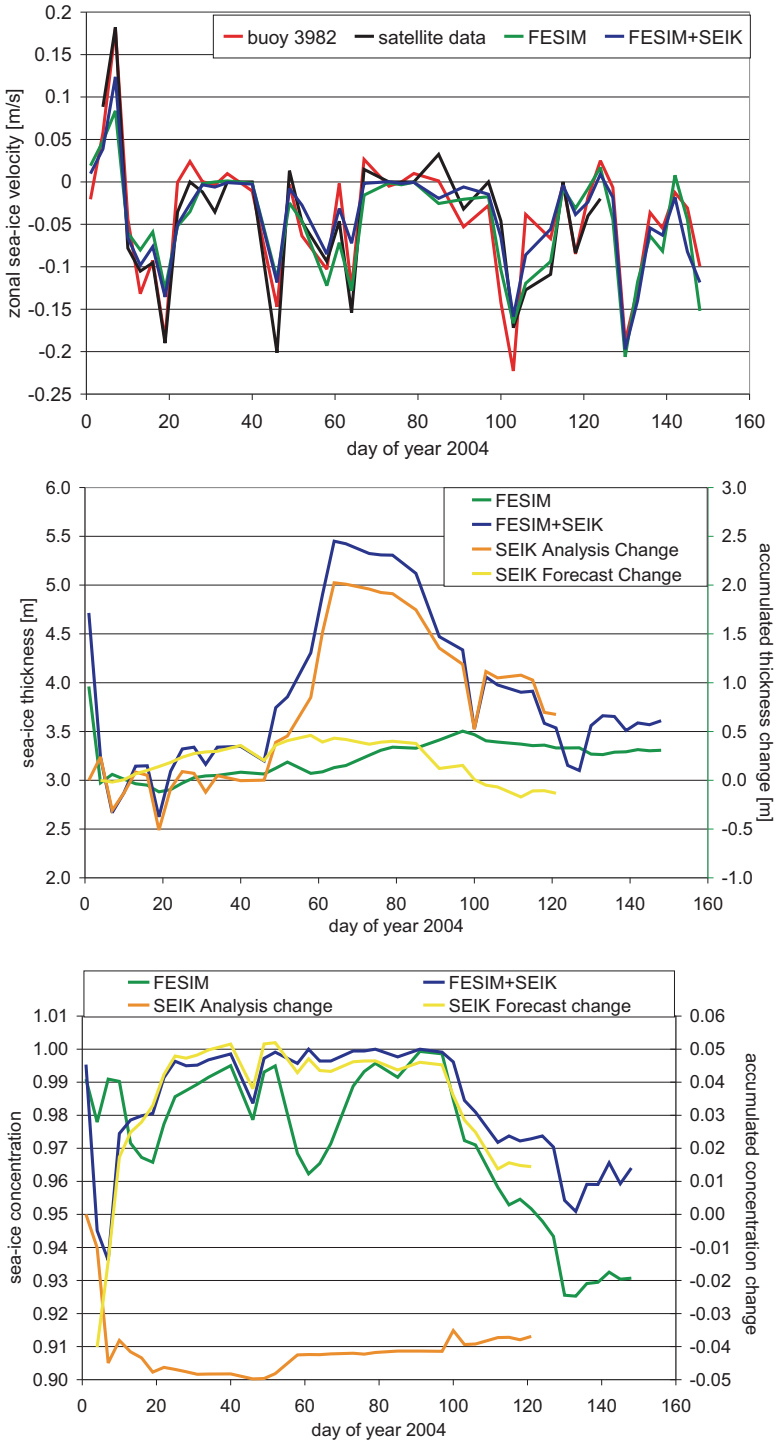

Figure 4.6: Sea ice properties along the trajectory of buoy no. 3982 (cf. Figure 4.5) zonal sea-ice velocity [$\mathrm{m\,s^{-1}}$] (top), sea-ice thickness [m] (center), and sea-ice concentration (bottom) with SEIK analysis and forecast change for sea ice thickness and concentration.

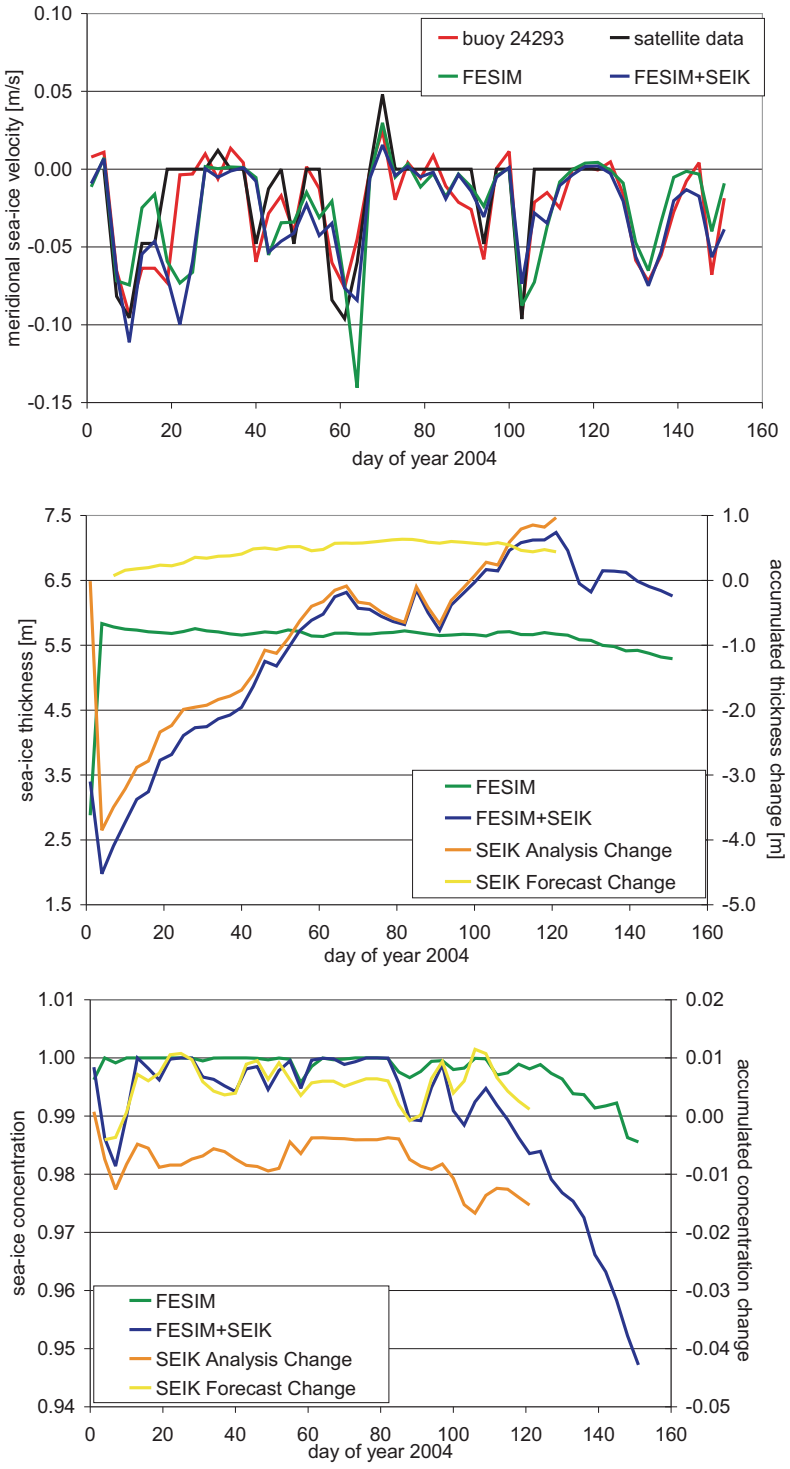

Figure 4.7: Sea ice properties along the trajectory of buoy no. 24293 (cf. Figure 4.5): meridional sea-ice velocity [$\mathrm{m\,s^{-1}}$] (top), sea-ice thickness [m] (center), and sea-ice concentration (bottom) with SEIK analysis and forecast change for sea ice thickness and concentration.

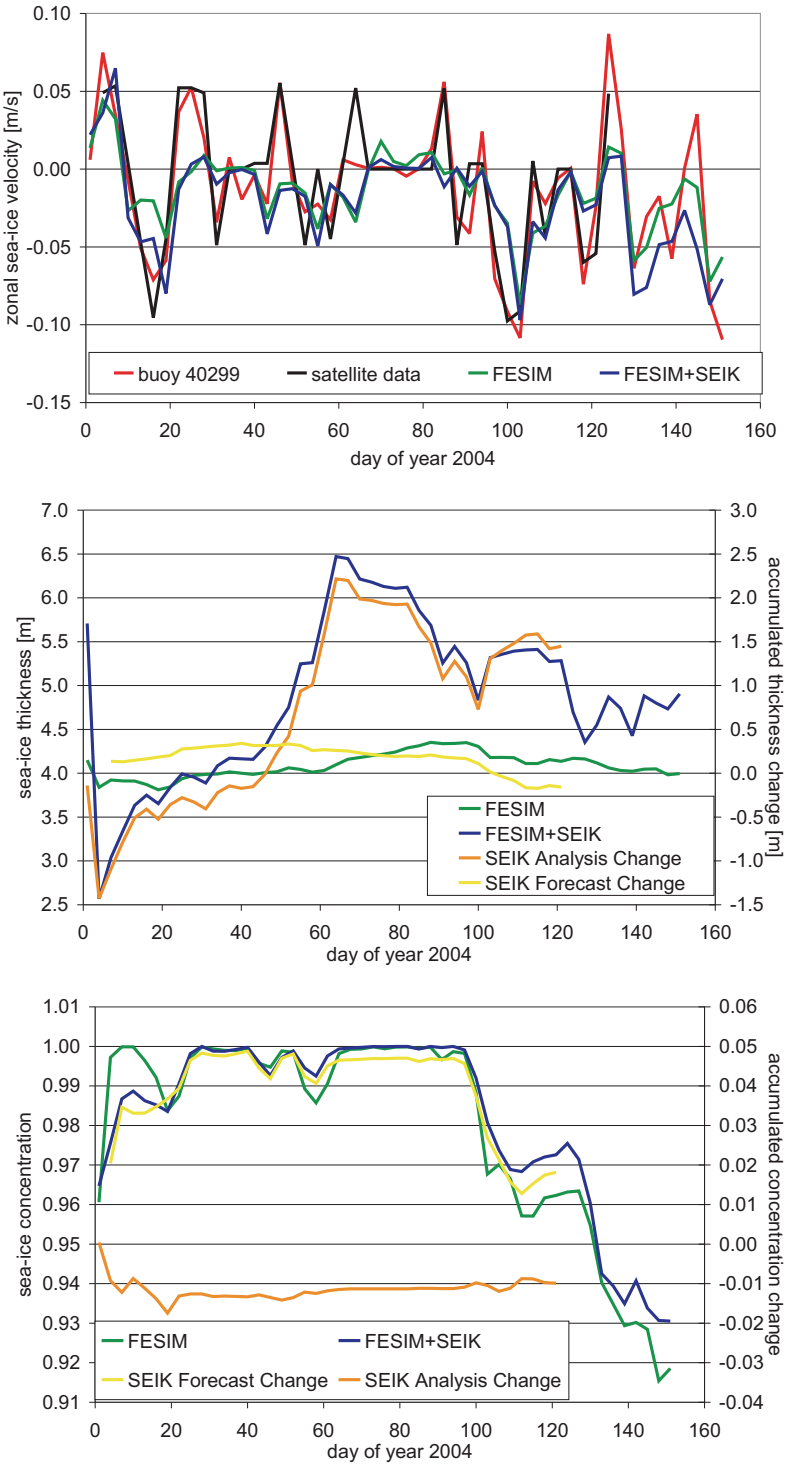

Figure 4.8: Sea ice properties along the trajectory of buoy no. 40299 (cf. Figure 4.5): zonal sea-ice velocity [$\mathrm{m\,s^{-1}}$] (top), sea-ice thickness [m] (center), and sea-ice concentration (bottom) with SEIK analysis and forecast change for sea ice thickness and concentration.

for the period considered. The reference simulation (green lines) already provides a good agreement with the observed trajectories (red lines). Therefore, the drift corrections are not expected to be large at all. In most cases the assimilation results (blue lines) are between reference and buoy trajectory. The corrections by the SEIK Filter are small as already shown. The selected buoy trajectories (Figure 4.5) show the wide range of drift corrections with regard to the independent data set of buoy position data. Both, speed and direction are modified by the assimilation. The sea ice conditions along these three buoy trajectories are discussed in more detail below.

Buoy 3982 The buoy no. 3982 is located in the Beaufort Sea and is advected towards the Chukchi Sea along the Alaskan coast (Figure 4.4). Partially the trajectory from the assimilation results (blue line) coincides exactly with the true buoy trajectory (red line) (Figure 4.5, top). The trajectory is determined mainly by the zonal sea-ice velocity component. The zonal sea-ice velocity along the true buoy trajectory (Figure 4.6, top) reveals that the simulations agree well with the observed velocities. Strong wind events causing sea-ice velocities of more than 0.1 $\mathrm{m\,s^{-1}}$ are well represented along this buoy trajectory. The first strong sea-ice drift event has been improved by the filter by reducing sea-ice concentration compared to the reference simulation (Figure 4.6, bottom). After the first assimilation steps only small differences in the simulated sea-ice velocities occur. The changes due to the assimilation procedure (yellow and orange lines in Figure 4.6, center and bottom) explains the striking differences between reference and assimilation results in the concentration and thickness along the true buoy track. More striking are the changes to the sea-ice thickness and concentration along the buoy trajectory (Figure 4.6). Here, larger changes in thickness and concentration coincide with the peaks of the velocity because the filter procedure features larger modifications in case of strong drift. When the sea-ice drift is very small the sea-ice conditions are maintained and the modifications due to data assimilation are small (Figure 4.6).

The thickness or concentration change due to the SEIK analysis is determined by the difference of the analyzed and forecasted thickness or concentration. The change due to the SEIK forecast is determined from the state difference between the previous analysis and current forecast state. The accumulated change is derived from the sum of these differences. The thickness changes along the buoy track are produced by the filter analysis as the accumulated thickness change in Figure 4.6 (center, orange line) reveals. It shows the same course as the assimilated thickness (Figure 4.6, center, blue line). In contrast, the SEIK derived sea-ice concentration is more dominated by the SEIK forecast (Figure 4.6, bottom, yellow line).

Buoy 24293 The buoy no. 24293 is located north of the Canadian Archipelago and is advected along the narrow branch of thick ice towards the archipelago (Figure 4.10, lower row). The buoy trajectory in the assimilation results shows changes in the drift direction and the speed (Figure 4.5, bottom, left, blue line). The drift, mainly represented by the meridional sea-ice velocity component in this case, along the true buoy trajectory shows that the peaks agree very well with the observations (Figure 4.7, top). The reference

simulation shows larger differences in the sea-ice velocity than for the buoy no. 3982.

Remarkable is the sea-ice state on day 60 where the reference sea-ice velocity (green line) is overestimated and the assimilation (blue line) results in a slower sea-ice velocity which is in this case due to the sea-ice thickness difference because the concentration is almost the same (Figure 4.7). Also, at the beginning of the simulations the buoy seems to be "advected" into an area of thicker sea ice. The reference simulation shows a strong leap from almost 3 to over 5 m sea-ice thickness. The assimilation results instead show an almost steady increase of sea-ice thickness which is due to the SEIK analysis thickness change (Figure 4.7, center, orange line). However, there are several effects included: sea-ice thickness along the track can be changed due to advection and thermodynamic growth. Additionally the SEIK Filter analysis introduces sea-ice thickness changes which actually provide the largest contribution. This is similar for the sea-ice concentration but the SEIK forecast and therefore the model physics are more dominant (Figure 4.7, bottom, yellow line). However, after the active assimilation (day 122) the drift representation is better for the ensemble mean state than for the reference simulation. Here, a mixture of higher thickness and less concentration compared to the reference simulation results in the improved sea-ice velocity.

Buoy 40299 The buoy no. 40299 is located in the Beaufort Sea in the region of the thick sea-ice (Figure 4.10, lower row). The buoy trajectory derived by the assimilation is underestimating or is even unable to produce the eastward sea-ice velocity component which is represented by the positive peaks of the zonal sea-ice velocity (Figure 4.8, top). This inability of producing eastward sea-ice velocities represents the main mismatch of true and virtual buoy (Figure 4.5, bottom, right). It seems that the simulated thick sea ice in the east of the buoy prevents drift eastwards for both simulations. The assimilation was not able to overcome this. In contrast, strong westward sea-ice velocities (values below -0.05 $\mathrm{m\,s^{-1}}$) agree well with the observations. The first eastward sea-ice drift event was improved by the assimilation due to reduced sea-ice thickness and concentration. Between day 20 and 100 a very compact sea-ice cover is present along the trajectory and the velocity is less well represented. After day 100 a strong drift event occurs which opens the ice cover and then the drift is better represented in both simulations. Actually, the drift is almost identical despite the different sea-ice concentration and thickness. During May, after the active assimilation, the velocity of the assimilation simulation deteriorates. As for the other sea-ice states along the trajectories, the SEIK analysis provides the largest contribution for the thickness change and the SEIK forecast for the concentration change (Figure 4.8, center and bottom).

4.2.2 Validation of Sea-Ice Concentration

Three-daily means of SSM/I satellite derived sea-ice concentration data for the time period of 1 January - 30 April 2004 were used for comparison with the three daily mean sea-ice concentration from the assimilation results. To investigate the representation of the sea-ice concentration the modeled vs. observed sea-ice concentration is plotted (reference run in the right column and assimilation results in the left column of Figure 4.9). A

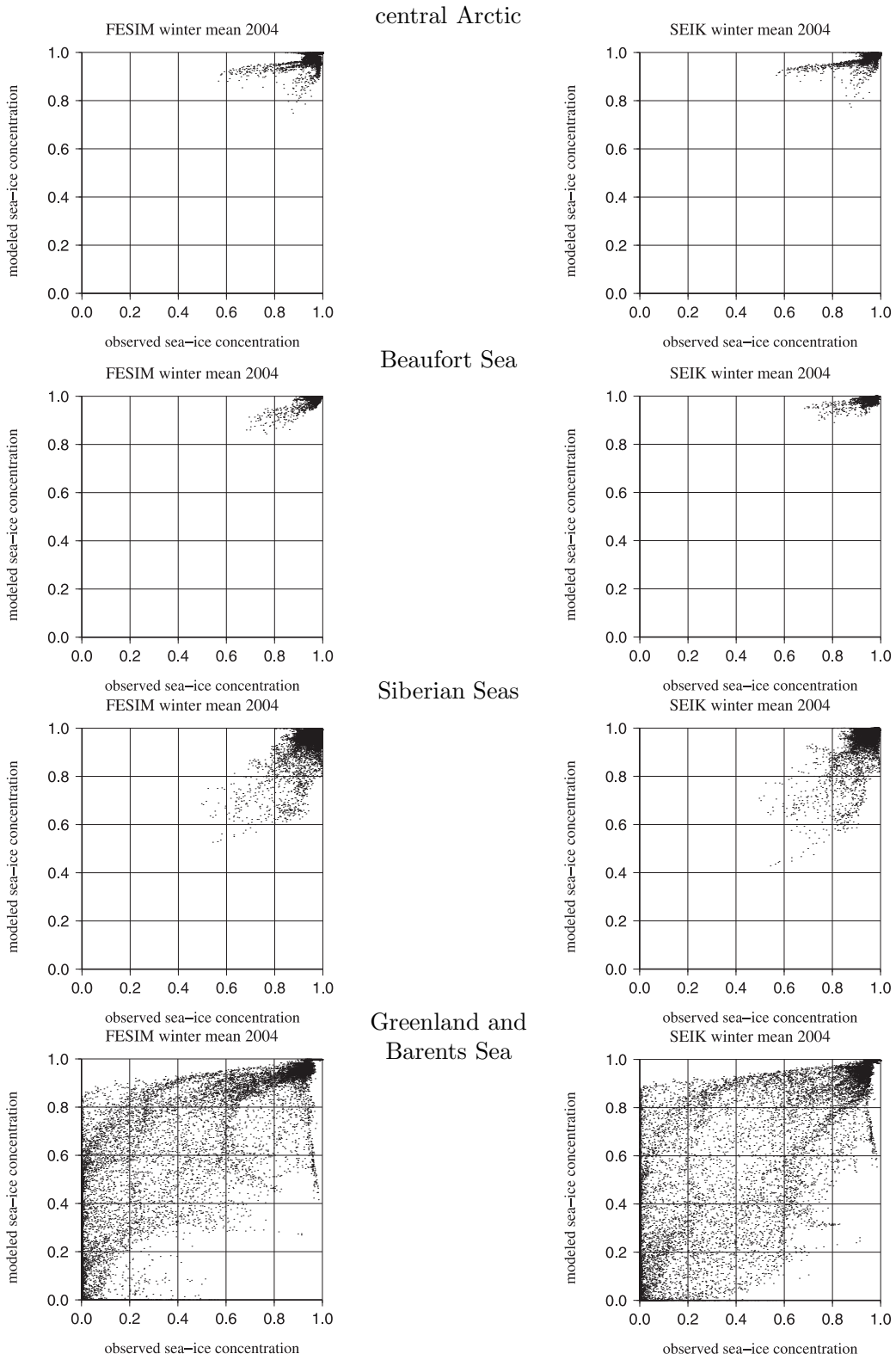

Figure 4.9: Modeled vs. observed sea-ice concentration: mean for 1 January - 30 April 2004; reference (left) and assimilation (right). Data are split into four regions: Central Arctic (latitude $> 81°$ N), Beaufort Sea, Siberian Seas (including Chukchi, East Siberian, Laptev and Kara Sea), and Greenland and Barents Sea.

slope of 1 represents a perfect match between model and observation. Figure 4.9 reveals that within the four months of assimilation the sea-ice concentration is as good as for the reference simulation. The model already produces good sea-ice concentration simulations for this season so that the assimilation can not improve the sea-ice concentration further in many cases (Figure 4.9). The representation of the sea-ice concentration in the central Arctic is close to 1, and observations show that compact ice conditions dominate this region in winter. The assimilation has slightly improved the results and the correlation coefficient increased from $R = 0.5$ (reference simulation) to $R = 0.6$ (assimilation). In the Beaufort Sea the correlation coefficient of $R = 0.4$ remains unchanged as well as in the Siberian Seas ($R = 0.5$) where also compact ice conditions are prevalent. In the Barents and Greenland Seas the reference simulation produces a higher correlation coefficient of $R = 0.9$ between simulated and observed sea-ice concentration than the assimilation ($R = 0.8$). Thus the reduced drift in March and April has to be caused by the thicker sea ice as a result from the assimilation. Then the sea-ice obtains a higher resistance to atmospheric and oceanic drag, and the assimilation produces a sea-ice drift which is closer to the observation than the reference sea-ice drift.

The SEIK Filter is able to estimate realistic sea-ice concentration distributions for four month which covers the whole period of sea-ice drift data assimilation. Thus, the sea-ice concentration does not deteriorate in course of the sea-ice drift assimilation except for the marginal ice zone. Due to rare drift data in these region and less correlations between drift and concentration and thickness it was not expected to improve the representation of sea-ice concentration in the Greenland and Barents Seas.

4.2.3 Evaluation of Sea-Ice Thickness

The assimilation has the largest impact on the sea-ice thickness. The assimilation of sea-ice drift observations results in significant sea-ice thickness modifications. The simulated sea-ice thickness pattern with assimilation agrees very well with the observed winter thickness pattern (*Bourke and Garrett*, 1987) although the absolute sea-ice thickness values can still differ substantially. Most striking is the sea-ice thickness extension into the Beaufort Sea as well as the narrow band of very thick sea ice along the Greenland and Canadian coast (Figure 4.10, bottom). This narrow feature of very thick compact ice along the archipelago the model alone can not produce at any time of simulation and can only be achieved with the assimilation.

The comparison with HEM sea-ice thickness measurements on 12 and 13 May 2004 reveals that the results of the continued simulation after the last assimilation overestimates the sea-ice thickness by about 3 m (Table 4.1). However, the observed gradient of decreasing sea-ice thickness along the meridional transect from the Canadian coast towards the North Pole is reproduced by the assimilation procedure. This gradient is also represented by the reference simulation (Table 4.1). Under the assumption that a generally overestimated sea-ice thickness is valid for the entire Arctic this leads to the conclusion that either the wind forcing or the transfer of momentum from the wind to the ice is overestimated or the internal force is estimated too small. Further the correlations of sea-ice drift and thickness are biased: If the observed sea-ice drift in compact

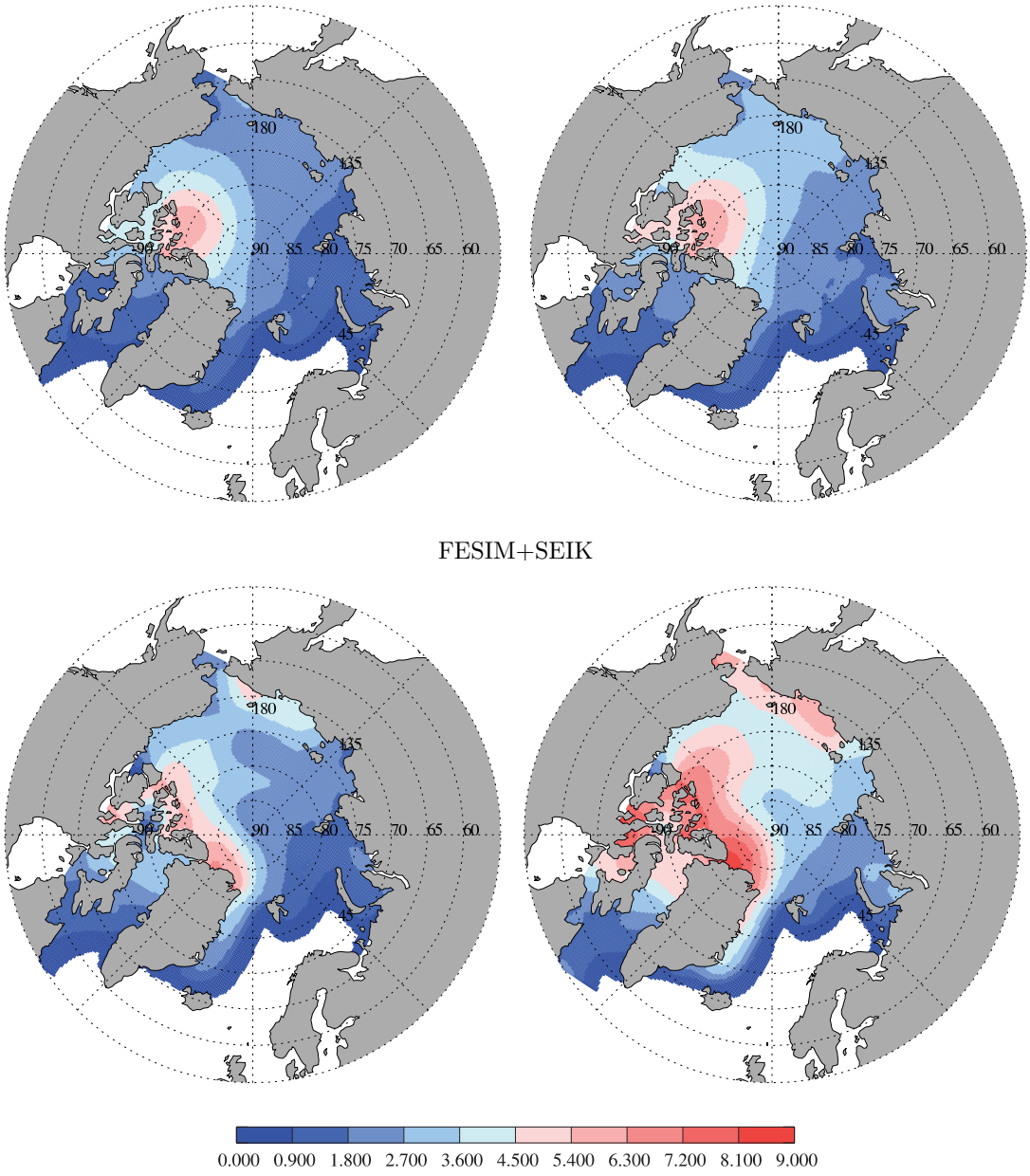

Figure 4.10: Arctic sea-ice thickness distributions for two time periods: 1 January - 29 February 2004 (left) and 1 March - 30 April 2004 (right) of reference simulation (top) and assimilation results (bottom).

Table 4.1: HEM data, from *Haas et al.* (2006), reference simulation (FESIM) and assimilation (FESIM+SEIK; drift data are available only until 30 April 2004; after April the results of the free ensemble computation are taken) results of sea-ice thickness and concentration data from 12 and 13 May 2004 on the nearby meridional transect between 62 W - 72 W from 82.5 N - 86 N.

	Sea-ice thickness [m]				Sea-ice concentration		
transect	HEM		FESIM	FESIM+	HEM	FESIM	FESIM+
	mode	mean		SEIK			SEIK
82.5-83.0° N	4.3	4.27	3.98	7.84	1.000	0.998	0.978
83.0-83.5° N	3.9	4.79	4.01	7.57	1.000	0.993	0.964
83.5-84.0° N	3.9	4.77	3.96	7.37	0.980	0.985	0.956
84.0-84.5° N	3.7	4.30	3.89	7.33	0.963	0.988	0.966
84.5-85.0° N	3.8	4.48	3.85	7.24	0.990	0.994	0.974
85.0-85.5° N	3.5	4.06	3.78	7.10	0.979	0.997	0.979
85.5-86.0° N	3.6	4.08	3.69	6.91	0.957	0.999	0.983
rms error		2.04	0.19 / 0.55	3.52 / 2.98		0.020	0.021
gradient	-0.21	-0.17	-0.10	-0.27			

sea-ice conditions are significant slower than the forecast drift, the cross correlations lead to an increasing sea-ice thickness update to reduce the overestimated modeled sea-ice drift. This results in an increased ice strength and larger resistance to the atmospheric and oceanic drag.

Based on the thickness values derived by ULS observations (*Bourke and Garrett*, 1987) it can be evaluated that the sea-ice thickness estimate is realistically represented in the first two months in the course of assimilation. With ongoing assimilation the thickness further increases to less reliable values and the sea-ice thickness has to be assessed with care. Thus, the sea-ice drift assimilation alone is not able to produce as reliable values for the sea-ice thickness over the whole assimilation period as is possible for the sea-ice concentration.

4.3 Case Study II: Autumn 2000

The assimilation results for autumn 2000 are presented in this section. This season is selected because the most recent ULS derived sea-ice thickness data are available for 13 - 31 October 2000. Earlier cruises are not selected because the merged SSM/I and Quikscat derived drift data are only available since 1999. These data have a larger coverage than the SSM/I only derived data available since 1991(*Ezraty and Piollé*, 2004a). A validation of all three sea-ice fields: drift, concentration and thickness, is done for October 2000. Again, for sea-ice drift validation the independent data set of drifting

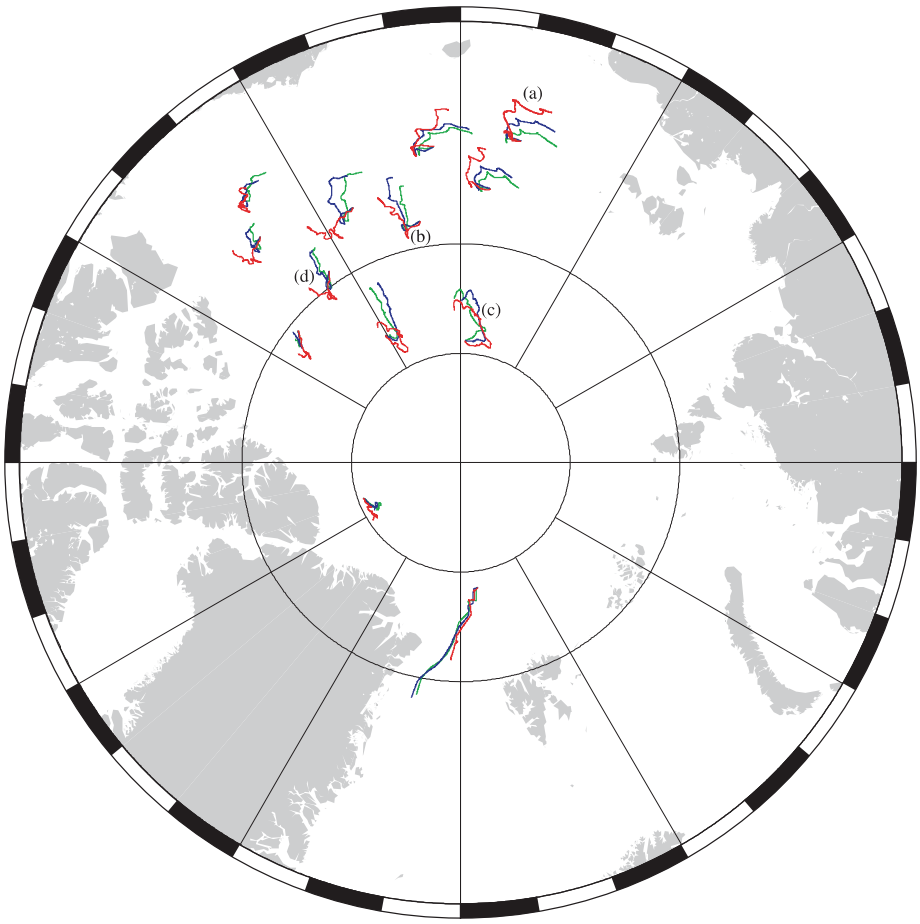

Figure 4.11: Arctic buoy trajectories from 1 October to 9 December 2000: red - deployed drifting buoys, green - trajectory from reference results, blue - trajectory from assimilation results. The trajectories of the buoys no. 24289 (a), 3691 (b), 3311 (c), and 20859 (d) are displayed in more detail in Figure 4.12.

buoy data is utilized. The sea-ice concentration is compared with satellite derived data. Under the assumption that the sea-ice drift assimilation procedure is able to estimate a reliable sea-ice state for at least 2 months, as a result from the previous section, a sea-ice variability study is done that covers the time period of mid of October until the beginning of December.

4.3.1 Sea-Ice Validation

Sea-Ice Drift

As a first test whether the sea-ice velocity was changed due to the assimilation, the satellite data is compared with the reference and assimilation results. It turns out that

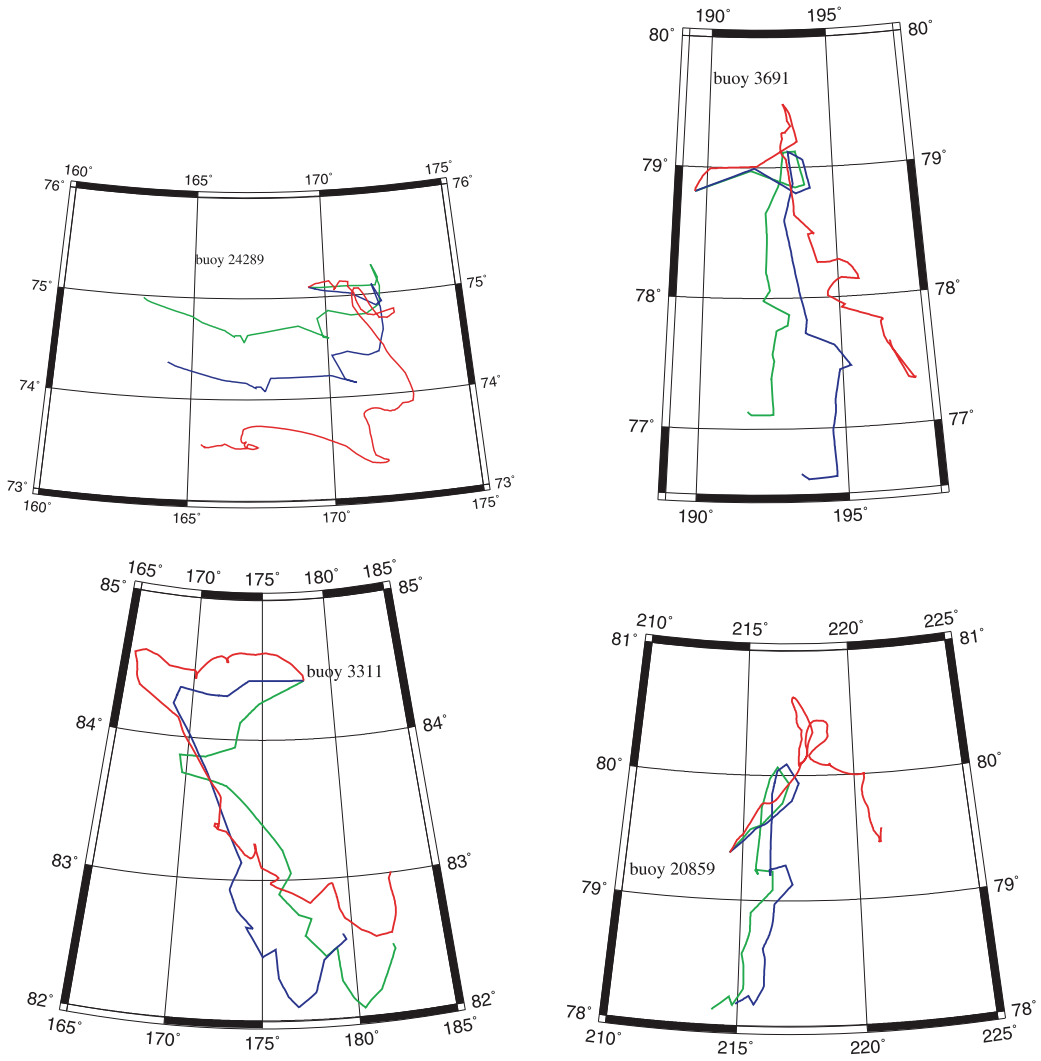

Figure 4.12: Four selected buoy trajectories covering the same period as in Figure 4.11: red - deployed drifting buoy, green - reference simulation, blue - assimilation results. Buoy no. 24289 (top, left) is located in the Chukchi Sea, buoy no. 3691 (top, right) in the northwesterly Beaufort Sea, buoy no. 3311 (bottom, left) between North Pole and Chukchi Sea, and buoy no. 20859 (bottom, right) in north of the Canadian Archipelago.

the drift modification from the SEIK Filter analysis is rather small and very similar to that of the forecast state and in some cases similar to the reference simulation. Thus, the SEIK Filter setup presented, produces less instantaneous analysis drift innovations but rather a progress of drift improvement with ongoing assimilation. However, a more comprehensive sea-ice drift validation can be done with a set of Arctic drifting buoy position data.

A comparison of observed and simulated trajectories (Figure 4.11) reveals that the drift modification due to the assimilation (blue lines in Figure 4.11) is not uniform. There are areas where the drift is closer to the observed buoy trajectories (red lines) like in the Chukchi Sea and areas where the drift is almost unchanged compared to the reference simulation (green lines) like in the north of Fram Strait. Near the ice edge, where a less compact ice cover is present, the correlations between drift and thickness and concentration are less distinct compared to the central Arctic. The current SEIK Filter setup is not adequate to modify the drift sufficiently in these regions as will be discussed later. On the other hand, the drift in the Chukchi Sea and partly in the Beaufort Sea is significantly improved due to the assimilation. Thus it is expected that the modified sea-ice thickness and concentration are also improved in these areas. Near the Canadian coast and north of Greenland the drift was small in that period and all data sets, observation, reference and assimilation trajectory almost coincide (Figure 4.11).

Four selected buoy trajectories (Figure 4.12) reveal the diversity of achieved drift correction in more detail. Here, the assimilated drift (blue lines) results in trajectories which are located between the derived trajectories from the reference simulation (green lines) and the observed buoy tracks (red lines). Since the SEIK Filter does not replace model data by observed data but treats both states as two possible solutions, it is expected to obtain trajectories which are closer but not identical to the observations. Although the validation with the independent buoy drift data reveals the drift improvement by the assimilation there is still a bias in the assimilation procedure so that the model state is given more confidence to. That is due to the fact that the estimated forecast drift error is smaller than the approximated observation error which is discussed in Section 4.4. Therefore, the comparison shows also in some cases drift behavior more similar to the model reference than to the observation as for the buoy no. 20859 (Figure 4.12, lower right) which is located in the north of the Canadian Archipelago. There the sea-ice conditions are similar for the reference simulation and the assimilation results. This underlines the fact that this SEIK Filter setup does not obtain drift improvement from the the analysis drift innovation alone. The buoy trajectories of the assimilation results in the Chukchi (buoy no. 24289) and Beaufort Sea (buoy no. 3691) and also in the central Arctic (buoy no. 20859) differ significantly from those of the reference drift. These buoys are located in areas where the assimilated thickness is significantly different from the reference simulation (Figure 4.15) which is shown later.

Sea-Ice Concentration

Similar to the winter 2004 case study, three-daily means of satellite derived sea-ice concentration data are used for comparison with the three daily mean sea-ice concentration

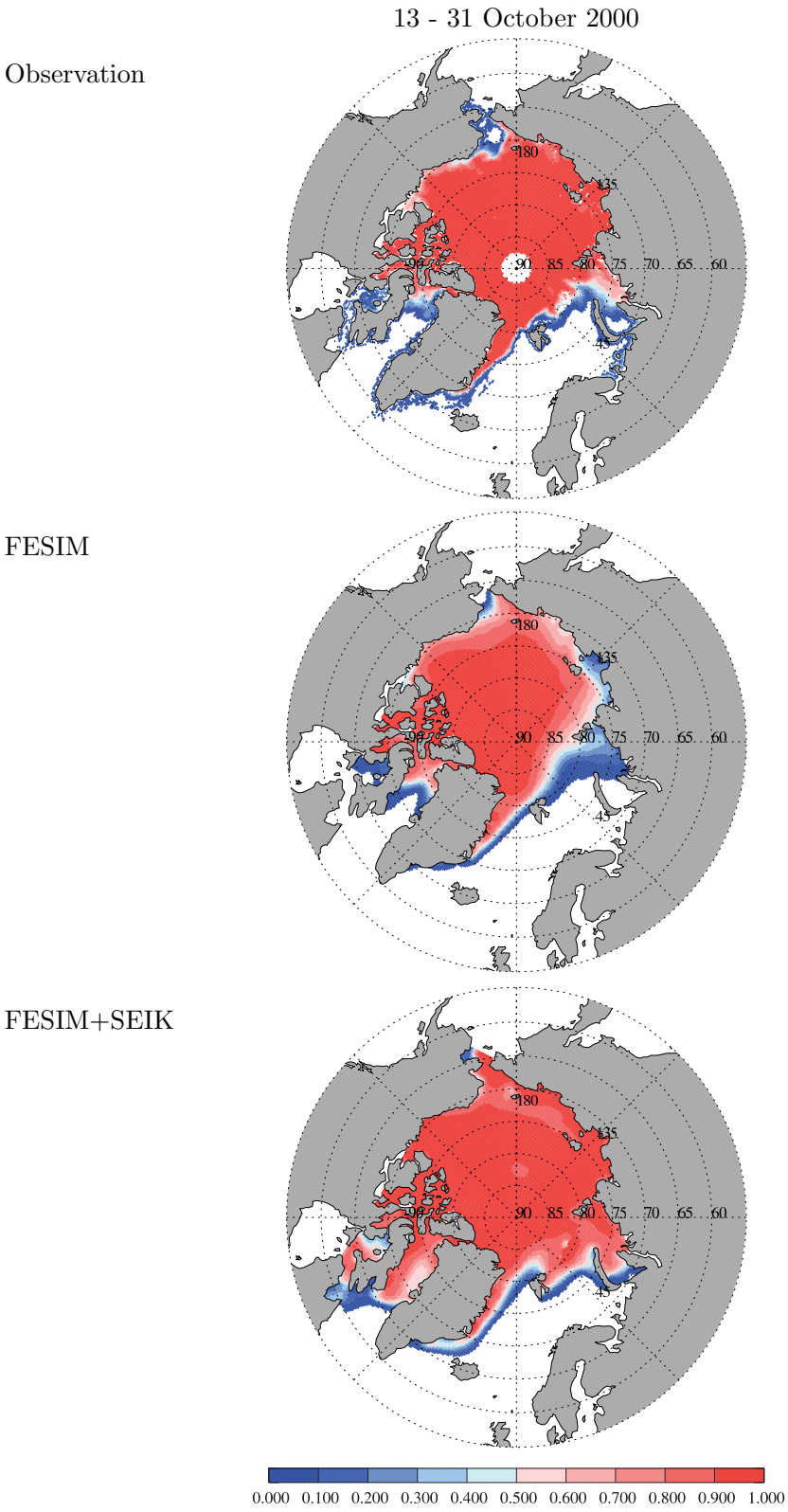

Figure 4.13: Sea-ice concentration maps 13-31 October 2000: Observation (top), model reference (center) and result from drift assimilation (bottom).

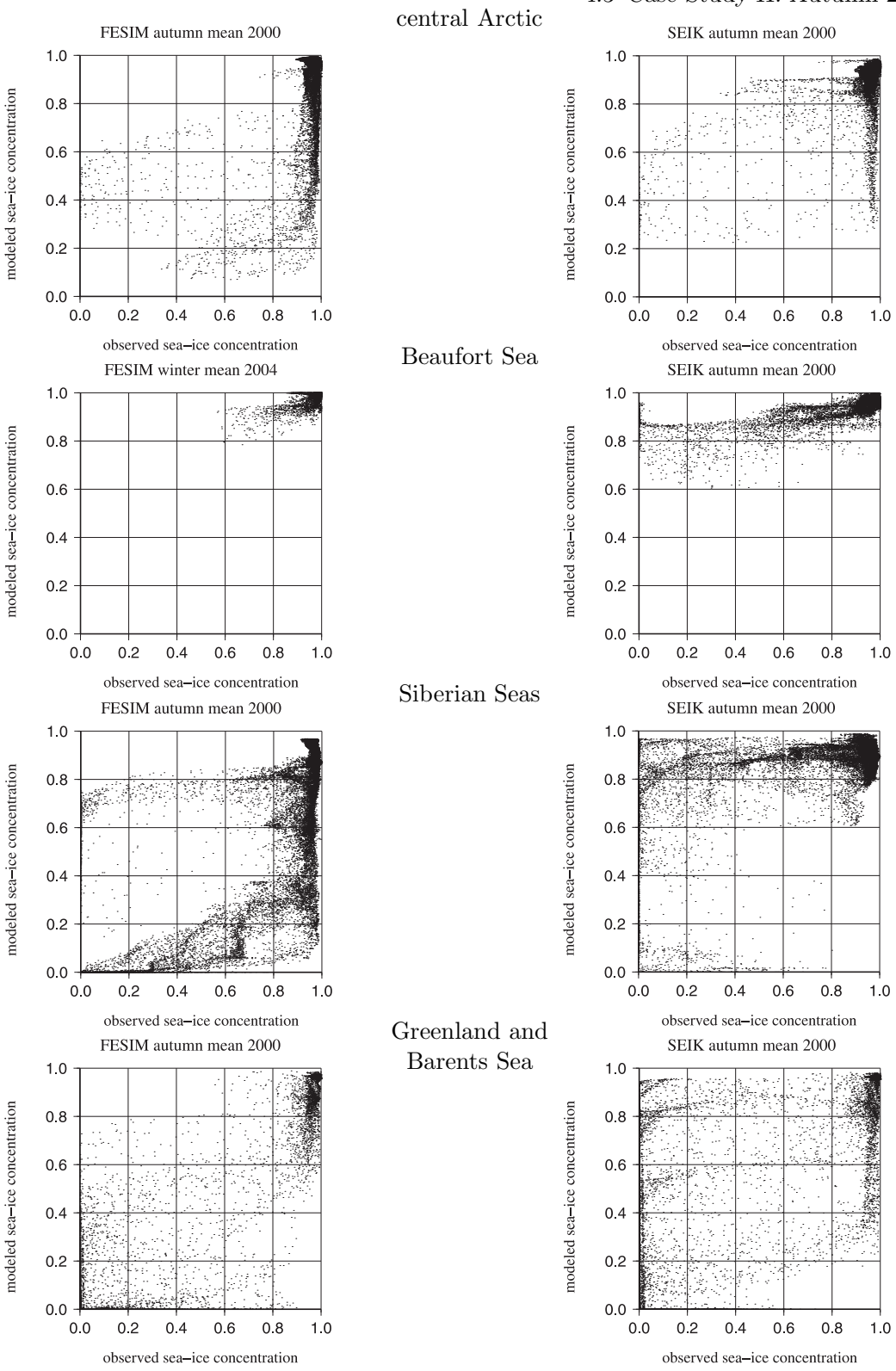

Figure 4.14: Modeled vs. observed sea-ice concentration data: mean for 13 - 31 October 2000; model reference (left), assimilation results (right). Data are split into four regions: Central Arctic (latitude $> 81°$ N), Beaufort Sea, Siberian Seas (including Chukchi, East Siberian, Laptev and Kara Sea), and Greenland and Barents Sea.

from the assimilation results for 13 - 31 October 2000. There are differences between the observed and simulated sea-ice concentration especially in the marginal ice zone (Figure 4.13). The reference simulation shows a good agreement in the Beaufort, Chukchi, and Greenland Seas but less in the East Siberian, Laptev, and Kara Seas. The assimilation obtains a more compact sea-ice cover in the Siberian Seas, but also in the Beaufort Sea. Additionally, sea ice is formed in the Baffin Bay in the assimilation that was not observed. These sea ice characteristics result from initial ensemble members which have already sea ice in the Baffin Bay in some cases. Thus, the overestimated sea-ice in the Baffin Bay is attributed to the statistical character of the data assimilation algorithm.

Scatterplots of simulated vs. observed sea-ice concentration (Figure 4.14) reveal the improvement due to assimilation of sea-ice drift in the central Arctic as well as in the Siberian Seas. The correlation between modeled/assimilated and observed sea-ice concentration in the central Arctic increases from 0.5 (without assimilation) to 0.6 (with assimilation). Additionally, the rms error is decreased from 0.18 (without assimilation) to 0.10 (with assimilation) here. Although the correlation coefficient for the sea-ice concentration in the Siberian Seas is decreased from 0.7 (without assimilation) to 0.6 (with assimilation) the rms error is decreased from 0.31 (without assimilation) to 0.26 (with assimilation). Here, the scatterplots also show a significant reduction of open water in the assimilation (Figure 4.14, third panel); but a slight overestimation of concentration arises which is mainly located in the Chukchi and Kara Sea. Thus, the sea-ice concentration in the Siberian Seas are slightly better represented by the assimilation.

The sea-ice concentration representation in the Beaufort Sea is better simulated in the reference run and the overestimation is slightly intensified with the assimilation procedure whereby this affects only a small part of the area. Here, the correlation coefficient is decreased from 0.8 (without assimilation) to 0.6 (with assimilation) and the rms error is increased from 0.12 (without assimilation) to 0.28 (with assimilation). Assimilation effects on the Greenland and Barents Seas sea-ice concentration seem to be rather small (Figure 4.14), but the sea-ice concentration maps show that a shift of the sea-ice edge is caused by the assimilation. However, as in the Beaufort Sea the correlation is decreased from 0.8 (without assimilation) to 0.6 (with assimilation) and the rms error is increased from 0.14 (without assimilation) to 0.24 (with assimilation).

However, it was not expected to improve sea-ice concentration representation on the marginal seas or at the sea-ice edge, because there are sparse sea-ice drift observations and weaker or even no correlations between sea-ice drift and concentration and thickness which leads to the inability to modify sea-ice state in that region with the presented SEIK Filter setup. An additional assimilation of sea-ice concentration might improve the concentration representation in these regions rather than the drift assimilation. Also a simultaneous assimilation of sea-ice drift and concentration with the SEIK Filter would be worth to analyze.

Sea-Ice Thickness

The modification of sea-ice thickness due to drift assimilation is substantial. The sea-ice thickness pattern differs considerably from the reference simulation (Figure 4.15).

13 - 31 October 2000

FESIM

FESIM+SEIK

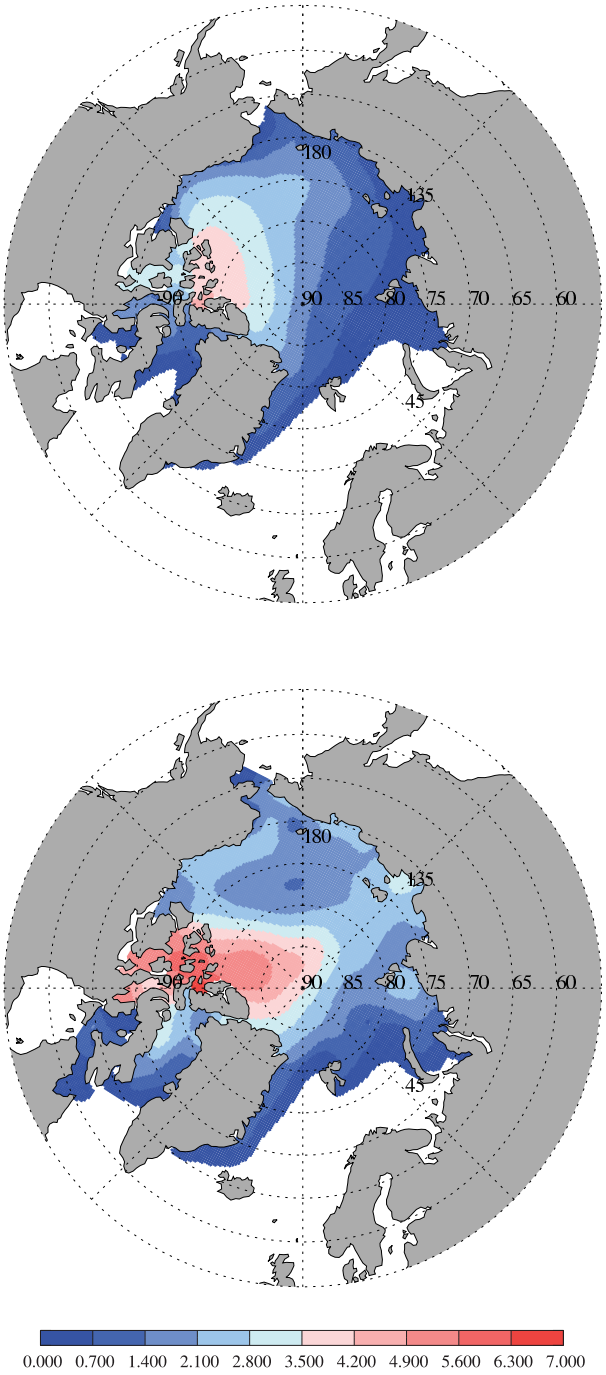

Figure 4.15: Mean sea-ice thickness [m] from 13 - 31 October 2000: reference simulation (top) and results from assimilation (bottom).

13 - 31 October 2000

ULS observation

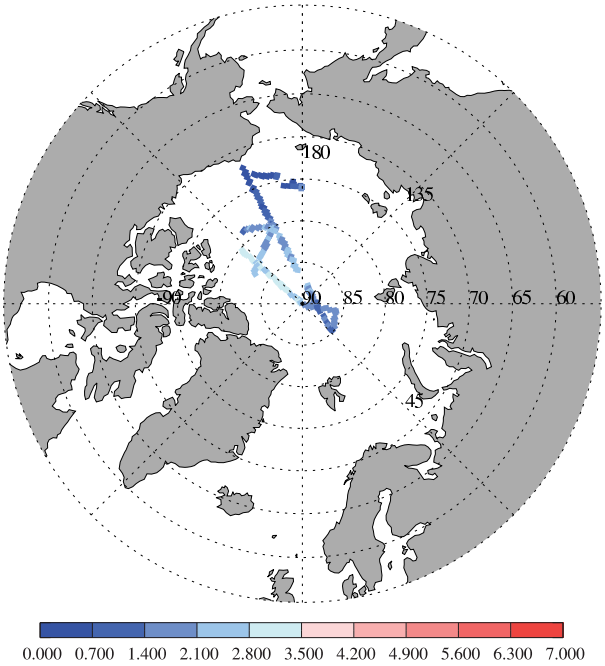

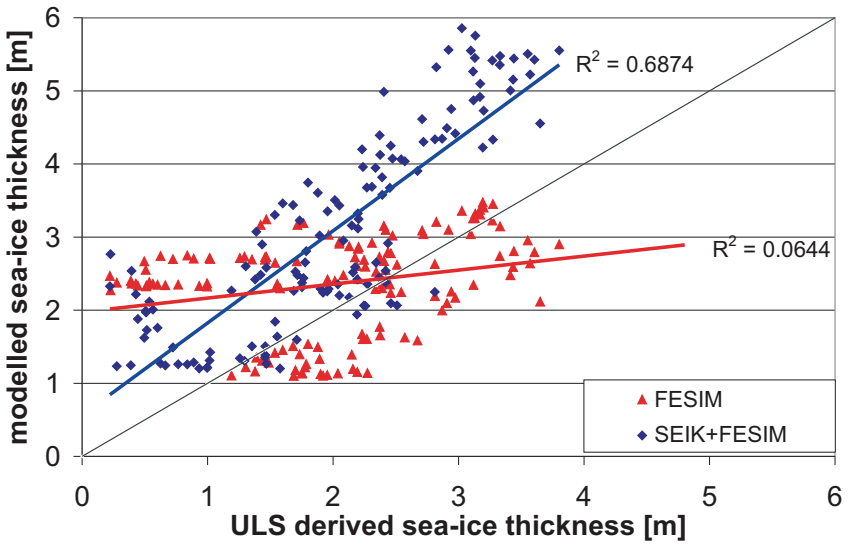

Figure 4.16: ULS derived sea-ice thickness [m] from 13-31 October 2000 (top) and scatter plot of modeled vs. observed sea-ice thickness with (blue diamonds) and without (red triangles) assimilation (bottom).

Thus, the ULS derived sea-ice thickness data (Figure 4.16, top) are utilized to validate the thickness distribution for October 2000 (Figure 4.15, bottom). It is obvious that the model was not able to produce the observed values without assimilation. The observation data cover partly the central Arctic that had been recorded from 13 - 31 October 2000. The data capture thicknesses from several centimeters up to 4 m. Neither the reference simulation nor the assimilation have been able to produce sea-ice thickness below 1 m. Both overestimate the observed thin ice in western Beaufort Sea whereby the assimilation for this thin ice produce a more representative thickness of 1 - 2 m than the reference simulation with 2 - 3 m.

The most visible difference lies in the large-scale pattern of the simulated sea-ice thicknesses (Figure 4.15). In the assimilation run the thickest sea ice stretches from North-Canada towards the pole and for the reference simulation it reaches towards the Beaufort Sea. The assimilation result shows a pattern similar to the long-term mean autumn map of *Bourke and Garrett* (1987). The thickest sea-ice is observed near to the pole (area north of 85° N) and coincides with the thickest sea ice in the assimilation which is not the case for the reference run, where the thickest sea ice occurs south of 85°N near the Canadian Archipelago.

The scatter plot reveals that the model alone is not able to represent the large variability of the observed sea-ice thickness (Figure 4.16, red triangles). Neglecting the overestimation of total sea-ice thickness the assimilation is able to produce a similar thickness variability as the observation suggests (Figure 4.16, blue diamonds). The least squares regressions reveal that the slope for the assimilation is close to 1, namely 1.26, which would represent a perfect coincidence of simulation and observation ± a constant. The slope for the reference run is merely 0.19 which underlines the small thickness range the reference simulation captures. Also the R^2, the squared correlation coefficient, suggest a better agreement of the assimilation results ($R^2 = 0.69$) with observations than the reference simulation ($R^2 = 0.06$). On the other hand, the assimilation overestimates thickness almost everywhere which is not true for the reference.

However, the crucial point is that the areas of thin and thick ice now better agree with observed thicknesses which demonstrates the high R^2, while the thinner and thicker ice of the reference result is arbitrarily distributed over the observed thickness range. That leads to the conclusion that the sea-ice thickness pattern is better represented after the assimilation than in the reference simulation. The overestimation of sea-ice thickness as well as overestimated sea-ice extent after the assimilation seems to be a consistent feature. The assimilation procedure produces more compact ice conditions which are amplified by the model ensemble integration.

4.3.2 Sea-Ice Thickness Variability Analysis

Within the assimilation from 1 October - 9 December a significant change occurred in the sea-ice thickness pattern (Figure 4.22). The sea-ice thickness changed from the summer pattern to the winter pattern similar to that of *Bourke and Garrett* (1987). To analyze this issue the sea level pressure (SLP) from NCEP/NCAR reanalysis data (*Kistler et al.*, 2001) were examined with regard to the large scale weather pattern

(Figure 4.17). The period is split into three phases: 13 October -18 November 2000 (autumn), 19 - 27 November 2000 (transition) and 28 November - 9 December 2000 (winter).

A wide anticyclone was located over the Laptev Sea during the first phase (Figure 4.17, top). This causes a weak Transpolar Drift Stream (TDS) and a Gyre with pronounced drift out of the Beaufort and Chukchi Seas to the East Siberian Sea and weak recirculation such that sea ice is transported towards the East Siberian coast. Such a drift results in a thinning of sea ice in the Beaufort and Chukchi Seas because leads and open water are formed in these regions. The open water areas refreeze so that new thinner ice is produced. The small drift north of Greenland and near the pole (Figure 4.18, top) indicates a compact thick ice mass resisting the air drag so that the ice is not moving.

During the second phase the anticyclone moved over the East Siberian Sea and a cyclone was located over the Laptev and Kara Seas (Figure 4.17, center). The increased drift out of the Laptev Sea results in polynyas and open water areas which again can refreeze and produce new ice. This has also the consequence that the ice coming out of the Laptev Sea is piled up if it is moving towards the pole where only small or no drift is dominant.

A strong anticyclone is located over the Arctic Basin in the last phase (Figure 4.17, bottom). This leads to strong drift in the Beaufort, Chukchi and East Siberian Seas as well as a pronounced TDS towards the northern coast of Greenland and Fram Strait (Figure 4.18). This strong drift causes divergence of sea ice along the TDS. The ice is not advected by a continuous long distance transport but rather intense small scale events of lead opening and deformation like rafting and ridging. The strong drift leads to a pronounced export through the Fram Strait. These processes cause a thinning across the TDS area. Since there is no drift along the coast of North-Greenland and the Canadian Archipelago no recirculation of sea ice occurs in the southern Beaufort Sea and the strong drift out of this sea might lead to unfasten of sea ice diverging towards the Chukchi Sea.

The drift comparison of reference simulation and assimilation results reveals higher velocities in both cases than the observed velocities during the first period whereby the assimilation leads to a slightly reduced velocity. The amazing point is that the different sea-ice thickness patterns (Figure 4.21 and 4.22, top) result in the same or very similar drift pattern. This is due to the different sea-ice concentration in the Chukchi Sea (Figure 4.13). Thicker ice (reference simulation) drifts faster because of the less compact conditions, and the thinner ice (assimilation results) together with a more compact sea-ice cover result in a similar drift.

At the end of November the reference simulation seems to result in a drift which is more reliable than the assimilation especially where the observed sea-ice drift out of the Laptev Sea is not reproduced by the assimilation procedure (Figure 4.19 and 4.20, center). However, the sea-ice drift in the Chukchi Sea is reduced by the assimilation. Here, the thickness patterns are very similar but the assimilation produces thicker ice near the Canadian Archipelago (Figure 4.21 and 4.22, center). In the Laptev Sea the sea ice from the assimilation run is 1 m thicker than in the reference experiment and the more compact ice conditions prevent the export toward the central Arctic.

At the beginning of December the assimilation produces a very good sea-ice drift agreement with the observations in contrast to the reference drift. Here, a recirculation of sea ice along the northern Greenland and Canadian coast, as simulated in the reference run, was not observed. Although both thickness distributions (Figure 4.21 and 4.22 , bottom) correspond to a winter thickness pattern they show extremely different sea-ice drift behavior in these regions. The reduced drift is due to the larger sea-ice thickness at the Canadian coast produced by the assimilation procedure which result in a higher ice strength resisting the air and ocean drags.

The sea-ice thickness changes resulting from the drift assimilation suggest a higher temporal thickness variability which is a result of the statistical modification of sea-ice mass introduced by the SEIK analysis. However, the thickness variability within the seasons can be explained by dynamical and thermodynamical processes. The thickness pattern in summer and autumn can be explained with persistent multi-year sea ice near the pole and thin ice or no sea ice due to melting in the marginal seas. These features are also prevalent in the sea-ice thickness data from *Rothrock et al.* (2003) where the thickest sea-ice occurs between Greenland and the North Pole in summer as well as in winter. The thermodynamic and dynamic sea-ice thinning in the coastal regions of the Beaufort Sea seems to be underestimated by the sea-ice model and sea ice remains in this region, which results in a simulation with thicker sea-ice and higher concentration. The underestimation of open water areas leads to an underestimation of thin newly formed sea ice which would result in a thinner mean sea-ice thickness in autumn. The transition to the winter distribution can be explained with extreme refreezing during autumn in the marginal seas which produces new sea ice. The TDS transports sea-ice towards Fram Strait which leads to thinning of the thick multi-year sea-ice at the pole. The new sea ice in the Beaufort Sea can be deformed more easily and can accumulate.

It is still difficult to conclude if the simulated sea-ice thickness change is more realistic than the more homogeneous sea-ice thickness pattern of the reference simulation. In summary, the assimilation derived thickness pattern in October has been positively validated with thickness observations and the assimilation derived sea-ice drift at the beginning of December agrees very well with the drift observations. Therefore the thickness patterns in both periods represent a realistic Arctic sea-ice state.

4.4 Ensemble Variability

In this section the ensemble variability, predicted with the SEIK Filter, is analyzed. The ensemble covariance matrix is used to determine the weights (Equation (2.119)) for the analysis update, which modifies the analysis state such that it is located between forecast and observation state, because both states, forecast and observation, are considered to be two possible realizations of the sea-ice state. The purpose is to obtain a adequate forecast variance to determine a weight which is mainly determined by the difference between observation and forecast because for small ensemble covariances the forecasted state is given more weight than the observation. In the following, the SEIK error estimation is discussed and then the option of the SEIK Filter with a fixed error base is presented.

13 October - 18 November 2000

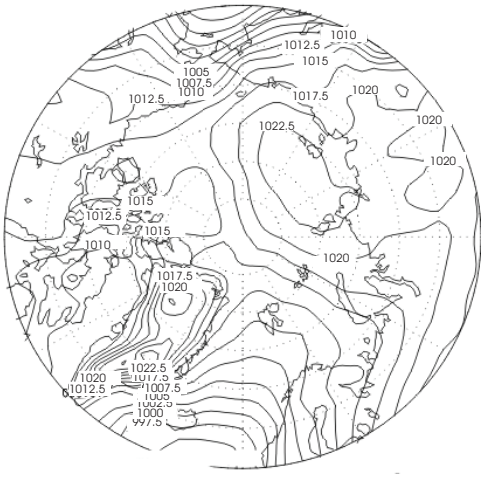

19 November - 27 November 2000

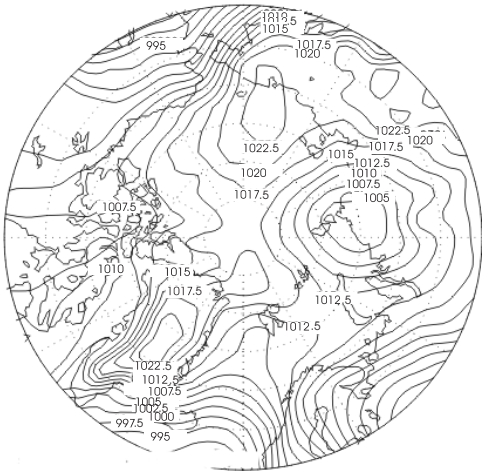

28 November - 9 December 2000

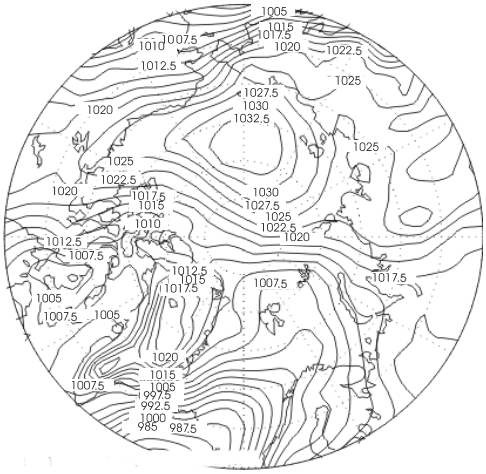

Figure 4.17: Mean sea level pressure [hPa] from NCEP/NCAR reanalysis for autumn 2000.

Observation

13 October - 18 November 2000

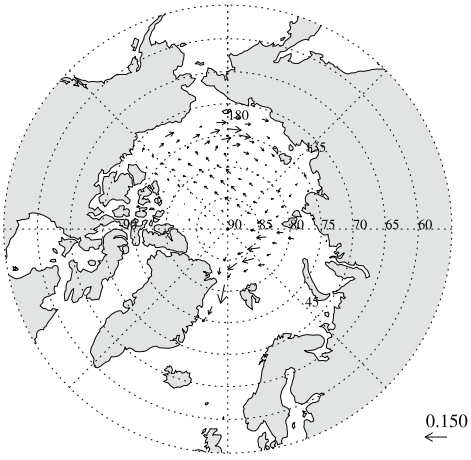

19 November - 27 November 2000

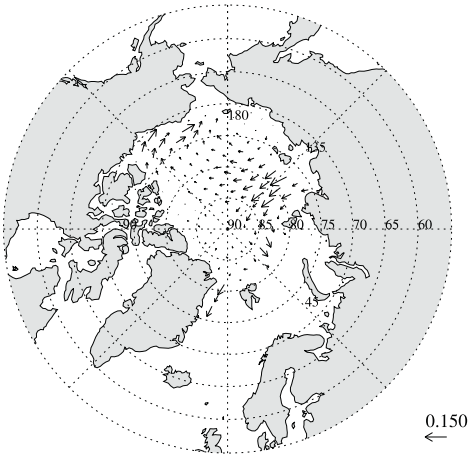

28 November - 9 December 2000

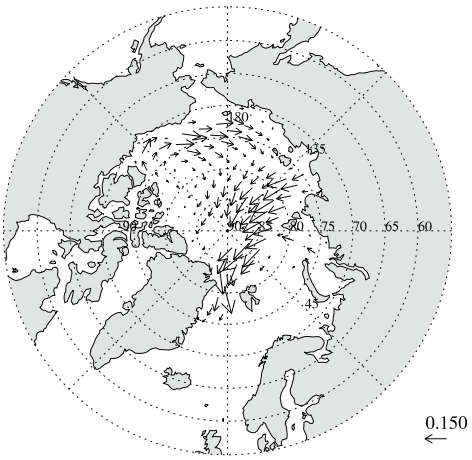

Figure 4.18: Observed mean sea-ice drift vectors [$\mathrm{m\,s^{-1}}$] for autumn 2000.

FESIM

13 October - 18 November 2000

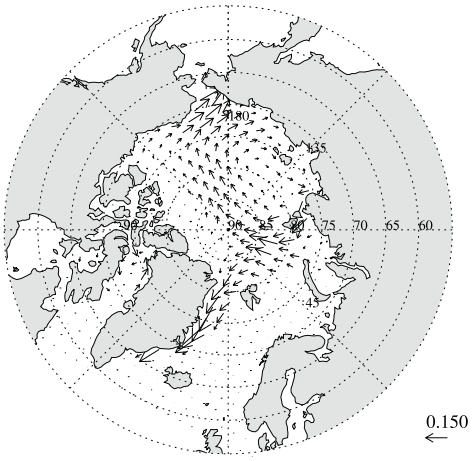

19 November - 27 November 2000

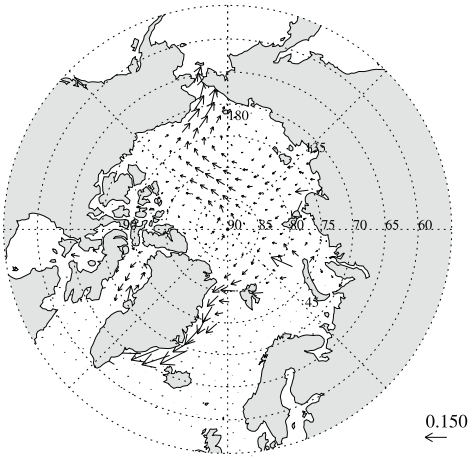

28 November - 9 December 2000

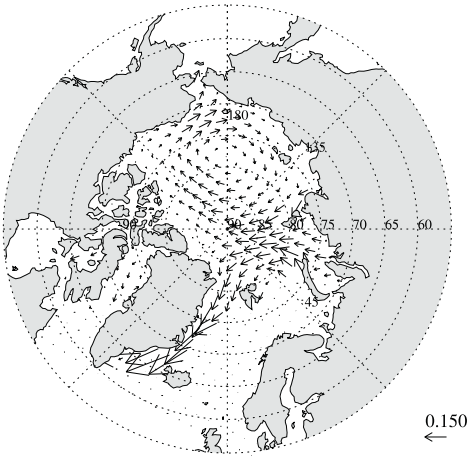

Figure 4.19: Reference simulation of mean sea-ice drift vectors [$\mathrm{m\,s^{-1}}$] for autumn 2000.

FESIM+SEIK

13 October - 18 November 2000

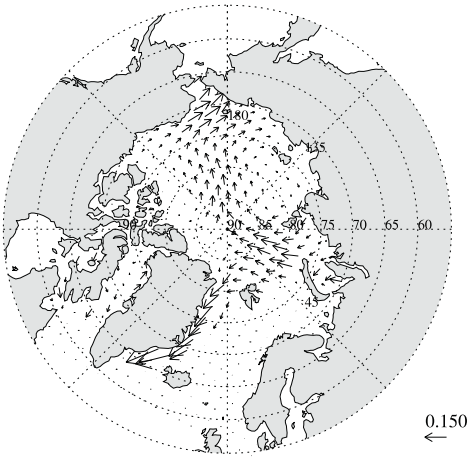

19 November - 27 November 2000

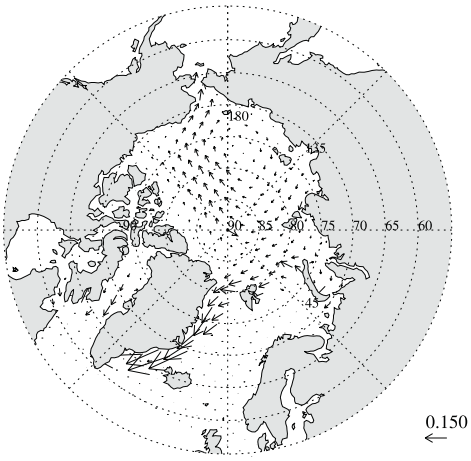

28 November - 9 December 2000

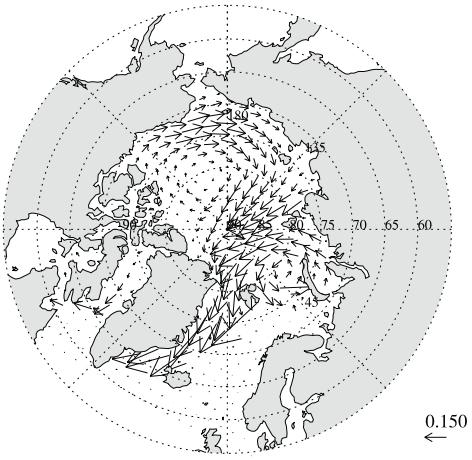

Figure 4.20: Assimilation results of mean sea-ice drift vectors [$\mathrm{m\,s^{-1}}$] for autumn 2000.

FESIM

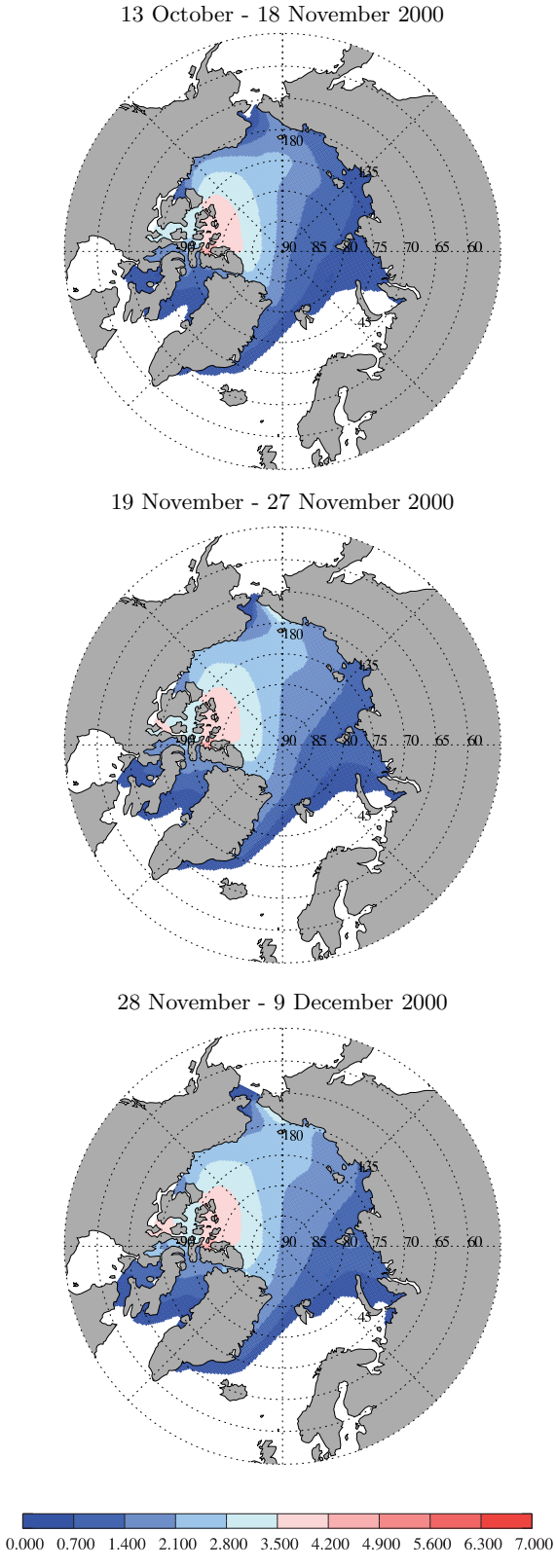

Figure 4.21: Reference simulation of mean sea-ice thickness [m] for autumn 2000.

FESIM+SEIK

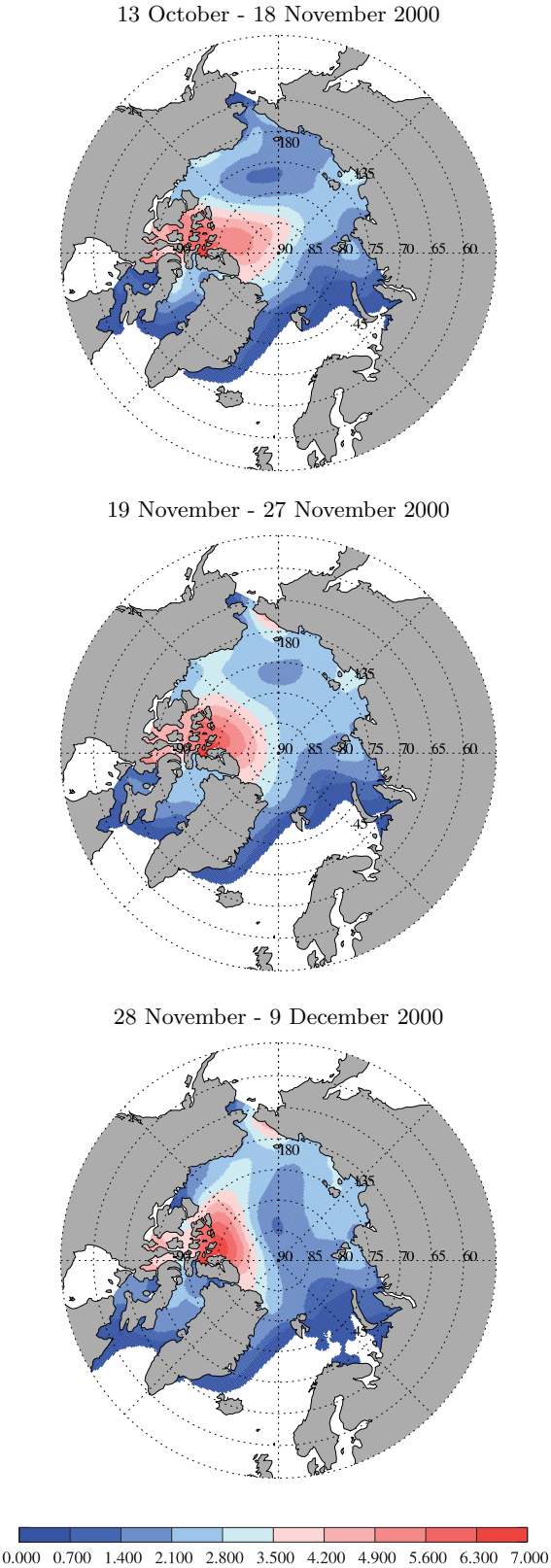

Figure 4.22: Assimilation derived mean sea-ice thickness [m] for autumn 2000.

4.4.1 SEIK Error Estimation

The data assimilation results from winter 2004 are selected to examine the SEIK error estimation. The simulation starts on 1 January and ends on 30 May 2004. However, the active assimilation lasts only until 30 April 2004 because sea-ice drift observations are not available for summer months (*Ezraty and Piollé*, 2004a). The computation was continued until the end of May because HEM sea-ice thickness measurements are available on 12 and 13 May 2004 in the Lincoln Sea. They are used to evaluate the SEIK Filter sea ice thickness estimate.

Since the covariance matrices $\mathbf{P}^f$ and $\mathbf{P}^a$ are not explicitly computed in the SEIK Filter algorithm, the corresponding variance is determined from the model ensemble. The standard deviation prediction by the SEIK Filter exhibits a transient response within the first few assimilation steps where the initial, overestimated error covariance is reduced after two to four assimilation steps (Figure 4.23), which consequently decreases the ensemble variability.

The SEIK Filter error estimation reveals a standard deviation for the sea ice velocity components that increases slightly and fluctuates within 2 and 7 mm s^{-1} (Figure 4.23, top). The robust standard deviation in the sea-ice drift field demonstrates that the SEIK Filter is able to control the model sea-ice drift estimation with consistent quality. However, this does not automatically mean that the estimated sea-ice velocity is close to reality. This can only be checked with independent observations. Since the predicted standard deviation is less than 1 cm s^{-1} (Figure 4.23, top), the drift ensemble has a very small variability. This is due to the use of the same forcing and the same model physics throughout the ensemble. The sea-ice drift variations are obtained with different sea-ice thickness and concentration states according to the dependence of thickness and concentration on the ice strength and vice versa. Thus, the drift corrections from the SEIK Filter analysis are very small and a drift improvement is achieved mainly by thickness and concentration change in the course of several weeks of assimilation.

For sea-ice thickness and concentration (Figure 4.23, center), the error estimation in the sea-ice fields increases continuously. This reflects an increasing ensemble variance and that the approximated mean state gets more uncertain. This ensemble spread increase is not an indication that the mean state deviates more strongly from the "true state". The predicted ensemble standard deviation in the sea-ice concentration field increases from less than 1 % to about 3 % which is still smaller than the estimated observation error of satellite derived sea-ice concentration (*Comiso et al.*, 1997). The simulated mean sea-ice concentration remains close to the observed sea-ice concentration.

The sea-ice thickness standard deviation is also in a small range of less than 0.6 m but the comparison with ULS and HEM observation data shows a significant overestimation of approximately 1 m (autumn 2000) and 3 m (spring 2004). However, the spatial variability and trends of the sea-ice thickness have been shown to be in a good agreement with the observations (Figure 4.16, Table 4.1). After a few assimilation steps the ensemble variance decreases to a minimum and then increases continuously with ongoing assimilation. The significant overestimation of sea-ice thickness is not directly correlated with the predicted standard deviation. Thus the predicted ensemble standard deviation

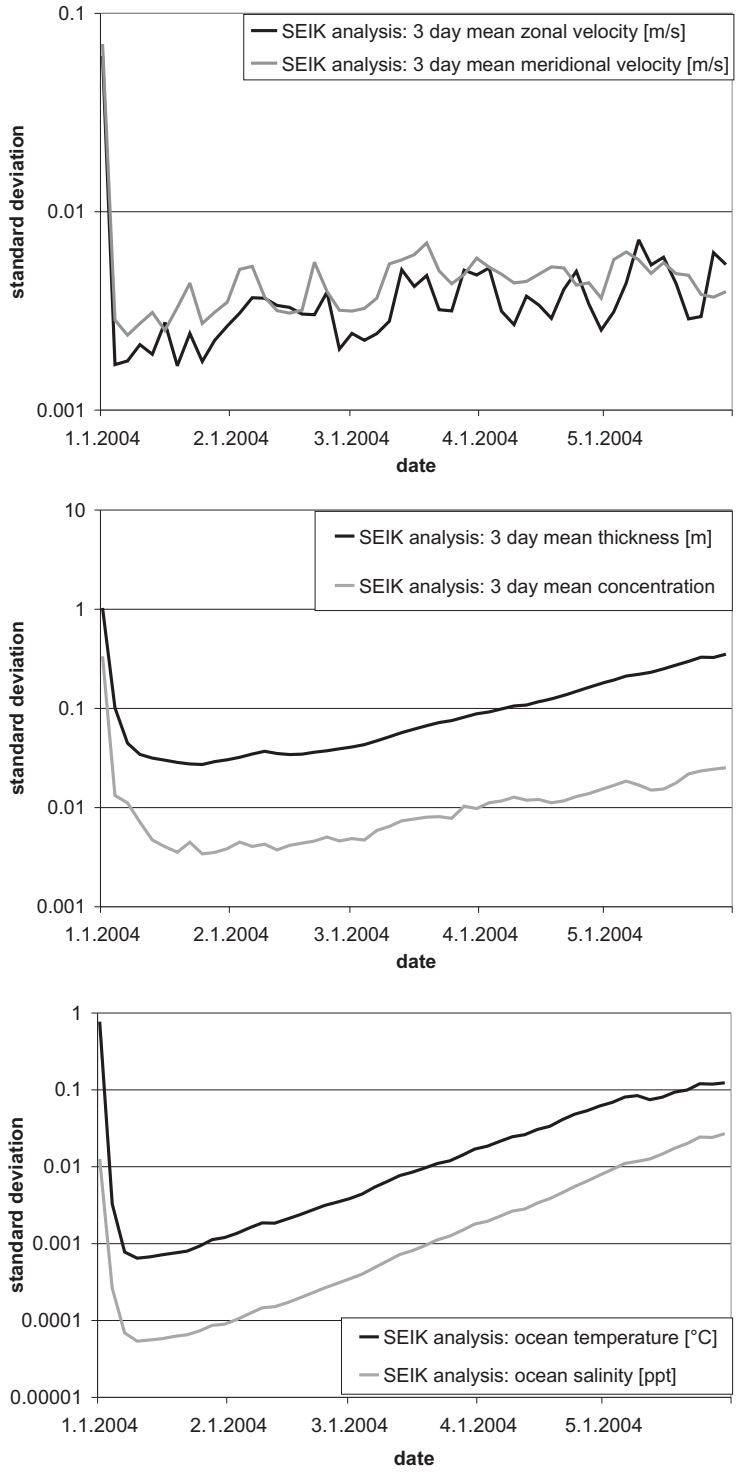

Figure 4.23: SEIK analysis estimate of the spatially averaged standard deviation of zonal and meridional sea-ice velocity (top), sea-ice thickness and concentration (center), and the ocean temperature and salinity (bottom) from 1 January to 30 May 2004.

is not a suitable quality criterion for the sea-ice thickness estimation.

For the ocean temperature and salinity the error estimate increases with ongoing assimilation. Not surprisingly, the sea-ice drift assimilation procedure is not able to control these fields sufficiently. From the physical point of view the temperature and salinity have no direct connection to the drift, so that correlations are small. They are connected to the model thermodynamics and rather correlated to the thickness and concentration, and so indirectly to the drift. Nevertheless, the standard deviation of these fields is still below 0.2° C and 0.05 ppt for temperature and salinity, respectively, at the end of the simulation (Figure 4.23, bottom).

On a local scale, the ensemble standard deviation exceeds 1.0 $\mathrm{cm\,s^{-1}}$ (Figure 4.24) which is less than the approximated observation error of 1.6 $\mathrm{cm\,s^{-1}}$. The sea ice drift has a high spatial and temporal variability (Figure 4.25). The temporal variability is related to the high atmospheric variability; the spatial variability corresponds to the large scale atmospheric circulation pattern. The ensemble drift variance partly depends on atmospheric conditions. Strong winds produce locally larger variances of the sea-ice variables than weak winds. Then larger modifications of the sea ice drift can be derived by the SEIK Filter analysis (section 4.2.1), which also holds for the thickness for compact ice conditions when the correlation between drift and thickness is distinct.

The highest standard deviation of the sea-ice velocity is located at the sea-ice edge where free sea-ice drift occurs. This coincides with the highest standard deviation of sea-ice concentration and the lowest standard deviation of the sea-ice thickness which are also found at the sea-ice edge. For free drift, the correlation between sea-ice thickness and drift is very small.

When a forgetting factor of 0.8 is applied to increase the variance in the SEIK Filter algorithm, the drift analysis still maintains an rms error which is larger than the observational error. An assimilation with a forgetting factor of 0.5 results in an unrealistic sea-ice state, that features mean thicknesses larger than 10 m north of Greenland followed by a large polynya in the same region. None of these appear in the observations. Such fluctuations are clearly unrealistic.

Ways to increase the ensemble variance are perturbations in the wind forcing or an inclusion of a varying air drag coefficient into the model state vector. This coefficient has a large influence on the drift because it determines the momentum transfer from the atmosphere to the sea ice. To vary this parameter, maybe even as a parameter field, is expected to lead to an increased drift variance and the SEIK Filter has another possibility to reduce or enhance the sea-ice drift significantly. The drift update in the marginal ice zone is then expected to be improved considerably with such a set-up. A side-effect might be a temporal and spatial variability of the drag coefficient which leads to conclusions about the variability of sea ice roughness and to an improved knowledge of this parameter.

To summarize, the SEIK Filter is able to provide an error approximation with consistent quality for the observed field while it is accepting an increasing variance in the other fields with no observation information. The presented SEIK Filter setup produces a small drift variance with little direct drift corrections. Small drift modifications are correlated with significant sea-ice concentration and thickness changes. These changes

FESIM+SEIK

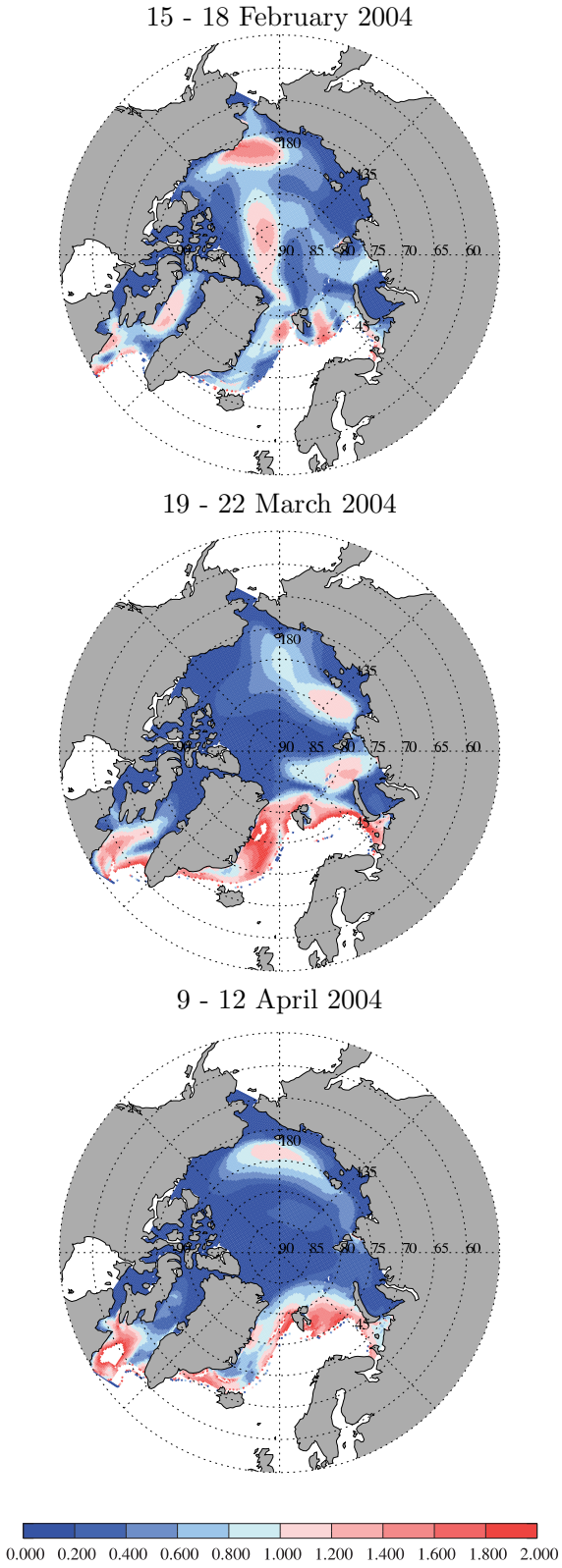

Figure 4.24: Three day mean sea-ice velocity ensemble standard deviation [cm s^{-1}]: 15 - 18 February (top), 19 - 22 March (center), and 9 - 12 April 2004 (bottom).

FESIM+SEIK

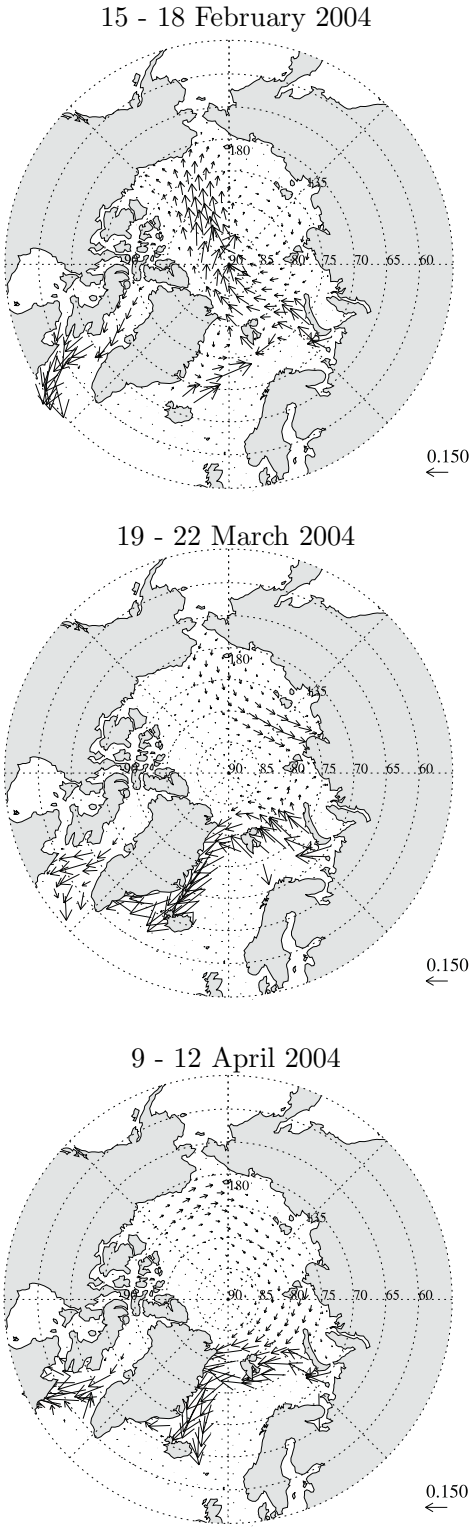

Figure 4.25: Three day mean sea-ice drift vectors [$\mathrm{m\,s^{-1}}$]: 15 - 18 February (top), 19 - 22 March (center), and 9 - 12 April 2004 (bottom). The larger the sea-ice velocities the larger is the ensemble standard deviation (cf. Figure 4.24).

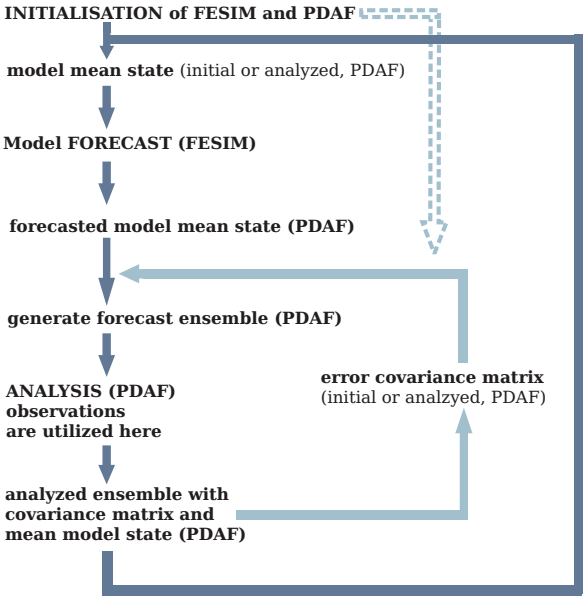

Figure 4.26: Assimilation scheme of the SEIK Filter with fixed error basis.

lead to an improved drift with ongoing assimilation. A higher variability of sea-ice drift is expected to be obtained with a perturbed forcing, different model physics for separate ensemble members or an additional assumed system noise $\mathbf{Q}$ as is intended in the theoretical SEIK Filter algorithm.

4.4.2 SEIK Filter with Fixed Error Basis

In a sensitivity experiment the SEIK Filter is applied with a fixed error basis (from now on referred as FSEIK). Here, the initialization is similar to the SEIK Filter but only the mean state is evolved with the model. The initial covariance matrix and the forecasted mean state are used to approximate an artificial ensemble which follows the analysis as for the conventional SEIK Filter but the computation of $\mathbf{U}_k^{-1}$ (Equation (2.122)) is done with fixed ensemble residuals ($\mathbf{L}_k$) and the Kalman gain matrix $\mathbf{K}_k$ (Equation (2.118)) is computed with this updated $\mathbf{U}_k$ matrix. Then the analysis provides the updated mean state and the updated covariance matrix. For the next assimilation step the previous updated mean state is forecasted only and the previous updated covariance matrix are used to approximate the artificial ensemble for the next analysis phase and so on (Figure 4.26). Actually, the residuals ($\mathbf{L}_k = \mathbf{X}_k\mathbf{T} = (\overline{\mathbf{x}}_k - \mathbf{x}_k^{(1)}, ..., \overline{\mathbf{x}}_k - \mathbf{x}_k^{(r)})$) are fixed in the SEIK Filter equations (Equation (2.115)-(2.118)). The residuals are modified in course of the re-initialization (Equation (2.121)) which corresponds to the updated covariance (Equation (2.120)).

Using the FSEIK with the initial covariance matrix, derived from monthly mean states yields highly overestimated thickness changes. These lead to a massive increase of ice

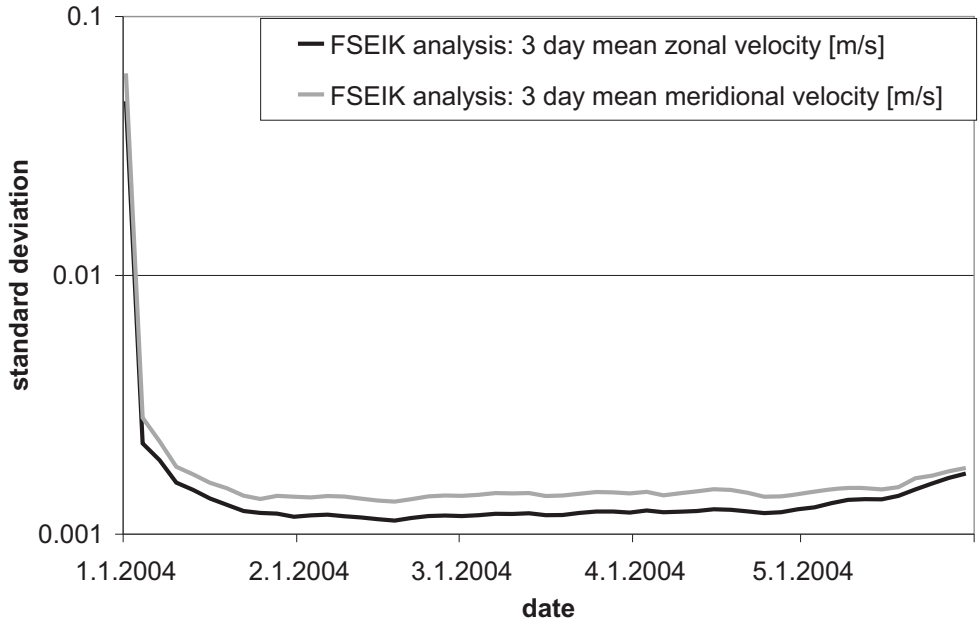

Figure 4.27: Estimated standard deviation of sea-ice velocity by the SEIK analysis with fixed error basis.

volume in the Siberian Seas with more than 4 m thickness and thinner ice at the Canadian and Alaskan coasts of less than 2 m which is clearly unrealistic.

Therefore the initial covariance matrix has to be determined more carefully for the FSEIK setup. While sea-ice velocity covariances are similar for different time scales, the covariance between drift and thickness anomalies increases considerably with the time scale. These dependencies adjust automatically in the full SEIK Filter setup by the ensemble forecast providing more accurate cross correlations between drift and thickness changes. Here, the initial covariance matrix for the FSEIK is estimated from model time series with the same time resolution of three days as is applied in the assimilation procedure.

The drift standard deviation which is derived from the ensemble statistics is decreased due to the FSEIK analysis (Figure 4.27) and the initial value of ≈ 6 cm s^{-1} is strongly reduced. From 1 February to 1 May 2004 the FSEIK obtains standard deviations less than 0.2 cm s^{-1} while the full SEIK obtains standard deviations between 0.2 cm s^{-1} and 0.7 cm s^{-1}. Thus, the model (without additional perturbations) is able to increase the forecast error estimation, based on the computed ensemble, but the deviation is not sufficiently large or comparable to the determined observation error of approximately 1.6 cm s^{-1}.

A test with the FSEIK setup with an increased observation error (≈ 6.4 cm s^{-1}) reveals that the updated drift standard deviation is increased (Figure 4.28). Here, the standard

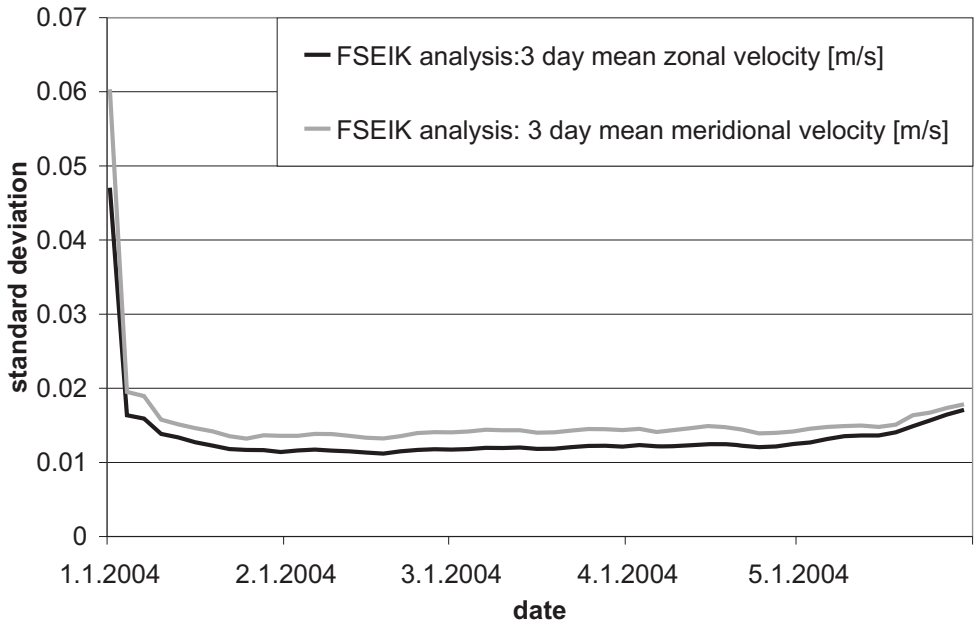

Figure 4.28: Estimated standard deviation of sea-ice velocity by the SEIK analysis with fixed error basis and increased observation error.

deviation from 1 February to 1 May 2004 obtains values greater than 1 $\mathrm{cm\,s^{-1}}$. This is a result of the larger observation error matrix $\mathbf{R}$ in Equation (2.122) that increases the matrix $\mathbf{U}$ which leads to an increased covariance estimation due to $\mathbf{P}^a = \mathbf{L}^{\mathrm{T}}\mathbf{UL}$. This does not automatically lead to a further drift improvement. Actually, the assimilated drift rms error (FSEIK with increased observation error) results almost in the same rms error as without an increased observation error (Figure 4.29). They are also similar to the results of the full SEIK Filter setup (Figure 4.23). This is due to the weights for the update of the mean state which is not much changed with an increased observation error because the enhancement in $\mathbf{U}$ is simultaneously reduced by the increase of $\mathbf{R}$ for the Kalman gain (Equation (2.118)).

This leads to the conclusion that a further improved drift analysis can be achieved with an enhanced ensemble covariance and not necessarily due to an increased observation error with a fixed error setup. This is not necessarily true for the full SEIK Filter setup where an increased observation error could lead to a wider ensemble spread due to the resampling which influences the ensemble forecast.

The sea-ice drift updates are similar for the conventional SEIK, the FSEIK, and the FSEIK with increased observation error setup (Figure 4.1 and 4.29) despite the different initialization covariance matrices for the SEIK and FSEIK. The spatial pattern of the sea-ice velocity for the FSEIK setup seems to resembles the reference simulation (Figure 4.30); the sea-ice concentration shows no large differences between the different

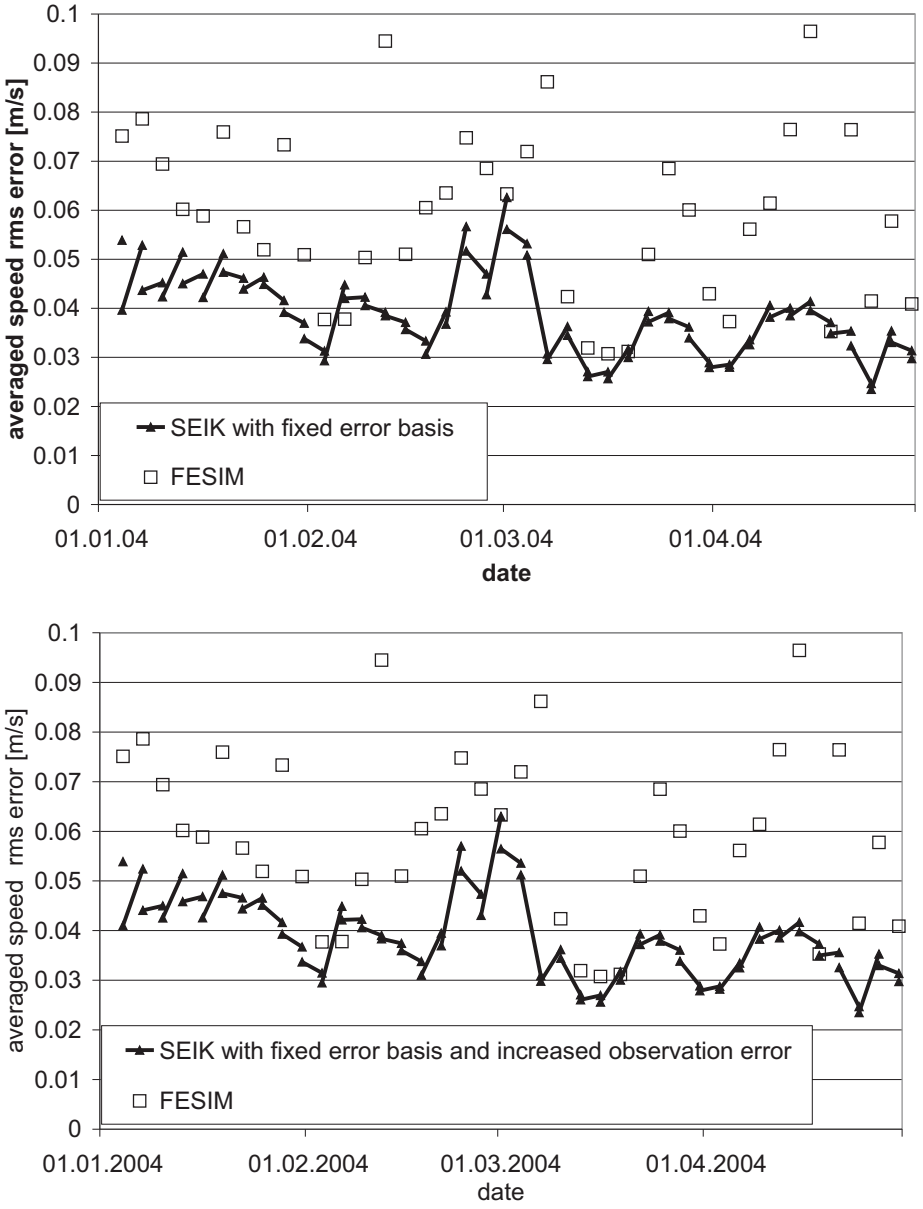

Figure 4.29: Spatial averaged rms error of satellite derived sea-ice speed: SEIK Filter with fixed error basis (top) and SEIK Filter with fixed error basis and increased observation error (bottom); SEIK Filter analysis drift correction is not affected by increased observation error.

FESIM

FESIM+SEIK

FESIM+
SEIK with fixed error basis

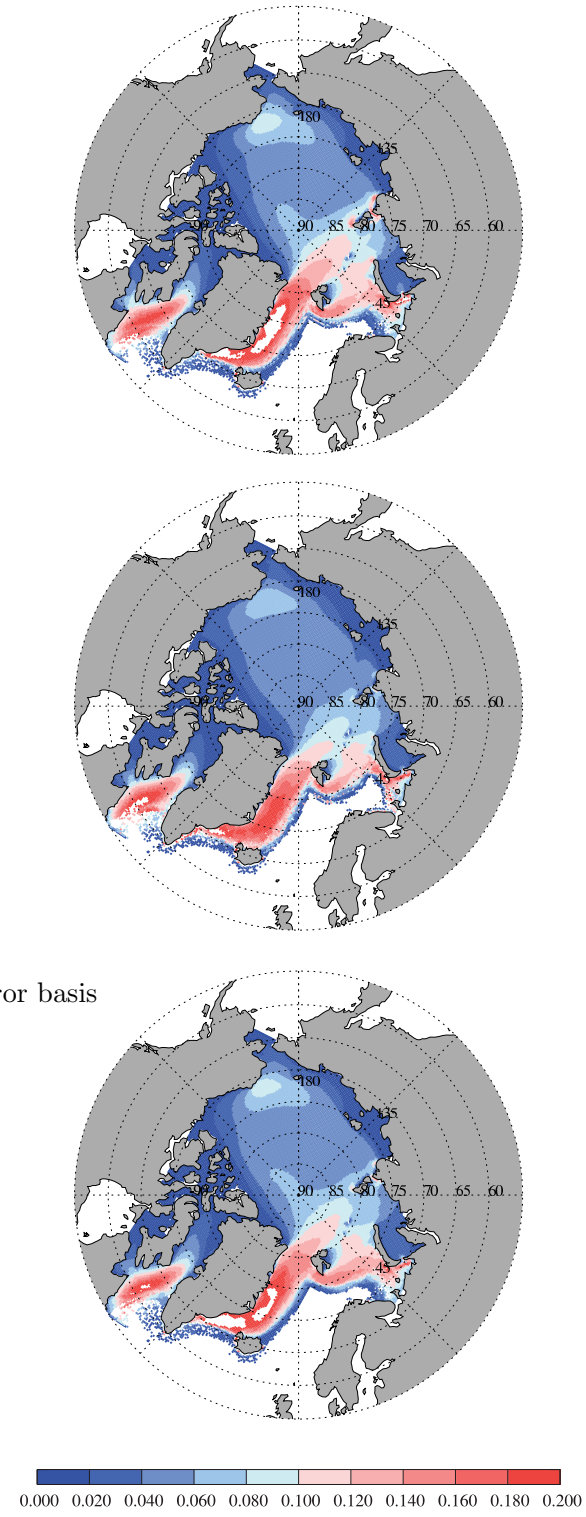

Figure 4.30: 1 January - 30 May 2004 mean sea-ice velocity [$\mathrm{m\,s^{-1}}$] from the reference simulation (top), assimilation (center) and fixed basis error set-up (bottom). Sea-ice velocities larger than 0.2 $\mathrm{m\,s^{-1}}$ are not shown (white patches near east Greenland coast).

FESIM

FESIM+SEIK

FESIM+
SEIK with fixed error basis

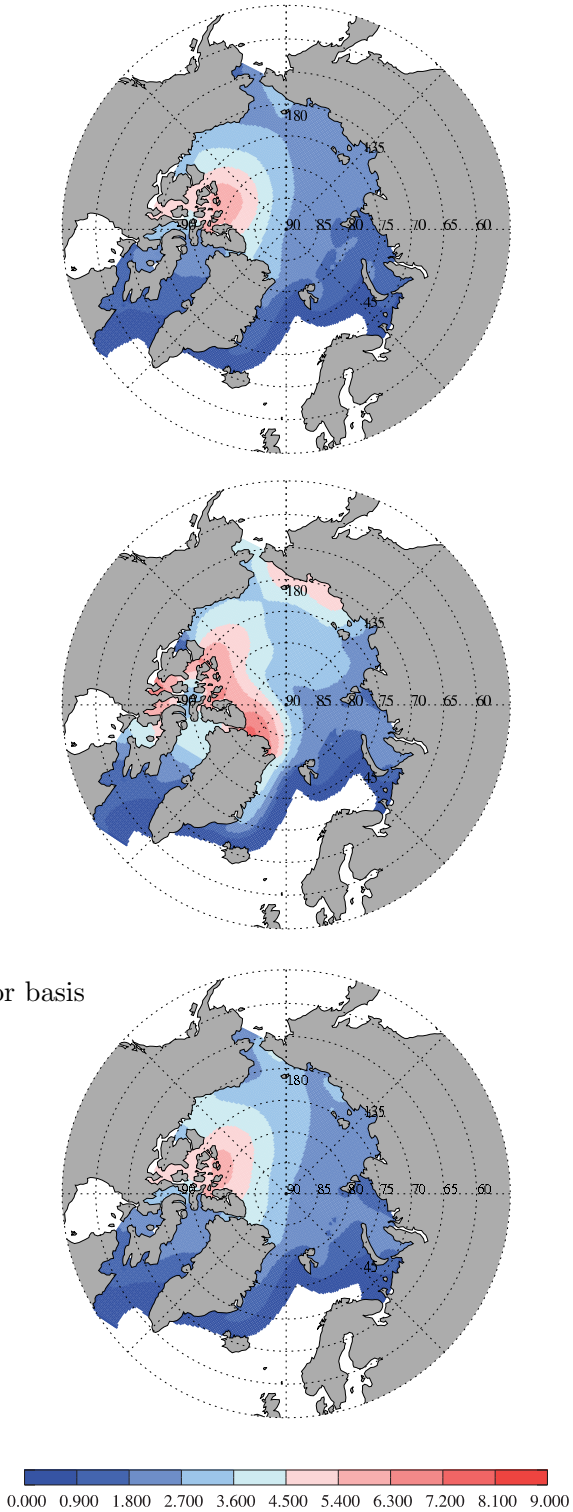

Figure 4.31: 1 January - 30 May 2004 mean sea-ice thickness [m] of reference simulation (top), assimilation (center) and fixed basis error set-up (bottom).

SEIK setups and the observations because this variable is already well estimated by the model reference simulation; the thickness changes are small and the sea-ice thickness distribution is more similar to the reference simulation (Figure 4.31).

4.5 Mass Conservation

The sea ice model variable h is defined as the mean ice thickness over the entire grid box presenting the ice volume per grid box area. To obtain the actual ice thickness $\hat{h}$ in the ice covered part of the grid box, h has to be divided by the sea-ice concentration A:

$$\hat{h} = \frac{h}{A}. \tag{4.2}$$

For the assimilation of ice concentration A, either the mean ice thickness h or the actual ice thickness $\hat{h}$ need to be adjusted, while the other can be preserved. *Lieser* (2004) mentions that sea-ice concentration assimilation affects the sea-ice volume due to the direct relation between concentration and mass (Equation (4.2)). There, the actual thickness $\hat{h}$ is fixed and the mean thickness h is subject to fluctuations. *Dulière and Fichefet* (2007) and (*Dulière*, 2007) find that for assimilation of sea-ice velocities and/or concentration a fixed actual sea-ice thickness $\hat{h}$ and a varying mean sea-ice thickness h provides best results.

The validation of sea-ice thickness in autumn 2000 and spring 2004 in our case has revealed that the sea-ice thickness is overestimated due to the assimilation procedure, but the assimilation results of 2000 covers the sea-ice thickness range similar to the ULS observations (section 4.3). The spatial large-scale sea-ice thickness pattern is also well simulated.

Clearly, the SEIK Filter analysis does not conserve the sea-ice volume. Sea-ice mass is added or removed in the analysis phase of the assimilation procedure. The Arctic-wide mean sea-ice increase caused by the assimilation procedure in 2004 is 5 cm on average within a single analysis step with a standard deviation of 13 cm. In the central Arctic (>81°N) the increase is 7 cm ± 15 cm. This increase is accumulated until mid of May when HEM sea-ice thickness data are available. The SEIK Filter caused an increase within this time, which is 245 cm ± 15 cm. This is close to the general overestimation of approximately 3 m for the assimilation results.

Similarly, the mean sea-ice thickness increase for an assimilation step in the simulation of autumn 2000 is approximately 2 cm ± 17 cm. In the Beaufort Sea area there is a sea-ice mass decrease which amounts to a few mm per analysis step with a standard deviation of 18 cm. The other areas show an increase between 2 - 3 cm. Regarding the central Arctic and Beaufort Sea areas, where the ULS derived thickness data are located, the SEIK Filter causes a sea-ice mass increase of 20 cm ± 22 cm for October 2000. The averaged sea-ice thickness overestimation of 1 m can not be explained with this mass increase, but it is obvious that the assimilation procedure modifies the ice volume budget quite heavily.

In a very simple experiment to test the sea-ice mass conservation, the SEIK Filter analysis was executed as usual and the derived mean thickness h change was converted

into a actual thickness $\hat{h}$ and concentration A modification and the sea-ice mass forecast is fixed due to the simple relation of Equation (4.2). This experiment resulted in unrealistic Arctic-wide sea-ice concentration conditions with less than 90% coverage in winter.

Of course, conserving sea-ice mass within the SEIK analysis and prescribing their covariances being zero would prevent sea-ice thickness modification. This, however, would be a step back, because the SEIK Filter has improved the sea-ice thickness pattern towards the observation, although with a systematic overestimation of the sea-ice thickness. It is probably more effective to include sparse thickness observations to constrain the filter's sea-ice thickness modification. It is not clear how the sea-ice drift will be affected with an additional sea-ice thickness assimilation.

4.6 Local SEIK Results

4.6.1 Local SEIK Analysis with Sea-Ice State Only

The local SEIK Filter (LSEIK) setup (section 2.2.3) is analyzed for the same time period in 2004 as for the SEIK Filter assimilation (Section 4.2). The LSEIK setup differs from the SEIK Filter in the analysis and resampling phases. The LSEIK analysis and re-initialization is done sequentially for the sea-ice state at each surface node if any observation is available within a 150 km radius. Otherwise no analysis is executed. The ocean ensemble states are not affected by the LSEIK analysis and only adjusted by the model during the forecast. The ensemble state standard deviation for the ocean temperature and salinity due to the ensemble integration amounts 0.02-0.08 °C and 0.0027-0.0069 ppt, respectively.

The LSEIK ensemble variance estimation of the non-observed fields increases significantly in course of the assimilation. This increase is primarily caused by the forgetting factor of 0.8 which increases the analyzed variance such that the new model ensemble receives a higher variability. Thus, the current LSEIK setup is not able to maintain a constant error approximation for the fields with no observation information for longer time periods. The standard deviation of the sea-ice concentration increases up to 25%, but is estimated to be almost constant for the first two months (7-13%). The standard deviation of the sea-ice thickness increases up to 3 m and the increase starts almost instantaneuosly after the first assimilation step which was not the case for the SEIK Filter setup (Figure 4.23, center).

The LSEIK is able to produce an almost constant sea-ice velocity standard deviation (Figure 4.32). Here, the estimated velocity standard deviation is between 2 and 4 $\mathrm{cm\,s^{-1}}$ and therefore in the same order of magnitude and larger than the observation error of approximately 1.6 $\mathrm{cm\,s^{-1}}$. Therefore, it is expected that the LSEIK analysis derives a direct and more significant drift update because the weights for the drift innovation are larger for larger variances. The different error estimates produced by the SEIK and LSEIK algorithms for the sea-ice drift are a result of the localization.

Compared to the SEIK Filter (Figure 4.1), the LSEIK obtains a better drift estimate (Figure 4.33). The local analysis more often results in a drift with a rms error closer

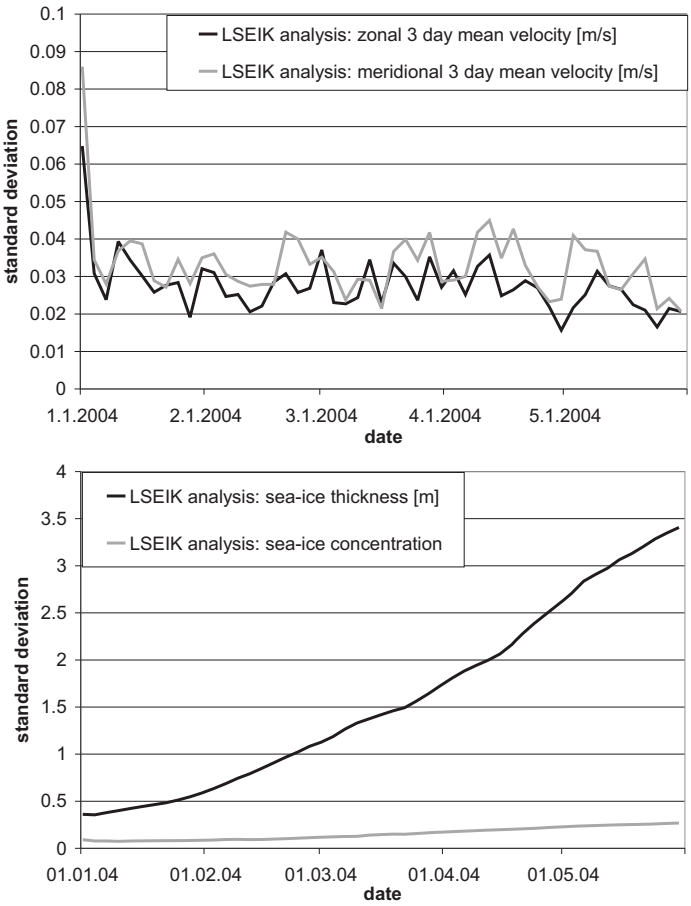

Figure 4.32: Estimated standard deviation of sea-ice velocity (top), and concentration and thickness (bottom) with the Local SEIK Filter.

to or even below the observation error of 1.6 $\mathrm{cm\,s^{-1}}$. However, the rms error increase during the forecast is larger than in the SEIK Filter (Figure 4.1).

The example of the 3 day mean drift vectors from 1 - 4 March 2004 (corresponds to assimilation step no. 21) reveals the significant drift improvement by the LSEIK analysis (Figure 4.34). The sea-ice drift forecast produces a larger drift in the Beaufort Sea and a drift parallel to the Canadian Archipelago which is not present in the observation (Figure 4.35, top). The local analysis obtains directly a drift reduction in the Beaufort Sea and a correction in the drift direction near the Canadian Archipelago. Still, the larger observed drift in the gyre from the East Siberian Sea to the pole seems only little improved. This example also reveals that a sustainable drift improvement is still small even after 20 assimilation steps because the forecast drift (Figure 4.34, top) is more similar to the reference simulation (Figure 4.35, bottom) than to the assimilated drift

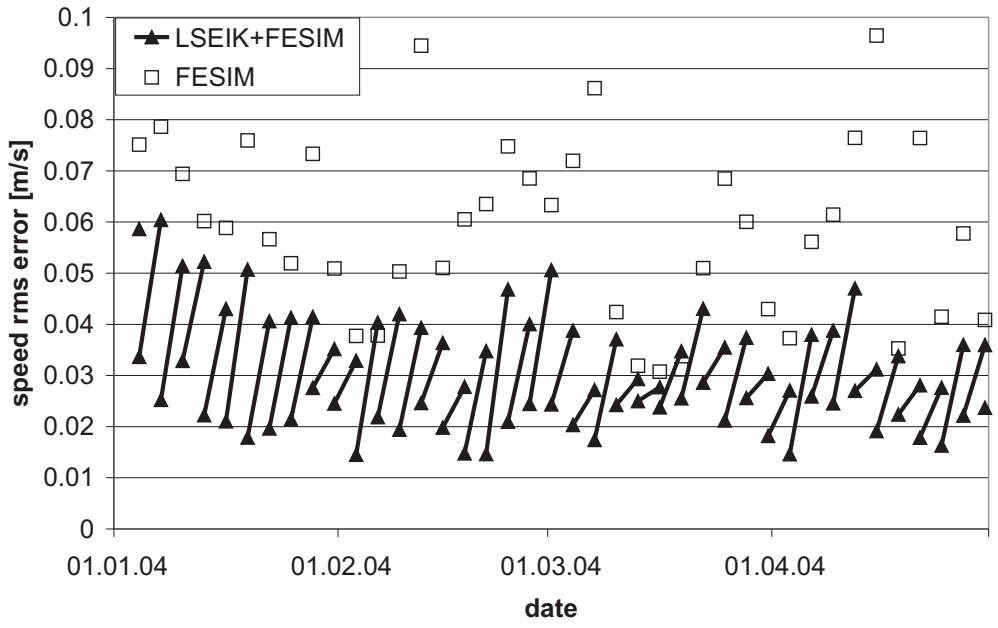

Figure 4.33: Arctic-wide averaged sea-ice velocity rms error of reference simulation (squares) and assimilation (triangles) with respect to the satellite derived sea-ice velocity. The lines between triangles represent the increase of sea-ice velocity difference during the model forecast integration. The change between triangles at same date represents Local SEIK Filter analysis derived corrections.

field (Figure 4.34, bottom).

To compare the drift performance due to the assimilation, again three selected buoy trajectories as in Section 4.2 are examined (Figure 4.36). For the buoy track 3982 and 24293, the LSEIK assimilation improves the simulated trajectory considerably. Only for buoy no. 40299, the LSEIK analysis is not able to improve the drift even further. Along the true trajectory of buoy no. 40299 the assimilation is able to produce the eastward drift components (Figure 4.37, top, positive values) that the SEIK has not been able to reproduce (Figure 4.8, top). This improvement is directly caused by the LSEIK analysis; the forecast is not able to simulate the eastward drift and provides a drift which is more similar to the reference simulation (Figure 4.37, bottom). While the LSEIK provides an improved direct drift analysis, the SEIK Filter obtains a sustainable drift improvement which is not as instantaneous and caused by sea-ice concentration and thickness changes that affect sea-ice velocities during the model forecast.

For the time period of 1 January - 30 April 2004, the 3 day mean sea-ice concentrations, derived from the LSEIK analysis results, obtain similar results as the reference simulation and show differences in the marginal ice zone to the satellite derived concentration data. The marginal ice zones is not much affected by the LSEIK algorithm due to the fact

LSEIK Forecast

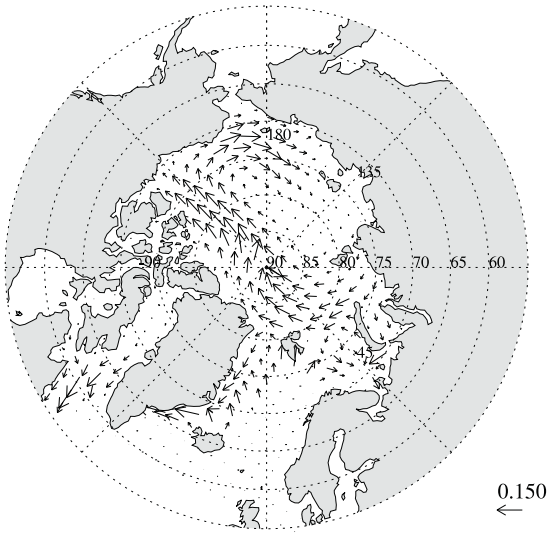

LSEIK Analysis

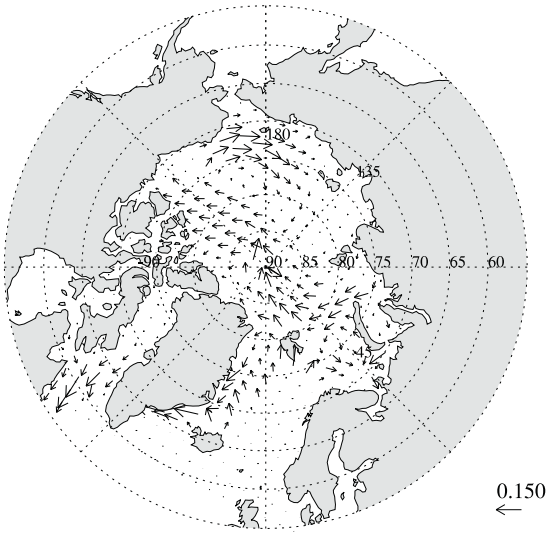

Figure 4.34: Sea-ice drift for 1 - 4 March 2004 from forecast (top) and analysis derived drift (bottom) with Local SEIK Filter.

Observation

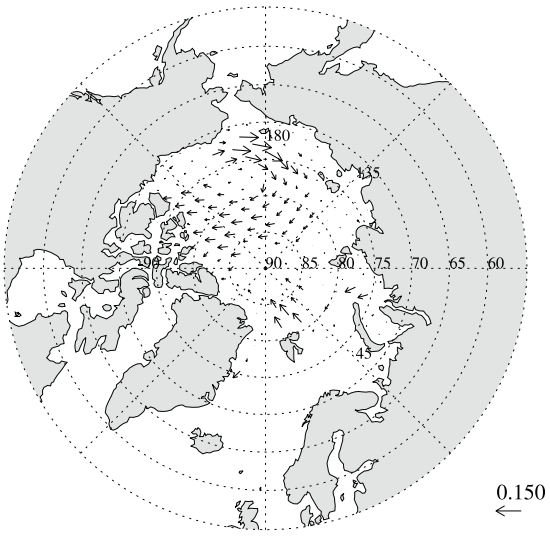

FESIM

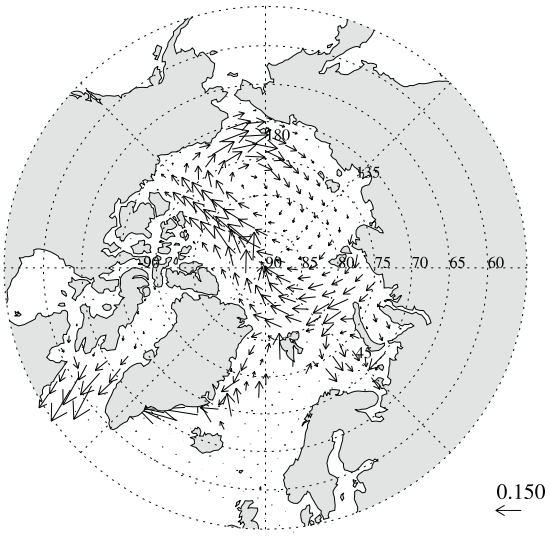

Figure 4.35: Sea-ice drift for 1 - 4 March 2004 from satellite derived drift (top) and reference simulation (bottom).

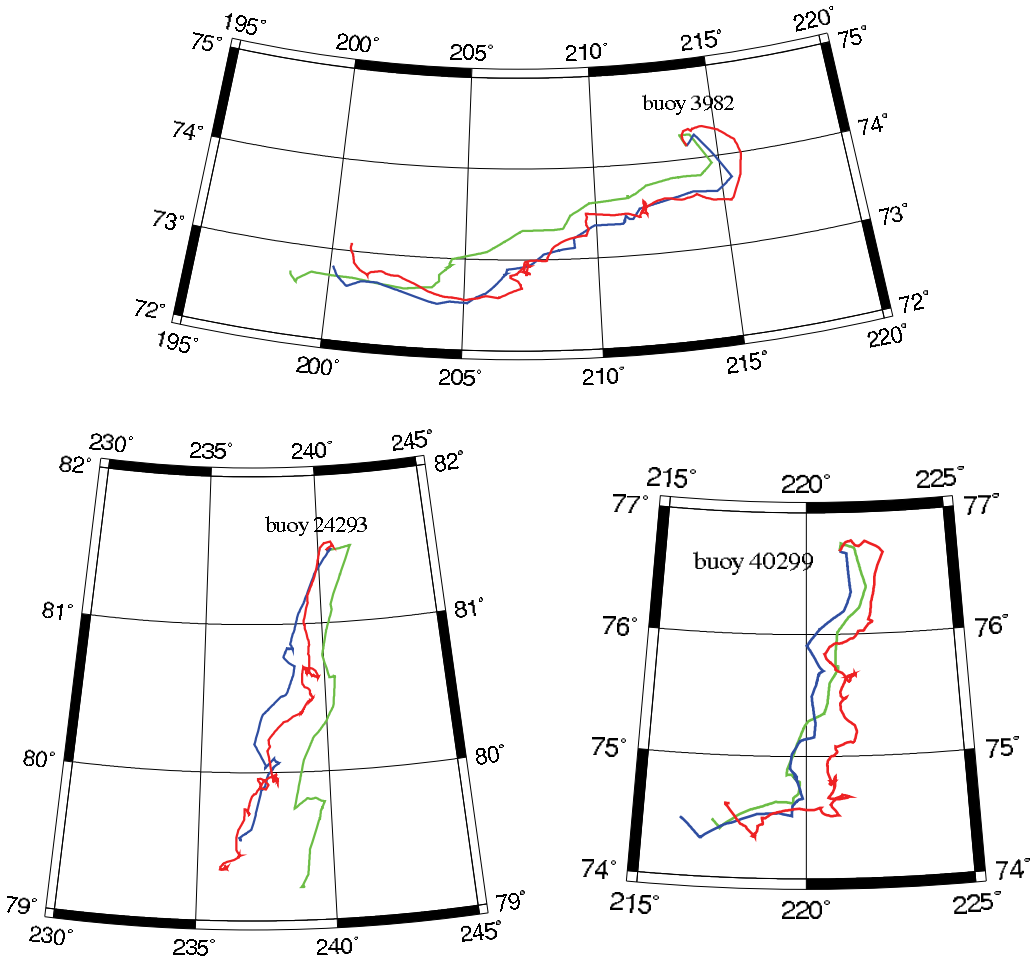

Figure 4.36: Three selected buoy trajectories for 1 January - 30 April 2004: buoy no. 3982 (top) between the Beaufort and Chukchi Seas, 24293 (bottom left) north of Canadian Archipelago and 40299 (bottom, right) in the Beaufort Sea. Red - deployed drifting buoy, green - trajectory from the reference simulation, blue - trajectory from the Local SEIK assimilation results.

that no analysis is done where no observations are available. The example for the 1 - 4 March 2004 (Figure 4.38) reveals that the marginal ice zone (MIZ) of the assimilation results resembles an ensemble forecast simulation without any SEIK analysis. A broad MIZ is present instead of a sharp sea-ice edge as it was observed. Thus, the wide MIZ is an averaging effect of the initial ensemble estimation which is maintained in the course of the assimilation.

Scatterplots (Figure 4.39) also reveal that the sea-ice concentration is very well estimated with the LSEIK analysis. It provides slightly better estimates for the sea-ice concentration than the reference simulation. The correlation between modeled/assimilated and observed sea-ice concentration has been increased with the assimilation. In the

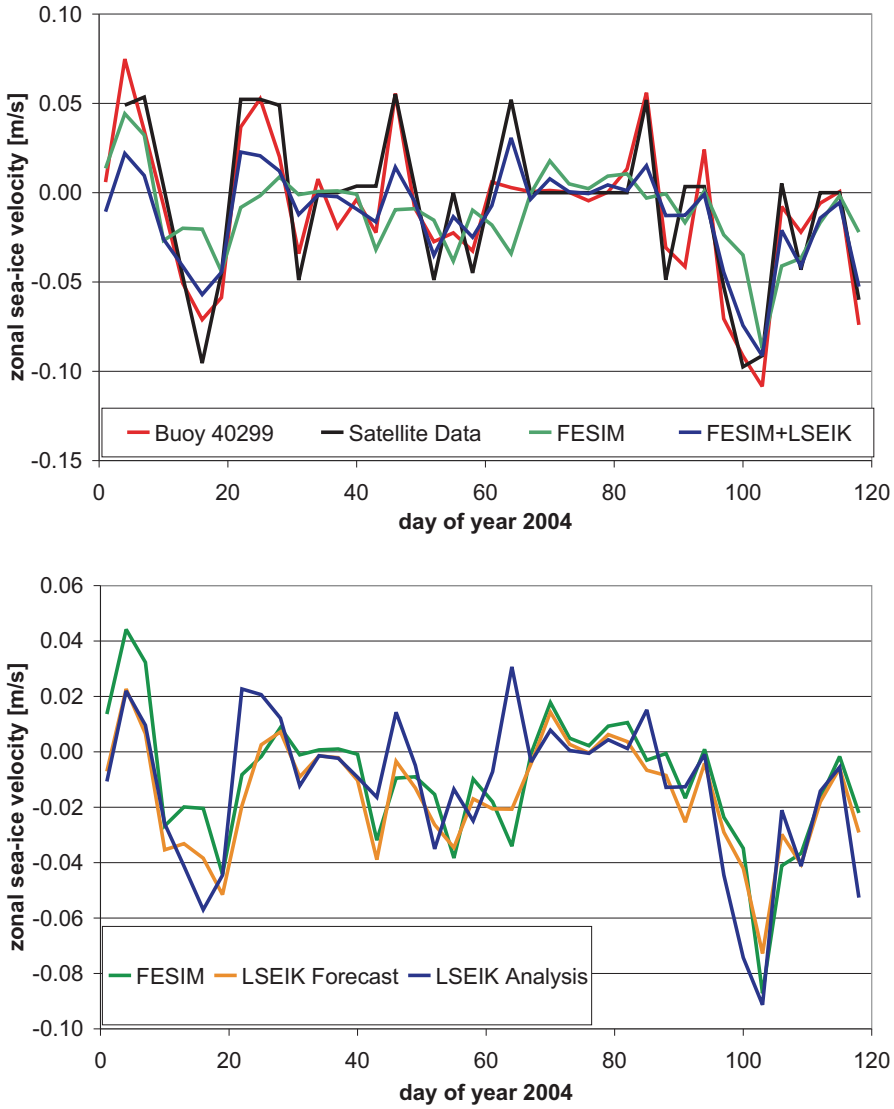

Figure 4.37: The zonal velocity along the track of the buoy no. 40299: LSEIK, satellite, reference and buoy velocity (top); LSEIK forecast and analysis and reference velocity (bottom).

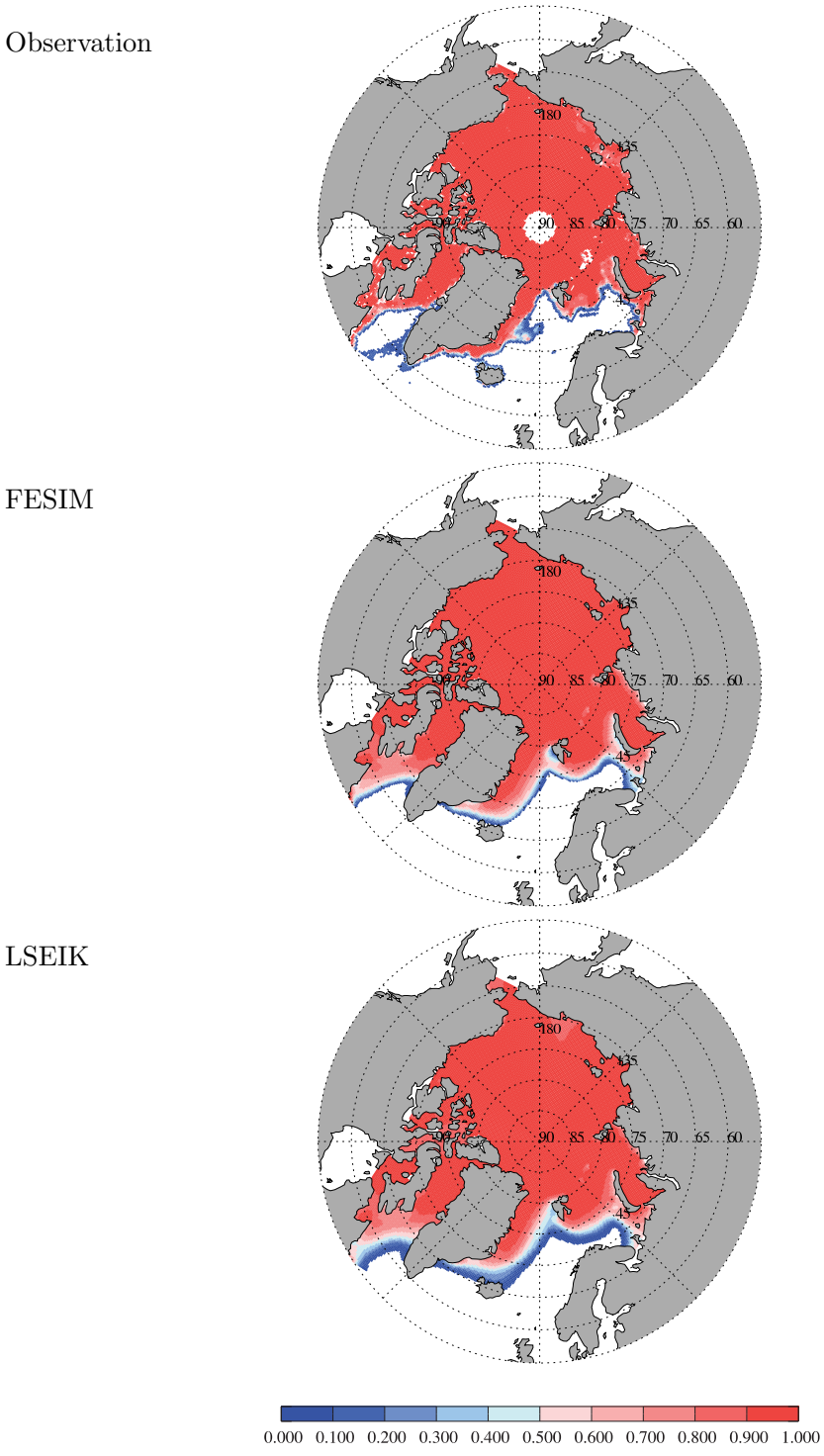

Figure 4.38: The 3 day mean sea-ice concentration in the Arctic derived from the observation (top), FESIM (center), and Local SEIK analysis (bottom) from 1 - 4 March 2004.

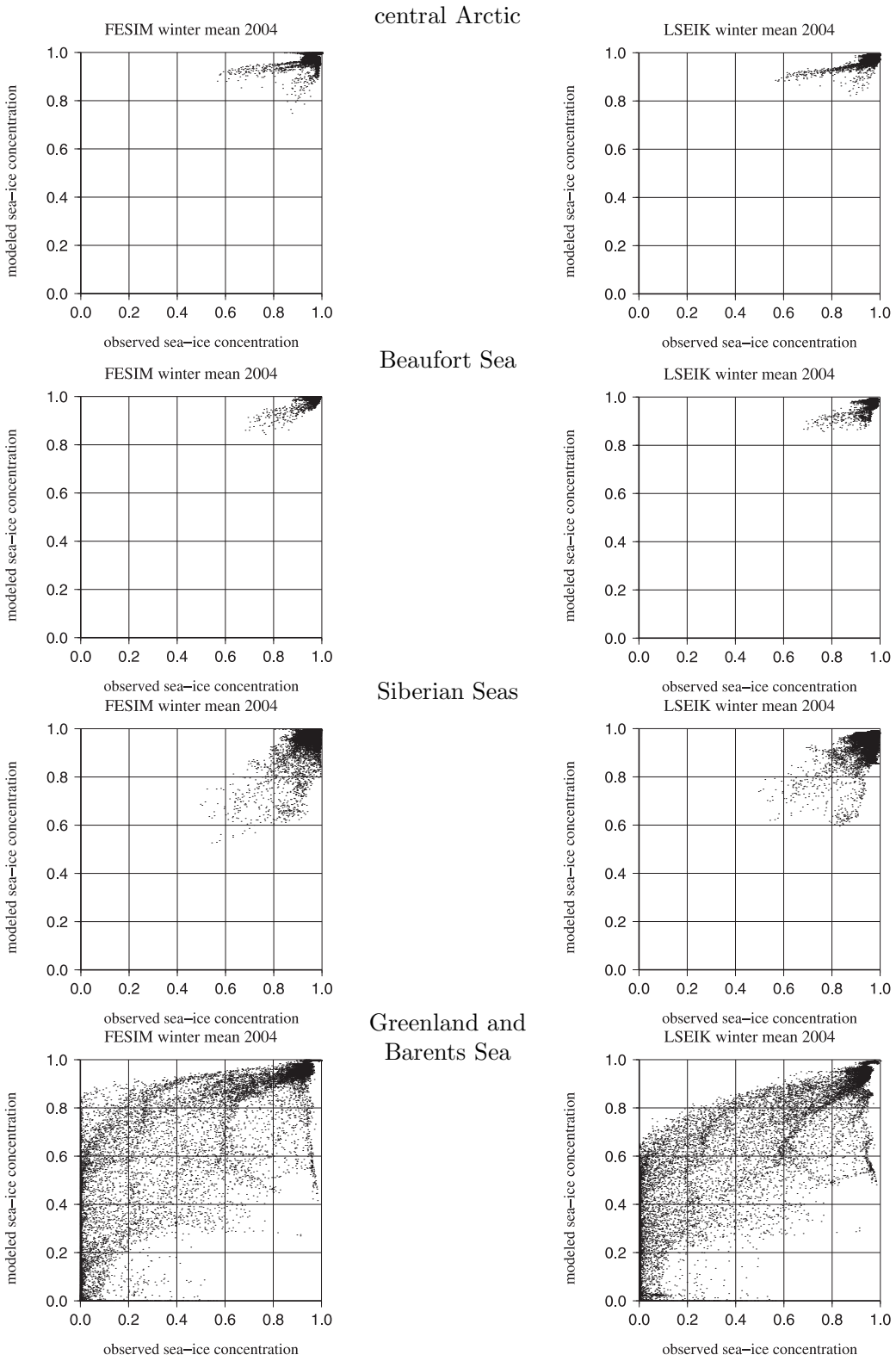

Figure 4.39: Modeled vs. observed sea-ice concentration: mean for 1 January - 30 April 2004; reference simulation (left) and LSEIK assimilation results (right). Data are split into four regions as in Figure 4.9.

central Arctic the correlation is increased from 0.5 (without assimilation) to 0.6 (with assimilation). In the Beaufort Sea the correlation is increased from 0.4 to 0.8 and in the Siberian Seas from 0.5 to 0.6. However in the Barents and Greenland Seas the correlation of 0.9 remained. Here, the rms error is, however, decreased from 0.23 (without assimilation) to 0.21 (with assimilation). Thus, the sea-ice concentration of the entire region has been improved slightly with the data assimilation. Since the reference simulation already provides a good sea-ice concentration representation, it was not expected to obtain a further improvement.

The sea-ice thickness from the LSEIK analysis is not as much affected as in the SEIK analysis. Here, effects on the sea-ice thickness are more local. For example the sea-ice thickness in the Beaufort Sea is slightly reduced (Figure 4.40) compared to the reference simulation (Figure 4.10, top). Also the smoothed isolines of the sea-ice thickness are replaced by a more patchy structure of the thickness ranges.

To sum up, the LSEIK analysis derives a considerable, direct drift improvement. Due to the small inertia of sea ice, the model state is almost not aware of the drift improvement after the first integration step during the forecast. Sea-ice concentration and thickness changes are too small to yield a sustainable drift improvement so that the drift forecast resembles more the reference simulation than the observation. The update for the sea-ice thickness is less pronounced than in the SEIK Filter setup such that the drift improvement is less persistent. Thus, the local drift analysis yields an improved drift field, but there is no significant improvement for the fields as the thickness where the assimilation algorithm has no observation information.

4.6.2 Local SEIK Analysis with Sea-Ice and Ocean State

In a further experiment, ocean temperature and salinity were included in the localized state, so that they were directly affected by the LSEIK analysis. The estimated standard deviation for the sea-ice fields are almost identical (Figure 4.41) and provides very similar results in sea-ice drift, concentration and thickness, but causes numeric instabilities after approximately 4 months of assimilation. Since the correlation between sea-ice drift and ocean temperature and salinity is very weak, the re-initialization of the ensemble after the analysis phase produces very strong temperature/salinity anomalies which then cause numerical instabilities in the ocean mixed layer scheme.

4.7 Summary

The results of sea-ice drift data assimilation show that the SEIK Filter is a powerful instrument which effectively adjusts the model fields based on their statistical properties. This leads to an improved agreement of model state and observation, even for ice concentration and thickness that are modified in course of the assimilation based on statistical correlations to the drift. A validation with independent buoy drift and observed sea-ice concentration data supports the applicability of the SEIK Filter for data assimilation in a sea-ice model.

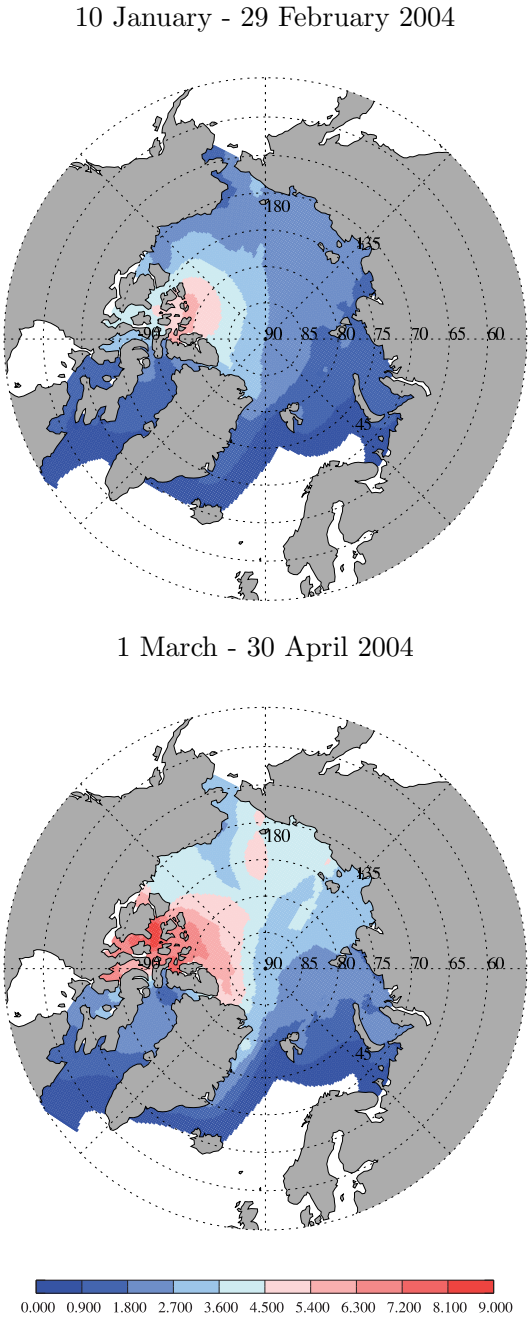

Figure 4.40: Mean sea-ice thickness distribution results [m] from 1 January - 29 February (top) and 1 March - 30 April 2004 (bottom) derived from the Local SEIK Filter.

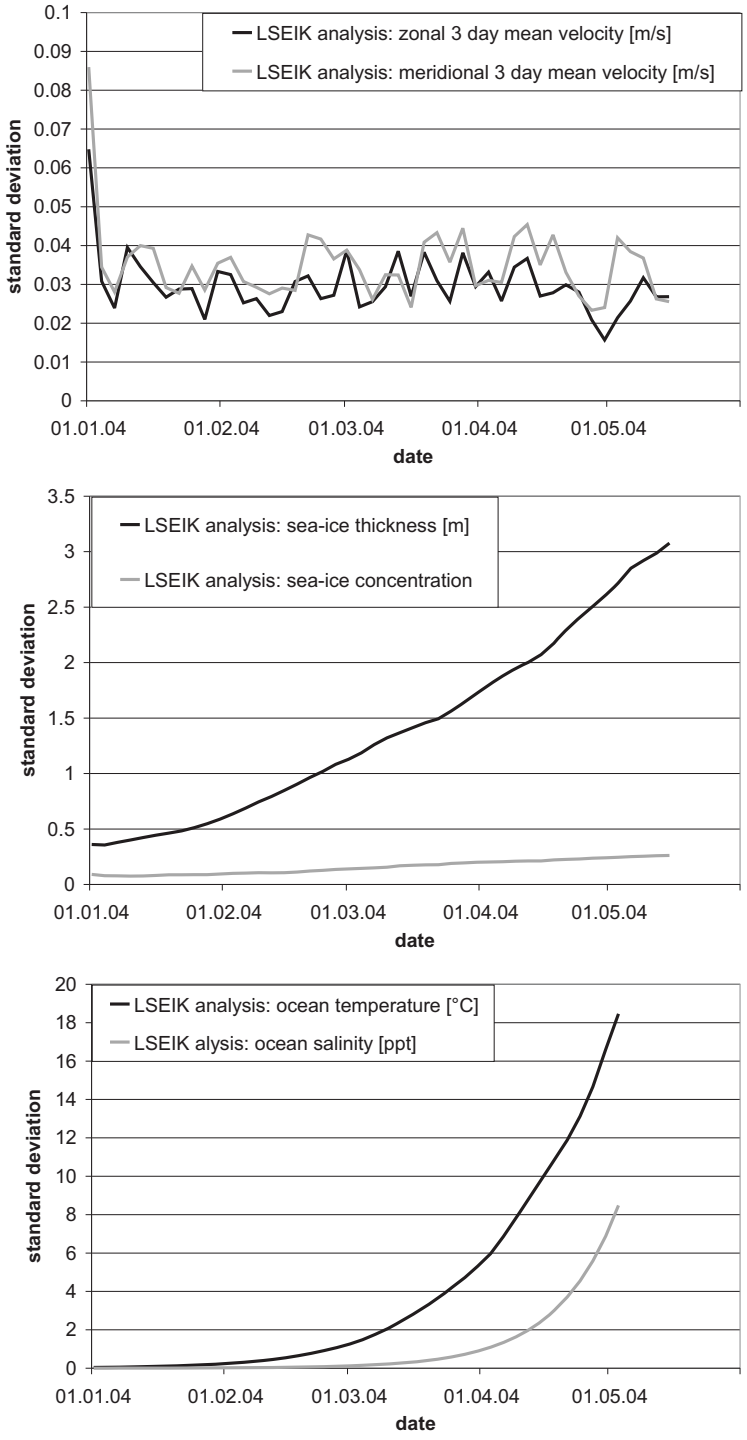

Figure 4.41: Estimated standard deviation of the sea-ice velocity (top), the sea-ice concentration and thickness (center), and the ocean temperature and salinity (bottom) derived from the Local SEIK Filter with the sea-ice and ocean state localization.

In many cases, the SEIK analysis does not lead to an instantaneous drift correction. Instead the drift improvement is obtained gradually due to SEIK analysis modifications of the sea-ice concentration and thickness. These sea-ice variables influence significantly the drift in the following SEIK forecast. Such a dependence leads to another conclusion: the presented SEIK Filter setup is able to produce reliable drift modification for compact ice conditions. In regions with less compactness the drift is predominantly dependent on surface and ocean forcing. Since the forcing is the same for all ensemble members the SEIK algorithm obtains less correlations between the sea-ice drift and thickness in those regions, and the assimilation therefore leads to insignificant modifications for a sustainable drift improvement. Thus, it is clear that the drift modifications at the ice edge cannot be satisfying for the presented SEIK Filter setup.

The SEIK derived sea-ice concentration represents a realistic state over the total assimilation period compared to the satellite observations. Additionally it is found that the sea-ice concentration is mainly determined by the SEIK forecast and the SEIK analysis provides less modifications whereas the largest impact on the sea-ice state due to the SEIK analysis affects the sea-ice thickness. The sparse data base of sea-ice thickness measurements prevents a thorough validation of modified sea-ice thickness fields as it is possible for the sea-ice concentration. Data sets of ULS and HEM are used to evaluate the sea-ice thickness estimates derived from the SEIK assimilation procedure. The assimilation produces a systematic overestimation of the thickness but the thickness pattern is reliable well represented compared with ULS derived sea-ice thickness maps.

The validation of sea-ice thickness with the ULS data also reveals that the assimilation is able to produce a thickness range similar to the observations which the model alone is not able to cover. The regions of very thin ice and thick ice also agree well with the assimilation results rather than the reference results. It seems that generally sea-ice models alone can not simulate the observed sea-ice thickness variability of individual cruises. The observed sea ice thickness variability range can usually be represented by model results when several cruises are considered as in *Rothrock et al.* (2003). Model results for individual cruises often do not cover the full range of observed thicknesses and a regression line of modeled vs. observed thickness might often lead to a slope close to zero as it is shown in section 4.3.1. In our case, the slope of the regression line for the simulated vs. observed thickness is increased from 0.19 (without assimilation) to 1.26 (with assimilation). Thus, a higher spatial variability of sea-ice thickness is obtained.

Also a higher temporal variability of the sea-ice thickness distribution has been achieved with the assimilation: A typical sea-ice thickness pattern change from a summer to a winter distribution is simulated with the assimilation.

A problem in the setup presented here is the small drift variance, which is produced by the SEIK analysis. The ensemble forecast is not able to increase the drift variance considerably, which is mainly due to the use of identical, unperturbed atmospheric and ocean forcing fields for all ensemble members. Thus, very similar drift results are predicted for all ensemble members. Another issue is the spatial distribution of the ensemble variance. Strong drift events produce large, local variances which lead to significant modifications of the sea-ice state. Under calm atmospheric conditions the variance is very small and the SEIK Filter analysis maintains an almost unchanged state. Some ways to achieve an

increased ensemble variability have already been mentioned: atmospheric perturbations, or different model physics for different ensemble members by introducing variations for physical parameters like the lead closing parameter h_0, the ice strength parameter $P^\star$, or the atmospheric drag coefficient c_a.

Although the sea-ice drift is not that much affected directly by the SEIK analysis the thickness change is pronounced. This is accompanied by modifications of sea-ice mass and concentration. An alternative setup which conserves ice mass but modifies actual ice thickness by adjusting ice concentration accordingly yields unrealistic results.

Assimilation with the Local SEIK Filter (LSEIK) also results in an improved drift estimate. Here, the drift improvement is achieved directly by the LSEIK analysis. The drift improvement is similar for the SEIK and LSEIK setup considering longer time periods. If only a few assimilation steps are considered, the LSEIK provides a better drift estimate. Compared to the reference simulation the LSEIK derived sea-ice concentration is closer to the satellite observations. The sea-ice thickness is significantly less modified compared to the SEIK derived thickness estimates. A sustainable effect to improve the sea ice drift is not produced with the LSEIK but with the SEIK Filter. The SEIK Filter achieves the drift improvement after some assimilation steps by a significantly changed sea ice thickness distribution that produces a sea ice drift which is closer to the observations. Therefore, it seems to be necessary to compute an update for the thickness and concentration distribution with the LSEIK assimilated drift field to derive a sustainable effect for the sea-ice state.

5 Conclusions and Outlook

The regional Finite Element Sea Ice Model (FESIM) for the Arctic has been presented along with its application to sea-ice drift data assimilation utilizing the Singular Evolutive Interpolated Kalman (SEIK) Filter, which estimates the system's state by combining all statistical knowledge of the system including measurements, model results and their error estimations. So far the SEIK Filter has not been employed for sea-ice data assimilation, neither for sea-ice concentration nor for velocity. Here, the attention has been focused on the sea-ice velocity assimilation examining the sea ice dynamics.

The FESIM achieves a realistic, seasonally varying sea-ice cover. The observed long-term sea ice decline is simulated as well and amounts to -6.3% in the last 15 years. The simulation of the winter sea-ice concentration agrees well with satellite observations but the location of the ice edge is less well simulated. The summer sea-ice concentration simulation seems to be underestimated in the central Arctic and overestimated in the Beaufort Sea.

The high variability of the sea ice circulation due to the dependence on the atmospheric forcing is well represented. The direction of the drift is well represented, too. The absolute sea-ice velocity is partly overestimated and partly underestimated depending on the drift regime. The recirculation of sea ice is overestimated up to 8 $\mathrm{cm\,s^{-1}}$ while the ice velocity across the Arctic is underestimation of up to 5 $\mathrm{cm\,s^{-1}}$. Such a systematic deviation explains the overestimation of sea-ice concentration in the Beaufort Sea. An underestimated drift in the Beaufort Sea leaves more ice in the Western Arctic and an overestimated recirculation of ice leads to an overestimated supply of sea ice into the Beaufort Sea.

The sea-ice volume decrease and increase within a year can be explained by thermodynamical growth and melt. However, the minima and maxima fluctuate during the years. This is a result of the dynamic process of deformation and sea-ice export (decreasing volume in the central Arctic in case of strong export events; increasing volume in case of reduced export). The FESIM is also able to simulate reliable sea-ice thickness patterns similar to ULS data derived sea-ice thickness maps.

The FESIM simulates a realistic sea ice state but still there are discrepancies to observations. This work has been carried out with the intention to obtain a more reliable sea ice state with sea-ice data assimilation to obtain further information for model improvement.

The data assimilation of observed sea-ice velocities affects the model state in various ways to produce drift estimates which are closer to the observations. Due to lack of drift data during the summer period and high computational cost no experiment running for a whole year or longer has been examined. Therefore, it is not clear how the model state behaves during summer in case of long-term assimilation. Two time periods have

been investigated: the winter 2004 from 1 January to 30 May and autumn 2000 from 1 October to 9 December.

For the velocities the SEIK Filter is able to maintain an almost constant error estimation. Overestimated initial covariances are reduced during the first 2 - 4 assimilation steps. After that the ensemble variability is very small. The standard deviation of the drift ensemble is below 1 $\mathrm{cm\,s^{-1}}$. This is due to the fact, that the SEIK analysis is reducing the variance significantly and the sea-ice model is not able to increase independently the ensemble variability because the same model physics and forcing conditions are applied for every ensemble member. This in turn leads to a very small, directly drift correction from the SEIK analysis during the assimilation. To increase the ensemble variability within the forecast phase it might be appropriate to include a perturbation in the atmospheric forcing fields.

A sustainable drift improvement is achieved by the SEIK derived sea-ice concentration and thickness modification. The ensemble variance for the sea-ice concentration and thickness increases after 3 - 4 months of the otherwise unconstrained velocity assimilation. The increasing standard deviation is not an indicator of the quality of the estimated mean state and no statement about the agreement between model and observation can be made from it. Thus, the state has to be compared/validated with observations.

A comparison has shown that the spatial averaged deviation of the SEIK analysis drift and satellite drift is reduced to 2 - 3 $\mathrm{cm\,s^{-1}}$. Without assimilation the spatial averaged deviation amounts up to 10 $\mathrm{cm\,s^{-1}}$. An assessment of assimilated drift shows a significant improvement for simulated buoy trajectories in many cases.

Sea-ice drift assimilation in the presented setup has been shown to improve the sea-ice concentration slightly. Since FESIM reference results have already provided a reliable sea-ice concentration representation with regard to SSM/I derived concentration data, it was not expected to obtain further improvement for the sea-ice concentration in course of the sea-ice drift data assimilation. It has also been found that the SEIK analysis is not the dominant process that influences the sea-ice concentration, but it is the model integration in the SEIK forecast phase that modifies sea-ice concentration most.

In the assimilation procedure the sea-ice thickness change is dominated by the SEIK analysis that results in the most striking effect. The spatial thickness variability increases considerably. The modified thickness pattern in both case studies agrees well with the seasonal thickness maps of *Bourke and Garrett* (1987), although the absolute sea-ice thickness is slightly overestimated. Model results with drift assimilation represents the thickness pattern even of single submarine cruises well. Nevertheless, the absolute thickness values have to be handled with care because the temporal and spatial observational data set is sparse and the modeled thickness cannot be validated over longer periods. The overestimation of 1 m for autumn thickness values due to assimilation is significant.

Another nice result from the autumn 2000 case study is the evolution of the simulated ice thickness pattern from a summer/autumn distribution to a winter distribution similar to the seasonal thickness maps of *Bourke and Garrett* (1987). Without assimilation, the model is not able to produce such a rapid thickness redistribution by dynamic thinning and thickening. The strong influence of the SEIK Filter on the sea-ice thickness field produces the thickness conversion due to statistical correlations between thickness and

drift.

The experiment with the local SEIK Filter (LSEIK) shows similar long-term drift results from the filter analysis as for the SEIK Filter. Even though the LSEIK analysis provides direct drift improvement and a better drift variance estimation than for the SEIK, a sustainable effect on to the ensemble drift forecast is not produced. That means, the LSEIK forecasted drift resembles the reference drift and the forecast drift deviation to satellite data is less reduced than for the SEIK forecast. The thickness is less modified but the concentration agreement is enhanced similar as for the SEIK Filter results. To obtain the effect of the assimilated drift on to the sea-ice thickness distribution a redistribution due to the updated drift would have to be determined additionally. To include the water column into the local state that is delivered to the LSEIK analysis and re-initialization is found to be a source of numeric instabilities during the model integration in course of the assimilation after a period of some months.

The SEIK Filter assimilation method presented here, is well applicable to derive realistic initial fields for operational systems because within a few assimilation steps a reliable sea-ice state is achieved which provides a good estimate of the distribution of the sea ice thickness and concentration. On the other hand the LSEIK drift assimilation seems to be more practical for long-time assimilation periods when an additional sea-ice mass advection due to the updated drift is applied. For the SEIK as well as for the LSEIK the influence of the data assimilation on the marginal ice zone is small due to the prevailing free drift conditions or the lack of observational data in this region, respectively. To improve the simulation in these areas, the assimilation of sea-ice concentration data seems to be more useful to improve the sea-ice conditions there, especially with respect to ship routing.

The thickness overestimation due to the assimilation has to be further studied. There seem to be several possible solutions: (1) additional assimilation of sparse thickness data which are available such that the thickness values can be constrained; (2) variation of model parameters like the drag coefficients or the ice strength parameter over the ensemble member to modify the drift sustainably also in the marginal ice zone.

Furthermore, the SEIK Filter provides the possibility of assimilating various sea-ice variables simultaneously and an additional sea-ice concentration assimilation is worthwhile. Then the sea-ice state is constrained closer to the observations. The potential of the SEIK Filter is not yet exhausted and this work presents a first study of the applicability of sea ice data assimilation. Since the system still features several differences from observations it is clear that the model should be improved further.

List of Acronyms

AIDJEX	Arctic Ice Dynamics Joint Experiment (1970-1976)
CERSAT	Centre ERS d'Archivage et de Traitment (French ERS Processing and Archiving Facility), Plouzane, France
cf.	confer
ECMWF	European Centre for Medium-Range Weather Forecasts
EKF	Extended Kalman Filter
EM	electromagnetic
EnKF	Ensemble Kalman Filter
ERS	European Remote Sensing Satellite of the European Space Agency
ETOPO	Earth Topography Data
EVP	elastic viscous plastic
FEM	finite elements method
FESIM	finite element sea ice model
FESOM	finite element sea ice ocean model
GPS	Global Positioning Systems
GreenIce	Greenlandic Arctic Shelf Ice and Climate Experiment EVK2-CT-2002-00156; European Union funded project
HEM	helicopter-borne electromagnetic
IABP	International Arctic Buoy Programme, hosted by the University of Washington, Seattle, WA, USA
IFREMER	Institut français de recherche pour l'exploitation de la mer (French Research Institute for Exploitation of the Sea), Issy-les-Moulineaux Cedex, France
KF	Discrete Kalman Filter
LSEIK	Local Singular Evolutive Interpolated Kalman Filter
LW	long wave
MIZ	Marginal ice zone
NCAR	National Center for Atmospheric Research, USA
NCEP	National Centers for Environmental Prediction,USA
NSIDC	National Snow and Ice Data Center, Boulder, CO, USA
OI	Optimal Interpolation
PDAF	parallel data assimilation framework
PDF	probability density function
ppt	parts per thousand
QuikSCAT	Quick Scatterometer (satellite sensor)

RGPS	Radarsat Geophysical Processor System
RHS	right-hand size
rms	root mean squared
SEEK	Singular Evolutive Extended Kalman Filter
SEIK	Singular Evolutive Interpolated Kalman Filter
SLP	sea level pressure
SSM/I	Special Sensor Microwave Imager (satellite sensor)
SW	short wave
TDS	Transpolar Drift Stream
ULS	upward looking sonar
URL	Uniform Resource Locator
VP	viscous plastic

List of Figures

List of Tables

Bibliography

Agnew, T. A., and H. Le, A more comprehensive view of the dynamics of the arctic sea ice as revealed through 85.5 GHz SSM/I imagery, *NSIDC Notes*, ***19***, Nat. Snow and Ice Data Cent., Boulder, Colo., 1996.

AMAP, *AMAP Assessment Report: Arctic Pollution Issues*, Arctic Monitoring and Assessment Programme, Oslo, Norway, 1998.

Andreas, E. L., and B. A. Cash, Convective heat transfer over wintertime leads and polynya, *J. Geophys. Res.*, ***104***(C11), 25,721–25,734, 1999.

Arbetter, T., A. Lynch, J. Maslanik, and W. Meier, Effects of data assimilation of ice motion in a basin-scale sea ice model, in *Ice in the Environment: Proceeding of the 16th IAHR International Symposium on Ice*, edited by V. Squire and P. Langhore, pp. 186–193, International Association of Hydraulic Engeneering and Research, Dunedin, New Zeeland 2-6 December 2002, 2002.

Barry, R. G., M. C. Serreze, and J. A. Maslanik, The Arctic sea ice-climate system: observations and modeling, *Rev. Geophys.*, ***31***(4), 397–422, 1993.

Belchansky, G. I., D. C. Douglas, and N. G. Platanov, Duration of the Arctic Sea Ice Melt Season: Regional and Interannual Variability, 1979-2001, *J. Climate*, ***17***(1), 67–80, 2004.

Bjørgo, E., O. Johannessen, and M. Miles, Analysis of merged SSMR/SSMI time series of Arctic and Antarctic sea ice parameters, *Geophys. Res. Lett.*, ***24***, 413–416, 1997.

Bourke, R. H., and R. P. Garrett, Sea ice thickness distribution in the Arctic Ocean, *Cold Reg. Sci. Technol.*, ***13***, 259–280, 1987.

Bourke, R. H., and A. S. McLaren, Contour Mapping of Arctic Basin Ice Draft and Roughness Parameters, *J. Geophys. Res.*, ***97***(C11), 17,715–17,728, 1992.

Bryan, K. S., S. Manabe, and R. L. Pacanowski, A global ocean-atmosphere climate model. part II: The oceanic circulation, *J. Phys. Oceanogr.*, ***5***, 30–46, 1975.

Burgers, G., P. J. van Leeuwen, and G. Evensen, Analysis scheme in the ensemble Kalman Filter, *Mon Weather Rev*, ***126***(6), 1719–1724, 1998.

Campbell, W. J., The wind-driven circulation of ice and water in the polar ocean, *J. Geophys. Res.*, ***70***, 3279–3301, 1965.

Cavalieri, D., C. Parkinson, and K. Vinnikov, 30-Year satellite record reveals contrasting Arctic and Antarctic decadal sea ice variability, *Geophys. Res. Lett.*, ***30***(28), doi: 10.1029/2003GL018031, 2003.

Comiso, J. C., D. J. Cavalieri, C. L. Parkinson, and P. Gloersen, Passive Microwave Algorithms for Sea Ice Concentration: A Comparison of Two Techniques, *Remote Sens. Environ.*, ***12***(60), 357–384, 1997.

Coon, M. D., G. A. Maykut, R. S. Pritchard, D. A. Rothrock, and A. S. Thorndike, Modeling the pack ice as an elastic-plastic material, *AIDJEX Bulletin*, ***24***, 1–105, 1974.

Courant, R., Variational methods for the solution of equilibrium and vibration, *Bull. Amer. Meteorol. Soc.*, ***49***, 1–23, 1943.

Dai, M., T. Arbetter, and W. Meier, Data assimilation of sea-ice motion vectors: Sensitivity to he perameterization of sea-ice strength, *Ann. Glaciol.*, ***44***, 357–360, 2006.

Danilov, S., and N. Yakovlev, A finite element ice model, unpublished, Alfred Wegener Institute for Polar and Marine Research, Bremerhaven, Germany, 2003.

Danilov, S., G. Kivman, and J. Schröter, A finite element ocean model: principles and evaluation, *Ocean Modelling*, ***6***, 125–150, 2004.

Dulière, V., On the assimilation of ice velocity and concentration data into large-scale sea ice models, Ph.D. thesis, Université catholique de Louvain, Faculté des sciences École doctorale en géosciences, 2007.

Dulière, V., and T. Fichefet, On the assimilation of ice velocity and concentration data into a large-scale sea ice models, *Ocean Sci.*, ***3***, 321–335, 2007.

Ebert, E. E., and J. A. Curry, An intermediate one-dimensional thermodynamic sea ice model for investigating ice-atmosphere interactions, *J. Geophys. Res.*, ***98***(C6), 10,085–10,109, 1993.

Eicken, H., From the Microscopic, to the Macroscopic, to the Rigional Scale: Growth, Microstructure and Properties of Sea Ice, in *Sea Ice: An Introduction to its Physics, Chemistry, Biology and Geology*, edited by D. N. Thomas and G. S. Dieckmann, pp. 22–81, Blackwell Science Ltd., 2003.

Emery, W. J., C. W. Fowler, and J. A. Maslanik, Satellite-derived maps of Arctic and Antarctic sea ice motion: 1988 to 1994, *Geophys. Res. Lett.*, ***24***(8), 897–900, doi: 10.1029/97GL00755, 1997.

Evensen, G., Sequential data assimilation with nonlinear quasi geostrophic model using Monte Carlo methods to forecast error statistics, *J. Geophys. Res.*, ***99***(C5), 10,143–10,162, doi:10.1029/94JC00572, 1994b.

Ezraty, R., and J. F. Piollé, *Sea Winds on Quikscat Polar Sea Ice Grids, User Manual*, CONVECTION report N° 5, V1.1, greenland Sea Convection Mechanism and their Implications, Fifth Framework Programme of the European Commission 1998-2002, Contract N° EVK2-2000-00058, 2001.

Ezraty, R., and J. F. Piollé, *Sea Ice Drift in the Central Arctic Combining Quikscat and SSM/I Sea Ice Drift Data User's Manual 1.0*, Laboratoire d'Océanographie Spatiale Département d'Océanographie Physique et Spatiale IFREMER/ Centre de Brest, 2004a.

Ezraty, R., and J. F. Piollé, *Sea-Ice Drift in the Central Arctic Estimated from Sea-Winds/Quikscat Backscatter Maps User's Manual **2.1***, Laboratoire d'Océanographie Spatiale Département d'Océanographie Physique et Spatiale IFREMER/ Centre de Brest, France, 2004b.

Ezraty, R., J. F. Piollé, L. Kaleschke, and G. Heygster, *Sea-Ice Concentration and drift in the Central Arctic Estimated from Special Sensor Microwave Imager Data User's Manual 1.0*, Laboratoire d'Océanographie Spatiale Département d'Océanographie Physique et Spatiale IFREMER/ Centre de Brest, France and Institute of Environmental Physics University of Bremen / Germany, 2004.

Fischer, H., Comparison of an optimized dynamic-thermodynamic sea ice model with observations in the Weddell Sea, Ph.D. thesis, Universität Bremen, Fachbereich Physik/Elektrotechnik, 1995.

Flato, G., and W. Hibler, Modeling pack ice as a cavity fluid, *J. Phys. Oceanogr.*, ***22***, 626–651, 1992.

Galerkin, B. G., Rods and plates: Series occuring in various questions concerning the elastic equilibrium of rods and plates (Russian), *Vestnik Inzhenerov i Tekhnikov*, ***19***, 897–908, petrograd, 1915.

Gibson, J. K., P. Kållberg, S. Uppala, A. Hernandez, and E. Serrano, *ERA Description. Re-Analysis (ERA) Project Report, Series 1*, European Centre for Medium-Range Weather Forecast (ECMWF), Shinfield Park, 1997.

Gill, A. E., *Atmosphere-Ocean Dynamics*, Academic Press, 1982.

Goosse, H., R. Gerdes, F. Kauker, and C. Köberle, Influence of the Exchanges between the Atlantic and the Arctic on Sea Ice Volume Variations during the Period 1955-97, *J. Climate*, ***17***, 1294–1305, 2003.

Haas, C., Evaluation of ship-based electromagnetic-inductive thickness measurements of summer sea-ice in the bellinghausen and amundsen sea, *Cold Reg. Sci. Techn.*, ***27***(1), 1–16, doi:10.1016/SO165-232X(97)00019-0, 1998.

Haas, C., Late-summer sea ice thickness variability in the Arctic Transpolar Drift 1991-2001 derived from ground-based electromagnetic sounding, *Geophys. Res. Lett.*, ***31***(L09402), doi:10.1029/2003GL019394, 2004.

Haas, C., and P. Jochmann, Continuous EM and ULS thickness profiling in support of ice force measurements, in *Proceedings of the 17th International Conference on Port and Ocean Engeneering under Arctic Conditions*, edited by S. Loeset, B. Bonnemaire, and M. Bjerkas, pp. 849–856, Departement of Civil and Transport Engeneering, Norwegian Universety of Science and Technology NTNU, Trondheim, Norway, 2, 2003.

Haas, C., S. Hendricks, and M. Doble, Comparison of the sea ice thickness distribution in the Lincoln Sea and adjacent Arctic Ocean in 2004 and 2005, *Ann. Glaciol.*, ***44***, in press, 2006.

Harder, M., Dynamic, roughness, and age of arctic sea ice - Numerical investigations with a large scale model, Ph.D. thesis, Universität Bremen, Fachbereich Physik/Elektrotechnik, 1996.

Harder, M., Roughness, age and drift trajectories of sea ice in large-scale simulations and their use in model verifications, *Ann. Glaciol.*, ***25***, 237–240, 1997.

Hibler, W. D., Differential sea ice drift II: Comparison of mesoscale strain measurements to linear drift theory predictions, *J. Glaciol.*, ***13***, 457–471, 1975.

Hibler, W. D., A Dynamic Thermodynamic Sea Ice Model, *J. Phys. Oceanogr.*, ***9***(4), 815–864, 1979.

Hibler, W. D., and W. B. Tucker, Some results from a linear viscous model of the Arctic ice cover, *J. Glaciol.*, ***22***, 293–304, 1979.

Hilmer, M., and P. Lemke, On the Decrease of Arctic Sea Ice Volume, *Geophys. Res. Lett.*, ***27***(22), 3751–3754, doi:10.1029/2000GL011403, 2000.

Holloway, G., and T. Sou, Has Arctic Sea Ice Rapidly Thinned?, *J. Climate*, ***15***, 1691–1701, 2002.

Houtekamer, P. L., and H. L. Mitchell, Data Assimilation Using an Ensemble Kalman Filter Technique, *Mon Weather Rev*, ***126***, 796–811, 1998.

Hunke, E. C., and J. K. Dukowicz, An Elastic-Viscous-Plastic Model for Sea Ice Dynamics, *J. Phys. Oceanogr.*, ***27***(9), 1849–1867, doi:10.1175/1520-0485(1997)027, 1997.

Ip, C. F., W. D. Hibler, and G. Flato, On the effect of rheology on seasonal sea-ice simulations, *Ann. Glaciol.*, ***15***, 17–25, 1991.

IPCC, *Climate Change 2007: The Physical Sciance Basis. Working Group I Contribution to the Fourth Assessment Report of the IPCC*, Cambridge University Press, Cambridge, United Kingdom and New York, 2007.

Jazwinski, A. H., *Stochhastic Processes and Filtering Theory*, Academic Press, New York, 1970.

Johannessen, O. M., L. Bengstsson, M. W. Miles, S. I. Kuzmina, V. A. Semenov, G. V. Alekseev, A. Nagurnyi, V. F. Zakharov, L. B. Bobylev, L. H. Pettersson, K. Hasselmann, and H. P. Cattle, Arctic climate change: observed and modeled temperature and sea-ice variability, *Tellus*, ***56A***, 328–341, 2004.

Kaleschke, L., Fernerkundung des Meereises mit passiven und aktiven Mikrowellensensoren, Ph.D. thesis, Fachbereich1 (Physik/Elektrotechnik), Universität Bremen, 2003.

Kaleschke, L., C. Lüpkes, T. Vihma, J. Haarpaintner, A. Borchert, J. Hartmann, and G. Heygster, SSM/I Sea ice remote sensing for mesoscale ocean-atmosphere interaction analysis, *Canadian Journal of Remote Sensing*, ***27***(5), 526–537, 2001.

Kalman, R., A new approach to linear filtering and prediction problems, *Trans. ASME, J. Basic Eng.*, ***82***, 35–45, 1960.

Kalney, E., M. Kanamitsu, R. Kistler, W. Collins, D. Deaven, L. Gandin, M. Iredell, S. Saha, G. White, J. Woolen, Y. Zhu, M. Chelliah, W. Ebisuzaki, W. Higgins, J. Janowiak, K. C. Mo, C. Ropelewski, J. Wang, A. Leetmaa, R. Reynolds, R. Jenne, and D. Josephs, The NCEP/NCAR 40-Year Reanalysis Project, *Bull. Amer. Meteorol. Soc.*, ***77***(3), 437–471, 1996.

Kimura, N., and M. Wakatsuchi, Relationship between sea-ice motion and geostrophic wind in the Northern Hemisphere, *Geophys. Res. Lett.*, ***27***(22), 3735–3738, doi: 10.1029/2000GL01149, 2000.

Kistler, R., E. Kalnay, W. Collins, S. Saha, G. White, J. Woollen, M. Chelliah, W. Ebisuzaki, M. Kanamitsu, V. Kousky, H. van den Dool, R. Jenne, and M. Fiorino, The NCEP-NCAR 50-Year Reanalysis: Mothly Means CD-ROM and Documentation, *Bull. Amer. Meteorol. Soc.*, ***82***(2), 247–268, 2001.

Köberle, C., and R. Gerdes, Mechanisms Determining the Variability of Arctic Sea Ice Conditions and Export, *J. Climate*, ***16***, 2843–2858, 2003.

König-Langlo, G., and E. Augstein, Parameterization of the downward longwave radiation at the Earth's surface in polar regions, *Meteorol. Zeitschrift*, ***N.F.3.***(H.6), 343–347, 1994.

Kreyscher, M., Dynamics of Arctic sea ice - Validation of different rheology schemes for the use in climate models, *Berichte zur Polarforschung*, ***291***, 1998.

Kreyscher, M., M. Harder, and P. Lemke, First results of the Sea Ice Model Intercomparison Project (SIMIP), *Ann. Glaciol.*, ***25***, 8–11, 1997.

Kreyscher, M., M. Harder, P. Lemke, and G. M. Flato, Results of the Sea Ice Model Intercomparison Project: Evaluation of sea ice rheology schemes for use in climate simulations, *J. Geophys. Res.*, ***105***(C5), 11,299–11,320, doi:10.1029/1999JC000016, 2000.

Krishfield, R. A., and D. K. Perovich, Spatial and temporal variability of oceanic heat flux to the Arctic ice pack, *J. Geophys. Res.*, ***110***(C7), doi:10.1029/2004JC002293, 2005.

Kwok, R., A. Schweiger, D. A. Rothrock, S. S. Pang, and C. Kottmeier, Sea-ice motion from satellite passive microwave imagery assessed with ERS SAR and buoy motions, *J. Geophys. Res.*, ***103***, 8191–8214, 1998.

Laevastu, T., Factors effecting the temperature of the surface layer of the sea., *Comment. Phys. Math.*, ***25***(1), 1960.

Lemke, P., W. D. Hibler, G. Flato, M. Harder, and M. Kreyscher, On the improvement of sea-ice models for climate simulations: The Sea Ice Intercomparison Project, *Ann. Glaciol.*, ***25***, 183–187, 1997.

Lieser, J. L., A Numerical Model for Short-term Sea Ice Forecasting in the Arctic, Ph.D. thesis, Universiät Bremern, Fachbereich Physik/Elektrotechnik, 2004.

Lindsay, R., and J. Zhang, The thinning of Arctic sea ice, 1988-2003: have we passed the tipping point?, *J. Climate*, ***18***, 4879–4894, 2005.

Lindsay, R., and J. Zhang, Assimilation of ice concentration in an ice-ocean model, *J. Atmos. Ocean. Technol.*, ***23***, 742–749, 2006.

Lindsay, R., J. Zhang, and D. Rothrock, Sea ice deformation rates from measurements and in a model, *Atmos. Ocean*, ***40***, 35–47, 2003.

Lisæter, K. A., J. Rosanova, and G. Evensen, Assimilation of ice concentration in a coupled ice-ocean model using Ensemble Kalman filter, *Ocean Dynamics*, ***53***, 368–388, 2003.

Long, R., *Kontinuumsmechanik*, Berliner Union, Stuttgart, 1964.

Manabe, S., K. S. Bryan, and M. J. Spelmann, A global ocean-atmosphere climate model with seasonal variation for future studies of climate sensitivity, *Dynam. Atmos. Oceans*, ***3***, 393–426, 1979.

Martin, T., Arctic Sea Ice Dynamics: Drift and Ridging in Numerical Models and Observations, Ph.D. thesis, Universität Bremen, Fachbereich Physik/Elektrotechnik, 2007.

Martin, T., and E. Augstein, Large-scale drift of Arctic Sea ice retrieved from passive microwave satellite data, *J. Geophys. Res.*, ***105***(C4), 8775–8788, doi: 10.1029/1999JC900270, 2000.

Martin, T., and R. Gerdes, Sea ice drift variability in AOMIP models and observations, *submitted*, , 2006.

Martin, T., and T. Martin, Anomalies of sea-ice transports in the Arctic, *Annals of Glaciology*, ***44***, 310–316, 2006.

Maykut, G. A., The surface heat and mass balance, in *The Geophysics of Sea Ice, NATO ASI Ser., Ser. B Phys.*, vol. 146, edited by N. Untersteiner, pp. 395–464, Plenum, New York, 1986.

Maykut, G. A., and M. G. M. Phee, Solar heating of the Arctic mixed layer, *J. Geophys. Res.*, ***100***(C12), 24,691–24,703, 1995.

Maykut, G. A., and N. Untersteiner, Some results from a time dependent thermodynamic model of sea ice, *J. Geophys. Res.*, ***76***(6), 1550–1575, 1971.

McCabe, G. J., M. P. Clark, and M. C. Serreze, Trends in Northern Hemisphere Surface Cyclone Frequency and Intensity, *J. Climate*, ***14***, 2763–2768, 2001.

Meier, W. N., and J. A. Maslanik, Synoptic-scale ice-motion case-studies using assimilated motion fields, *Ann. Glaciol.*, ***33***, 145–150, 2001a.

Meier, W. N., and J. A. Maslanik, Improved sea ice parcel trajectories in the Arctic via data assimilation, *Mar. Pollut. Bull.*, ***42***, 506–512, 2001b.

Meier, W. N., and J. A. Maslanik, Effect of environmental conditions on observed, modeled, and assimilated sea ice motion errors, *J. Geophys. Res.*, ***108***(C5), doi: 10.1029/2002JC001333, 2003.

Meier, W. N., J. A. Maslanik, and C. W. Fowler, Error analysis and assimilation of remotely sensed ice motion within an Arctic sea ice model, *J. Geophys. Res.*, ***105***(C2), 3339–3356, doi:10.1029/1999JC900268, 2000.

Mitchell, H. L., P. L. Houtekamer, and G. Pellerin, Ensemble Size, Balance, and Model-Error Representation in an Ensemble Kalman Filter, *Mon Weather Rev*, ***130***, 2791–2808, 2002.

Murray, F. W., On the computation of saturation vapour pressure, *J. Appl. Meteorol.*, ***6***, 203–204, 1967.

National Snow and Ice Data Center, Sea Ice Decline Intensifies, http://nsidc.org/press/20050928_trendscontinue.html, 2005.

Nerger, L., W. Hiller, and J. Schröter, A Comparison of Error Subspace Kalman Filters, *Tellus series A*, ***57A***(5), 715–735, doi:10.1111/j.1600-0870.2005.00141.x, 2005a.

Nerger, L., W. Hiller, and J. Schröter, PDAF - The Parallel Data Assimilation Framework: Experiences with Kalman filtering, in *Use of High Performance computing in Meteorology - Prooceedings of the 11. ECMWF Workshop*, edited by W. Zwiefelhofer and G. Mozdzynski, pp. 63–83, World Scientific, 2005b.

Nerger, L., S. Danilov, W. Hiller, and J. Schröter, Using sea-level data to constrain a finite-element primitive-equation ocean model with a local seik filter, *Ocean Dynamics*, ***56***(5/6), 634–649, doi:10.1007/s10236-006-0083-0, 2006.

Nerger, L., S. Danilov, G. Kivman, W. Hiller, and J. Schröter, Data assimilation with the Ensemble Kalman Filter and the SEIK filter applied to a finite element model of the North Atlantic, *J. Marine Science*, ***67***(1-4), 288–298, doi: 10.1016/j.jmarsys.2005.06.009, 2007.

NOAA Satellite and Information Service, Digital relief of the surface of the earth, *Data Announcment 88-MGG-02*, National Geophysical Data Center, Boulder, Colorado, 1988.

NSIDC, *Submarine upward looking sonar ice draft profile data and statistics*, Boulder, CO: National Snow and Ice Data Center/World Data Center for Glaciology. Digital media, 1998, updated 2006.

Ortmeyer, M., and I. Rigor, International Arctic Buoy Programme Data Report 1 January 2003 - 31 December 2003, *Technical Memorandum APL - UW TM 2-04*, Applied Physics Laboratory, University of Washington, http://iabp.apl.washington.edu, 2004.

Owens, W., and P. Lemke, Sensitivity studies with a sea ice-mixed layer pycnoline model in the weddel sea, *J. Geophys. Res.*, ***95***(C6), 9527–9538, 1990.

Parkinson, C. L., and W. M. Washington, A large-scale numerical model of sea ice, *J. Geophys. Res.*, ***84***(C1), 311–337, 1979.

Parkinson, C. L., J. Comiso, H. J. Zwally, D. J. Cavalieri, P. Gloersen, and W. J. Cambell, Arctic sea ice, 197-1976: Satellite passive microwave observations, *NASA Spec. Publ.*, ***SP-489***, 295 pp., 1987.

Pham, D. T., Stochastic Methods for Sequential Data Assimilation in Strongly Nonlinear Systems, *Mon Weather Rev*, ***129***, 1194–1207, 2001.

Pham, D. T., J. Verron, and L. Gourdeau, Singular evolutive Kalman filters for data assimilation in oceanography, *C. R. Acad. Sci. Ser. II*, ***326***(4), 255–260, 1998a.

Pham, D. T., J. Verron, and M. C. Roubaud, A singular evolutive Kalman filter for data assimilation in oceanography, *J. of Mar. Syst.*, ***16***, 323–340, 1998b.

Polyakov, I. V., A. Beszczynska, E. C. Carmack, I. A. Dmitrenko, E. Fahrbach, I. E. Frolov, R. Gerdes, E. Hansen, J. Holfort, V. V. Ivanov, M. A. Johnson, M. Karcher, F. Kauker, J. Morison, K. A. Orvik, U. Schauer, H. L. Simmons, Ø. Skagseth, V. T. Sokolov, M. Steele, L. A. Timokhov, D. Walsh, and J. E. Walsh, One more step toward a warmer Arctic, *Geophys. Res. Lett.*, *32, L17605*, doi:10.1029/2005GL023740, 2005.

Pritchard, R. S., An elastic-plastic constitutive law for sea ice, *J. Appl. Mech.*, ***43E***, 379–384, 1975.

Proshutinsky, A., R. H. Bourke, and F. A. McLaughlin, The role of the Beaufort Gyre in Arctic climate variability: Sesonal to decadal climate scales, *Geophys. Res. Lett.*, ***29***(23), doi:10.1039/2002GL015847, 2002.

Rothrock, D. A., The energetics of the plastic deformation of pack ice by ridging, *J. Geophys. Res.*, ***80***(30), 4514–4519, 1975.

Rothrock, D. A., Y. Yu, and G. A. Maykut, Thinning of the Arctic Sea-Ice Cover, *Geophys. Res. Lett.*, *26*(23), 3469–3472, doi:10.1029/1999GL10863, 1999.

Rothrock, D. A., J. Zhang, and Y. Yu, The arctic ice thickness anomaly of the 1990s: A consistent view from observations and models, *J. Geophys. Res.*, ***108***(C3), doi: 10.1029/2001JC001208, 2003.

Semtner, A. J., A model for the thermodynamic growth of sea ice in numerical investigations of Climate, *J. Phys. Oceanogr.*, ***6***, 409–425, 1976.

Stroeve, J. C., M. C. Serreze, F. Fetterer, T. Arbetter, W. Meier, J. Maslanik, and K. Knowles, Tracking the Arctic's shrinking ice cover: Another extreme September minimum in 2004, *Geophys. Res. Lett.*, ***32***(4), doi:10.1029/2004GL021810, 2005.

Thomas, D., and D. Rothrock, Blending Sequential Scanning Multichannel Microwave Radiometer and buoy data into a sea ice model, *J. Geophys. Res.*, ***94***, 10,907–10,920, 1989.

Thomas, D., and D. Rothrock, The arctic ocean ice balance: a kalman smoother estimate, *J. Geophys. Res.*, ***98***, 10,053–10,067, 1993.

Thomas, D., S. Martin, and M. Steele, Assimilating satellite concentration data into an Arctic sea ice mass balance model, *J. Geophys. Res.*, ***101***, 20,849–20,868, 1996.

Thorndike, A. S., Kinematics of sea ice, in *The Geophysics of Sea Ice, NATO ASI Ser., Ser. B Phys.*, vol. 146, edited by N. Untersteiner, pp. 489–549, Plenum, New York, 1986.

Thorndike, A. S., A toy model linking atmospheric thermal radiation and sea ice growth, *J. Geophys. Res.*, ***97***(C6), 9401–9410, 1992.

Timmermann, R., A. Beckmann, and H. H. Helmer, Simulations of ice-ocean dynamics in the Weddell Sea 1. Model configuration and validation, *J. Geophys. Res.*, ***107***(C3), doi:10.1029/2000JC000741, 2002.

Timmermann, R., H. Goosse, G. Madec, T. Fichfet, C. Ethe, and V. Duliére, On the representation of high latitude processes in the ORCA-LIM global coupled sea ice-ocean model, *Ocean Modelling*, ***8***, 175–201, 2005.

Timmermann, R., S. Danilov, J. Schröter, C. Böning, and K. Rollenhagen, A finite-element global coupled sea ice – ocean model, *to be submitted to J. Geophys. Res.*, in preparation.

Untersteiner, N., On the mass and heat budget of Arctic sea ice, *Arch. Meteorol. Geophys. Bioklimatol.*, ***A***(12), 151–182, 1961.

Vowinckel, E., and S. Orvig, The Climate of the North Polar Basin, in *Climates of the polar regions*, World Survey of Climatology, vol. 14, Hrsg. S. Orvig, 1970.

Walsh, J. E., and W. L. Chapman, 20th century sea-ice variations from observation data, *Ann. Glaciol.*, ***33***, 444–448, 2001.

Weeks, W. F., Groth Conditions and the Structure and Properties of Sea Ice, in *Physics of Ice-Covered Seas, Vol. 1*, edited by M. Leppärante, pp. 25–104, Helsinki University Printing House, Helsinki Finland, 1998.

Wensnahan, M., *Submarine upward looking sonar ice draft profile data and statistics: Documentation for G01360 Analog Subset*, National Snow and Ice Data Center, http://nsidc.org/data/docs/noaa/g01360_upward_looking_sonar/index.html, 2006.

Wensnahan, M., and D. Rothrock, Sea-ice draft from submarine-based sonar: Establashing a consistent record from analog and digitally recorded data, *Geophys. Res. Lett.*, ***32***, doi:10.1029/2005GL022507, 2005.

Yen, Y. C., Review of the thermal properties of snow, ice and sea ice, *Tech. Rep. 81-10, 27pp*, U.S. Army Corps of Eng., Cold Reg. Res. Eng. Lab., 1961.

Zhang, J., and W. D. Hibler, On an efficient numerical method for modeling sea-ice dynamics, *J. Geophys. Res.*, ***102***(C4), 8691–8702, 1997.

Zhang, J., D. R. Thomas, D. A. Rothrock, R. W. Lindsay, Y. Yu, and R. Kwok, Assimilation of ice motion observations and comparisons with submarine ice thickness data, *J. Geophys. Res.*, ***108***(C6), doi:10.1029/2001JC001041, 2003.

Zhang, X., J. E. Walsh, J. Zhang, U. Bhatt, and M. Ikeda, Climatology and Interannual Variability of Arctic Cyclone Activity: 1948-2002, *J. Climate*, ***17***, 2300–2317, 2004.

Zillman, J. W., A study of some aspects of the radiation and heat budgets of the southern hemisphere oceans., in *Meteorological study*, vol. **26**, p. 526pp., Bureau of Meteorolgy, Dept. of the Interior, Canberra, Australia, 1972.

Acknowledgments

My sincere thanks I give to Prof. Dr. Peter Lemke for the opportunity of a very interesting and exciting PhD study at the AWI and for the final comments rounding off the thesis.
I thank Prof. Dr. Rüdiger Gerdes for reviewing this thesis.
I'm very grateful to my supervisor Dr. Jens Schröter for scientific discussions and suggestions and the possibilities to present my work at international conferences and workshops.
I also want to thank Dr. Christian Haas who introduced me into the fascinating world of sea ice and his offer participating in the NABOS cruise 2005 into the Laptev Sea.
Furthermore, I want to thank Ralph and Torge for their patience for all my questions to the sea-ice physics and the surrounding processes and the modeling aspects. Thanks for all the inspiring discussions we had. Special thanks go to the other colleagues of the sea-ice group: Stephan, Thomas K., Lasse, Wolfgang and those who have left: Carola, Sybille, Thomas B. and Marcel (I apologize if I forgot someone). I have especially enjoyed their sea-ice observation point of view and the convenient meetings.
I also want to thank Lars for introducing me in the math world of data assimilation as well as Tijana for her fruitful discussions and suggestions to the assimilation procedure.
I do not want to forget to thank all the colleagues who contributed to the pleasant working atmosphere. Under such conditions it is a pleasure to do science.
Meinem Partner Marc Sgonina möchte ich für seine Geduld und Rücksicht danken, und dass er alle meine Bemühungen und Anstrengungen, die diese Arbeit begleitet haben, in jeglicher Hinsicht unterstützt und nie den Glauben an mich verloren hat.
Ganz besonderen Dank gilt meiner Mutter Brigitte Rollenhagen, die mich in allen meinen Vorhaben unterstützte und die eine oder andere Aufmunterung im rechten Moment parat hatte.
The Alfred-Wegener-Institute for Polar and Marine Research provided a very good infrastructure and organisational support for preparing this thesis.
This work was partly funded by the European Union Project SITHOS (EVK2-2002-00146).